8-2017

Design and Implementation of a Low-Power Wireless Respiration Monitoring Sensor

Ifana Mahbub
Univeristy of Tennessee, Knoxville, imahbub@vols.utk.edu

To the Graduate Council:

I am submitting herewith a dissertation written by Ifana Mahbub entitled "Design and Implementation of a Low-Power Wireless Respiration Monitoring Sensor." I have examined the final electronic copy of this dissertation for form and content and recommend that it be accepted in partial fulfillment of the requirements for the degree of Doctor of Philosophy, with a major in Electrical Engineering.

Syed K. Islam, Major Professor

We have read this dissertation and recommend its acceptance:

Nicole McFarlane, Aly Fathy, Mohamed R. Mahfouz

Accepted for the Council:
Dixie L. Thompson

Vice Provost and Dean of the Graduate School

(Original signatures are on file with official student records.)

Design and Implementation of a Low-Power Wireless Respiration Monitoring Sensor

A Dissertation Presented for the
Doctor of Philosophy
Degree
The University of Tennessee, Knoxville

Ifana Mahbub

August 2017

This dissertation is dedicated to my parents and my husband, who have tremendously supported me throughout the journey.

Acknowledgement

I am extremely thankful to my advisor Dr. Syed K. Islam for all his valuable suggestions, constant guidance and support throughout my graduate student life which not only helped me in my research projects but also helped me to prepare myself for my future career. I could not have achieved what I have accomplished during my graduate school without his directions and encouragements. His pieces of advice have been really useful for every aspect of my life and I could never ask for a better advisor than Dr. Islam.

I am also grateful to Dr. Nicole McFarlane for being such a supportive mentor. Our conversations during the mentor-mentee lunch sponsored by *Systers* have been tremendously helpful for me. It always amazes me how much caring she is towards all her students. I am truly thankful for her constant guidance and support during my search for full-time job positions.

I cannot thank Dr. Aly Fathy enough for all his supports throughout my graduate school. With his referral, I could not have had the opportunities of getting summer internships at Qorvo, Inc., which had been a wonderful experience for me. I have had the opportunity to take many of Dr. Fathy's courses on microwave circuit and antenna design, which intrigued my interests in RF integrated circuit design. I am really grateful for his suggestions and directions and for allowing me to do experiments in his research laboratory.

I am also thankful to Dr. Mohamed Mahfouz for his time and insightful suggestions on improving this work. I would like to extend my gratitude to him for allowing me to work in his laboratory at TechMah where Michael Kuhn and Gary To mentored me to develop the proof-of-the-concept UWB wireless communication system using the DecaWave module. Without their help, I could never finish this project.

I would like to thank my colleagues Ginny Lacquio, Nick Marcoux and my manager Doug Teeter at Qorvo, Inc. who have helped me in assembling my CMOS dies on the test PCB board. I would also like to thank Dr. Jain at the University of Connecticut for helping in packaging my chips.

I would also like to sincerely thank all my colleagues and friends in the EECS department who have helped and supported me during the last four and half years. I would like to acknowledge Samira Shamsir for helping me in testing the charge amplifier ICs, Shahriar Jahan for helping me in figuring out the Cadence troubleshoots and bare-die bonding, Terence Randall for helping me during tape-outs, Hanfeng Wang, Habib Ullah Habib, Shamim Ara Shawkat for all the technical discussions and Saeed Anwar and Peixing Liu for helping me in learning PCB designs in Altium. I am also thankful to all the members of the Bangladesh Student Association and Systers, two of the organizations that I loved being a part of. I am thankful to them for making my graduate student life a memorable one.

I would like to acknowledge the financial support from the University of Tennessee Graduate School of Medicine for the development of the wireless apnea monitoring sensor, the Chancellor for supporting my graduate school through fellowship, the department of Electrical Engineering and Computer Science (EECS) at the University of Tennessee for supporting my graduate school through Teaching Assistantships and the graduate school for funding my research proposal through 'Student/faculty research award'. I am grateful to the head of the EECS department Dr. Leone Tolbert and the Graduate Student Senate for supporting me by providing financial support for conference travels. I am grateful to all the EECS office staff members especially Dana Bryson, Kimberly Cox, Tracy Smith. Linda Robinson, Kelley Melanie, Alaa

Alharzi, Markus Iturriaga and his IT support team. I am really fortunate to have so many helpful people around me during my graduate school.

Last but not the least my special thanks go to my parents who have always provided me the moral support and encouragements when I needed them the most and my loving husband who have always supported me and drove many times back-and-forth from VA for the last three and a half years. I am truly blessed to have their unconditional love and support.

Abstract

Wireless devices for monitoring of respiration activities can play a major role in advancing modern home-based health care applications. Existing methods for respiration monitoring require special algorithms and high precision filters to eliminate noise and other motion artifacts. These necessitate additional power consuming circuitry for further signal conditioning. This dissertation is particularly focused on a novel approach of respiration monitoring based on a PVDF-based pyroelectric transducer. Low-power, low-noise, and fully integrated charge amplifiers are designed to serve as the front-end amplifier of the sensor to efficiently convert the charge generated by the transducer into a proportional voltage signal. To transmit the respiration data wirelessly, a low-power transmitter design is crucial. This energy constraint motivates the exploration of the design of a duty-cycled transmitter, where the radio is designed to be turned off most of the time and turned on only for a short duration of time. Due to its inherent duty-cycled nature, impulse radio ultra-wideband (IR-UWB) transmitter is an ideal candidate for the implementation of a duty-cycled radio. To achieve better energy efficiency and longer battery lifetime a low-power low-complexity OOK (on-off keying) based impulse radio ultra-wideband (IR-UWB) transmitter is designed and implemented using standard CMOS process. Initial simulation and test results exhibit a promising advancement towards the development of an energy-efficient wireless sensor for monitoring of respiration activities.

Table of Contents

List of Tables

List of Figures

Chapter 1 Introduction

1.1 Motivation

Wireless devices for monitoring of respiration activities can play a great role in advancing the modern home-based healthcare applications. Non-invasive respiration monitoring has become very prominent recently as it can detect various diseases such as tachypnea (high respiration rate), bradypnea (low respiration rate) and apnea (absence of breathing). Many chronic respiratory diseases such as asthma and apnea are leading causes of death worldwide which are even more critical for premature neonatal infants. Continuous respiration monitoring without placing adhesive electrodes on the skin of the newborn infants with the sleep disorder is very crucial as the adhesive electrodes could be harmful to their sensitive skin. Currently the patients require to participate in an overnight clinical sleep analysis of 12 to 24-hour duration, which is also known as polysomnography, to diagnose the symptoms of apnea. During this process, many sensors are attached to the sensitive skin of the infants resulting in irritation and inconvenience. It also requires a specially trained sleep experts to monitor the breathing pattern from the raw data, which is also very time-consuming. Other methods of respiration monitoring such as electrocardiogram (ECG), ballistocardiogram (BCG), pulse oximetry, piezoelectric MEMS-based chest belt to monitor chest dilation, strain gauge, and microphone for tracheal sound monitoring require special algorithm and high precision filter to eliminate noise and artifacts due to body movements that are not associated with respiration. These result in additional power-consuming blocks for the front-end circuitry. The aforementioned problems intrigue the motivation to look for an alternate approach to respiration monitoring which does not require any additional circuitry for filtering, is light-weight

and flexible so that it can be incorporated in a wearable sensor and is biocompatible and can be incorporated into silicon integrated circuits (IC).

Almost all of the biomedical sensing systems require a front-end amplifier to amplify the acquired data. Depending on the application, some amplifiers might require very high gain, and low input-referred noise, high bandwidth, and high output voltage swing etc. Breathing signal usually ranges from 1 mHz to 1 Hz range, therefore the amplifier designed for this particular application has to be optimized to detect such a low-frequency signal. It also needs to achieve a low input-referred noise to be able to detect an even smaller amplitude of breathing signal. Unfortunately, not many front-end amplifiers particularly suitable for the respiration monitoring application have been published in the literature. Therefore the primary motivation of this work is to further investigate the front-end amplifier circuit optimizing it specifically for ultra-low frequency respiration monitoring application.

Following acquisition and subsequent amplification the data needs to be transmitted for further signal processing. The data communication needs to be wireless to make the sensor portable and user-friendly. To transmit the data wirelessly, a low-power transmitter design is crucial. Communication standards such as MICS (Medical Implant Communications Service), WMTS (Wireless Medical Telemetry Service), Bluetooth (IEEE 802.15.1), and Zigbee (IEEE 802.15.4) are some of the most popular choices for implantable and wearable sensors. Most of the radios in these communication standards are power-hungry requiring frequent replacement of the battery which is not desirable for a wearable or implantable biomedical sensor applications. In addition, most of the biomedical sensors harvest energy from ambient sources to power up the processing circuitry. Typically the harvested energy from various ambient sources such as heat, vibration, electromaganetic radiation etc. is in the range of few nWs to few µWs and therefore the signal

processing circuitry along with the transmitter has to be designed to accommodate the energy constrained environment. Energy efficiency is defined by the term called "energy per bit", E_b, which determines the energy that is required to transmit a digital bit by the transmitter. E_b increases as the data rate decrease ($E_b = \frac{Power}{Data\ rate}$). Thus it is even harder to design an energy efficient radio for low-data rate application. This energy constraint provides motivation to look into the design of a duty-cycled transmitter, where the radio would be shut down most of the time and active for only a short period so that the average power consumption is even lower to increase the energy efficiency. The total power consumed by a duty-cycled transmitter is a combination of the active power (*on* state) and the leakage power (*off* state). The design challenge lies not only in reducing the active power but also the leakage power since the majority of the time the transmitter dissipates leakage power.

1.2 Prior Work

Apnea is defined as the partial or complete cessation of breathing and is one of the leading respiratory disorders for premature infants. Continuous monitoring of respiration and early detection of apnea is critically important to prevent neonatal mortality. The current gold standard for apnea diagnosis namely polysomnography (PSG) is used to diagnose pediatric sleep apnea involving various wires and electrodes to be placed on delicate bodies of the infants and is both expensive and inconvenient to the patients. In addition, this complex study includes multiple physiological parameters such as heart rate, blood pressure, and blood oxygen saturation level (SpO_2) [1]. Although these parameters exhibit a well-defined behavior during apnea, they can be affected by other cardiovascular phenomena and are also characterized by the secondary evidence of apnea as they are delayed by many seconds of breathing cessation. Therefore, several research efforts have been attempted to develop a suitable apnea detection system by monitoring the

respiratory signal which includes acoustic or optical based methods [2], [3], [4] or some advanced techniques by using piezoelectric, infrared or ultrasound sensors [5]. [6] [7]. Most of the acoustic based methods are based on tracking of the sound of the nasal airflow and are susceptible to the environmental and the internal body noise and thus need to incorporate sophisticated frequency analysis to extract breathing from different interfering signals which increases the system cost and degrades device reliability in the present systems. The technique of measurement of the breathing rate via thoracic or abdominal movement also requires complex algorithms for signal processing and are also not suitable for neonatal infants having very delicate and sensitive skins. For this particular patient category, non-contact sensor based respiratory evaluation is more convenient, which is yet to be developed.

In general, various approaches to respiration monitoring can be broadly categorized as noncontact and contact-based methods. For the methods which are contact-based, the sensing device or element has a direct contact with the patient's body. On the other hand, for noncontact-based approaches, the instrument is not directly connected with the patient's body. Most of the noncontact-based approaches found in the literature are based on the ultra-wide band (UWB) radar signal or infrared image processing. One such noncontact-based respiration monitoring approach is proposed by Chekmenev *et al.*, which uses wavelet-based measurement using thermal imaging [8]. In this approach, the temperature changes around the nasal area, neck region and the carotid vessel complex are monitored using a special thermal camera. The camera has a focal plane array for a long-wave infrared (IR) (6–15 μm) sensor. These regions of interests are manually selected on which a continuous wavelet analysis technique is applied to extract the respiration rate and the ECG signal. Although this type of face thermography for vital sign detection has potential application for noncontact health monitoring, the use of multi-scale image decomposition

technique is very complex. In addition, the manual selection of the region of interests increases this complexity for continuous tracking of features and the noise from motion artifacts also hinders the overall performance of the system. Another contactless respiratory rate monitoring method is proposed by Zito *et al.* that uses UWB pulse radar sensor [9]. This approach uses a pulse generator that transmits short pulses at a certain repetition frequency and an antenna that captures the signal bounced back by the target. The delay and the phase correlations between the transmitted pulse and the received echo are further analyzed to detect the respiratory rate. The primary benefit associated with this approach is that it provides the implementation of a non-intrusive vital sign detection as well as a low power wireless data communication. However, this type of UWB based radar approach can only provide phase information and lacks the ability to differentiate between normal and shallow breathing. In addition, most noncontact approaches depend significantly on the distance and the position of the sensors and the motion artifacts that corrupt the resolution of the breathing signal. In order to achieve a better signal-to-noise ratio (SNR), often there is a tradeoff between the power level and the signal resolution. Moreover, these types of pulse sources or impulse signal generators can most likely be a concern for many potential users, especially for neonatal infants.

Contact-based but noninvasive and wearable continuous respiration monitoring can also be achieved by using different forms of miniature sensors. Rodriguez-Villegas *et al.*[3] proposed such a type of a miniaturized and wearable respiration monitoring respiration system based on acoustic sensors. This system consists of a microphone attached to the neck of the patient to detect the largest acoustic signal due to the turbulence of the airflow during respiration. The acoustic signal is acquired using a sensor connected to a soundcard and the signal processing is performed to extract the respiratory information. The algorithm used for the modulation and filtering of the

signal is very complex and the complexity affects the design of electronic circuits and power consumption. Moreover, the extraction of the breathing sound from other wideband noise sound depends on the surrounding environment of the patient, which hinders automatic, and the versatile application of this system. Another type of sensor based respiratory monitoring system can be found in literature where different types of microelectromechanical systems (MEMs) based sensors are employed. Liao *et al.*[10] present a CMOS-MEMS capacitive flow sensor that translates the change in pressure of respiratory airflow to a corresponding change in capacitance of a sensing electrode. A similar type of concept is also used by Liu *et al.* who proposed a nano-electromechanical system (NEMS) based on carbon nanotube sensors to detect apnea [11]. Although MEMS or NEMS-based sensors are very promising as miniaturized health care devices, fabrication and processing costs of this type of sensors make it commercially challenging. Capnometry is another approach for respiratory monitoring that uses a capnometer and optional graphing capability (capnograph) to measure carbon dioxide concentration in expired gasses. A prototype device has been reported by Folke *et al.* [12] that uses such type of a CO_2 sensor to detect the variable CO_2 concentration between expired air and normal indoor air. In this system, a receptor is placed to collect nasal and oral expired air in front of the nose and the mouth. The capnometry sensor can detect variation of CO_2 concentration by sensing the change of mean molecular weight within the small air cell. The breathing signal is represented as pulse processed by electronic circuitry. In this approach, a slight design change in the sensing device results in a large discrepancy in the performance of the sensor. For this reason, the receptor needs to be mounted reliably while avoiding any invasive contact with the sensitive skin of the patient which, however, may conflict with the comfort of the patients. In addition, the proposed system does not

include any wireless data transmitting system and automated detection of an apneic event, which makes this system inconvenient for continuous respiration monitoring.

A different version of the low-power respiration monitoring system has been proposed using the piezoelectric property of the PVDF sensor instead of the pyroelectricity in [13], [14]. In this method, the pressure induced by the chest dilation during respiration has been utilized. The piezoelectric property of the PVDF sensor can produce charge corresponding to the change in pressure. The sensor along with the complete integrated circuit is attached inside a jacket or vest in particular places that would be worn by the patients with respiratory distress. A similar type of respiration monitoring system based on piezoelectric PVDF sensor has been proposed by Hwang *et al.* [15]. However, in this system, the sensors are embedded in the mattress, which makes the process more susceptible to motion artifacts

Low-power, low-noise, and fully integrated CMOS front-end amplifier design has spurred considerable interest for potential applications in biomedical sensors. In particular, because of the low signal amplitude, the biomedical signals have to be amplified before performing any signal conditioning. The design of such front-end amplifier particularly focuses on noise limitation, power consumption, gain and bandwidth for a particular application. Various topologies have been explored to design low-power, low-noise front-end amplifiers for biomedical sensors. A chopper-stabilized low-noise amplifier has been reported by Denison *et al.* for neural field potential application [16]. However, this type of amplifier consumes more area and adds complexity to the design to minimize the input-referred noise. Harrison *et al.* incorporated such a single-ended topology to design a low-power low-noise amplifier [17]. Kmon *et al.* have presented the techniques to minimize the input-referred noise of the amplifier along with the offset voltage correction [18]. The lack of literature in this area of research leads to the need for the design of a

low-power, low noise front-end amplifier capable of amplifying respiration signal of frequency as low as 1 mHz.

As mentioned earlier, biomedical signals, in general, have low frequency and thus require a low-data rate transmitter for transmitting the data wirelessly. Unlike the traditional radios for cellular application, these radios can transmit low energy for short-range communication. For an energy harvested sensor application, the available energy is often less than 100µW. Assuming the power budget for the front-end readout circuitry, the ADC and the voltage regulator is ~50µW, the transmitter needs to be dissipating less than 50µW of power. Even though there are many published works regarding the design of traditional narrowband transmitters for low-data rate applications, the lowest power consuming transmitter in that design space still consumes ~900µW of power [19]. For that reason, a duty-cycled radio seems to be appropriate for such an energy-constrained application. Due to its inherent duty-cycled nature, this work looks into the impulse radio ultra-wideband (IR-UWB) architectures for the implementation of a duty-cycled radio. Much of the work involving IR-UWB transmitter demonstrate excellent energy efficiency for high-data rate applications. However, the energy efficiency is not equally perfect for low-data rate applications [20], [21]. Moreover, the leakage power in these works is much higher, which even degrades the energy efficiency at 100 kbps data rate. The aforementioned challenges have inspired the need for the development of a low-power, low-data rate IR-UWB transmitter with low leakage power dissipation to achieve longer battery lifetime.

1.3 Research Objectives

The goal of this research is to study the challenges that are mentioned in the previous section into more details and identify the prospective solutions. One of the objectives is to study the front-end transducer for the point-of-care respiration monitoring system. It is also important to

characterize the proposed *polyvinylidene fluoride* (PVDF) based pyroelectric transducer so that it can be placed inside the nasal cavity or inside a cannula of the patient. The next objective is to design a low-power, low-noise operational transconductance amplifier (OTA) based charge amplifier to convert the charge generated by the transducer due to the change in the temperature caused by the nasal air flow into a proportional voltage signal. For an energy constrained system such as the wearable respiration monitoring sensor, the power consumption can be significantly reduced by duty-cycling the radio communication. The next objective is to study a low-power impulse radio ultra-wideband (IR-UWB) transmitter to implement aggressive duty-cycling to reduce average power consumption. Unlike the traditional continuous wave (CW) transmitters, the IR-UWB transmitter does not require any mixer or PLL (phase locked loop), which minimizes the power consumption of the system. For the wireless transmission of the data, on-off keying based transmitter scheme needs to be analyzed to reduce the complexity of the transmitter architecture.

1.4 Overview of the Dissertation

The remaining chapters of this dissertation will cover the design of the different blocks of the proposed respiration monitoring sensor. Chapter 2 presents an overview of the proposed system. Chapter 3 describes the detailed design and analysis of the proposed charge amplifier along with the simulation and measurement results. Chapter 4 presents an overview of the UWB transmitter along with a proof-of-the-concept system development using commercially available UWB transceiver module. Chapter 5 presents the detailed design analysis, simulation and measurement results of the proposed voltage-controlled oscillator and driver/power amplifier in the proposed IR-UWB transmitter system. Chapter 6 presents three low-power IR-UWB transmitter designs which have been able to achieve a competitive energy efficiency by

aggressively duty-cycling the transmitter as well reducing the supply voltage. Chapter 7 concludes this dissertation and presents some future work directions.

Chapter 2 Pyroelectric Transducer

This chapter presents a system level overview of the pyroelectric transducer based respiration monitoring system. A PVDF-based pyroelectric transducer is proposed for the system and the characterization, as well as the feasibility of the transducer for this particular application, are also presented.

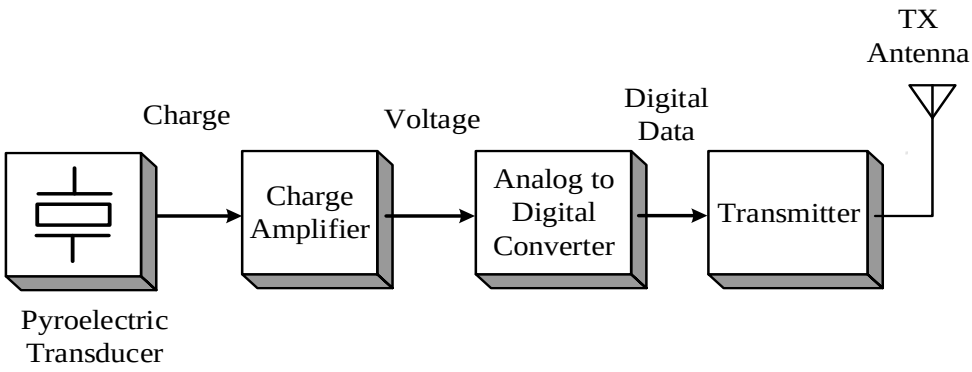

Figure 2.1: Block diagram of the proposed respiration monitoring sensor.

2.1 Proposed System Overview

Fig. 2.1 shows the block diagram of the proposed respiration monitoring system. The proposed PVDF-based pyroelectric polymer transducer is placed underneath the nostril of the patient or inside a mask or cannula to detect the temperature change during breathing. As the nasal air flow increases the temperature of the transducer, the dipoles inside the PVDF material gain kinetic energy from thermal energy and as a result the net number of non-neutralized dipoles on the surface increases. These charges that are generated at the surface of the transducer are then converted to a proportional voltage signal by a charge amplifier. The analog-to-digital converter (ADC) has not been designed as a part of this work. A low-power successive approximation register (SAR) ADC with 10 ksample/s and 10 bit resolution works efficiently for this application

and results in 100 kbps data rate which is then transmitted by a low-power transmitter. The pyroelectric polymer transducer is placed at the front-end of the device and generates a charge signal when the temperature changes due to breathing. The transducer is composed of a metalized thin layer of *polyvinylidene fluoride* (PVDF) which is attached to the inside wall of the nasal cannula placed in the nostrils of the patient. A charge amplifier converts the charge generated due to the temperature change into a voltage signal and subsequently the necessary processing is performed to determine the presence or absence of the breathing. The amplitude of the breathing signal being constantly below a certain threshold for a period of 20 seconds denotes the occurrence of apnea and an alarm signal is generated by the processing circuitry. The alarm signal is transmitted wirelessly to a receiver node attached to the bed of the patient. As soon as the node receives the alarm signal, it activates a vibrating device attached to the bed which wakes the patient up causing apnea to cease. The breathing signal is also continuously transmitted to a remote central location using a low-power ultra-wideband (UWB) transmitter. The signals coming in from different beds in an incubator are stored in the central system and a nurse or a caregiver can monitor the respiratory pattern of each patient from the remote location.

2.2 Integration of the PVDF Transducer

The proposed breathing monitoring sensor is designed to be placed inside a cannula which is configured to be placed underneath the nostrils of the patient. This specially fabricated cannula is made of polydimethylsiloxane (PDMS) and the molds that shape the liquid PDMS are made of acrylonitrile butadiene styrene (ABS) [22]. PDMS is one of the most attractive choices for biomedical sensing application due to its biocompatibility property. This material helps absorb additional humidity produced by respiration thus ensuring the longevity of the electronic components. The molds are fabricated using a 3D printer (Stratasys Uprint SE) for upholding the

shape of the cannula. The fabrication process uses two molds made of ABS in which the PDMS mixture is cast. The upper part of the cannula has two prongs and the lower part has the integrated PVDF transducer. A thin layer of silver is deposited on the surface of the PVDF material using a sputtering technique to provide the electrical contact for the subsequent electronic circuitry. Metallization is also required to collect the charge generated from the polymer. A graphite layer is also used along with the PVDF sensor which acts as an absorbing layer (Fig. 2.2). The graphite layer provides an electrical contact for the front-end circuitry. Following the preliminary de-scum process, the PVDF liquid is injected into the ABS mold and is then placed inside a temperature chamber for polymerization to occur at a temperature of 60^0 C. The fabricated cannula and its dimensions are shown in Fig. 2.3. The fabricated cannula which has a dimension of 20 mm by 10 mm, is very light in weight (only 2 gram) and is suitable to be connected to the front-end electronics.

The charge generated at the surface of the PVDF transducer can be quantified as;

$$Q_p(t) = p_Q S\, T_p(t) \tag{2.1}$$

where $Q_p(t)$ is the charge generated from the polymer, p_Q is the pyroelectric charge coefficient, S is the surface of the transducer and $T_p(t)$ is the difference between the upper and the lower surface temperatures of the film. The equivalent thermal model of the pyroelectric transducer is shown is Fig. 2.4. The charge generated by the transducer can be electrically modeled by a pulsed current source across a capacitor and a resistor. The values of the resistor and the capacitor depending on the dimensions of the transducer. For a 2mm x 20 mm x 20μm transducer, the resistance and capacitance values are few GΩs and few pFs, respectively.

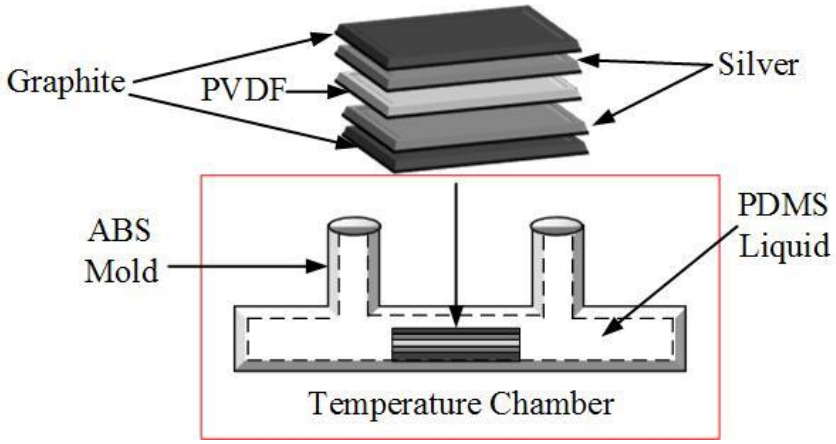

Figure 2.2. The polymerization process of the proposed respiration sensor.

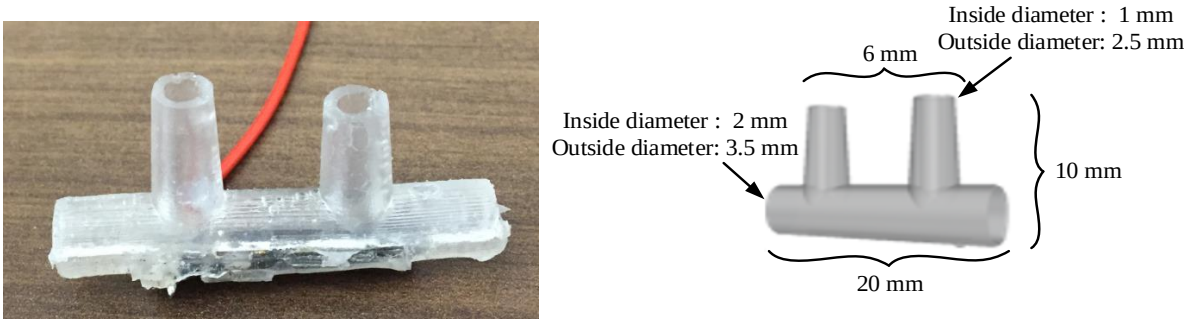

(a) (b)

Figure 2.3: (a) 3-D printed cannula with integrated PVDF sensor and (b) outer and inner dimension of the fabricated cannula.

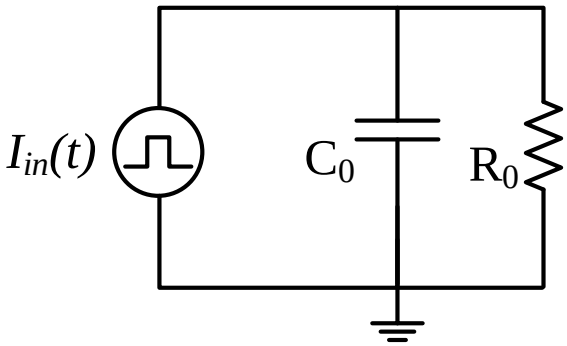

Figure 2.4: Thermal equivalent model of a pyroelectric transducer.

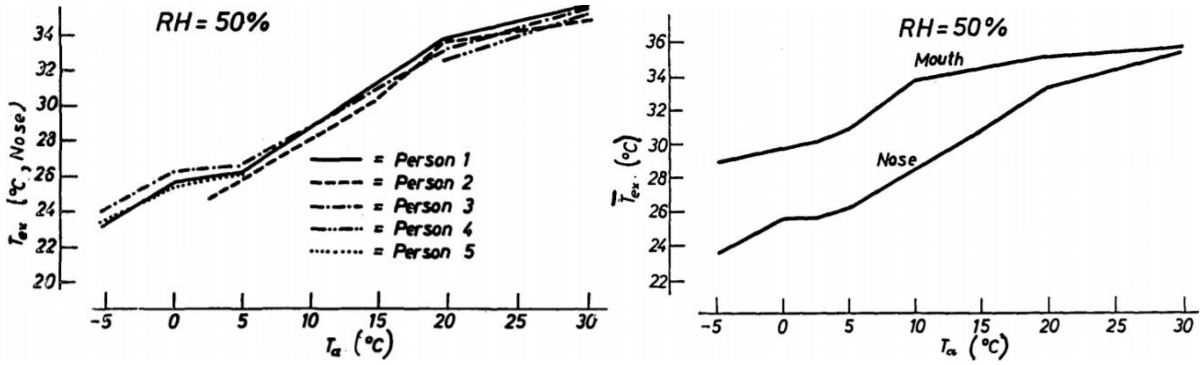

(a) (b)

Figure 2.5: (a) Plot of the measured nasal air temperature versus surrounding air temperatures and (b) mouth and nasal air temperature relative to the room temperature [23].

2.3 Characterization of the PVDF Transducer

The total amount of charge at the surface of the PVDF transducer, placed inside the nasal cannula or right under the nostrils with a patch, primarily depends on the external room temperature, the skin temperature of the patient and the temperature of the exhaled air. If the breathing stops for a long period of time the transducer approaches the thermal equilibrium depending on the external room temperature and the skin temperature. It is possible to obtain an analytical estimation of this temperature values by the use of the heat equation which takes into account the thermal properties of the two mediums in contact.

During breathing the temperature of the sensor cyclically vary between a minimum and a maximum which mainly depends on the environmental (room temperature) and the exhaled air temperatures. The relationship of breathing temperature with the environmental/room temperature has been investigated and reported in the literature [23]. Fig. 2.5(a) shows the temperature of the nasal air (T_{ex}) versus the environmental temperature (T_a) for five different subjects. With a relative humidity of 50%, T_{ex} reaches 32^0C with a variation of 5^0C or more as T_a varies between 20 - 25^0 C. Fig. 2.5(b) shows the average temperature of the expired nasal air ($\overline{T_{ex}}$) and the air coming from

the mouth as the external temperature changes. As expected, the mouth temperature is about 2 – 3 ^{0}C higher than that of the nasal air.

Fig. 2.6 shows the variation of nasal air temperature during breathing cycles when the room temperature is about 21°C [23]. The temperature of the air coming out of nostrils varies from 22°C to 32°C. The temperature variation is ±5°C from the mid-temperature which is about 25°C. The corresponding charge generated on the surface of the PVDF transducer due to this temperature variation can be calculated from equation 2.1

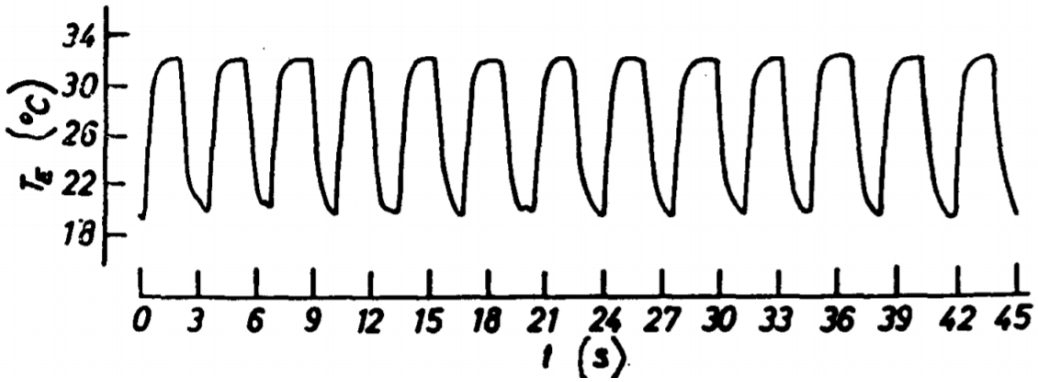

Figure 2.6: Temperature variations of nasal air throughout the breathing cycles [23].

2.4 Temperature Resolution and Sensitivity

From equation 2.1, it is clear that the electrical charge is generated by the PVDF transducer due to the temperature change as long as the pyroelectric coefficient is not zero. Newsome *et al.* [24] measured the pyroelectric coefficients of the PVDF transducer for a temperature as low as 3° K. The other parameters for quantifying the total amount of charge generated are the surface area of the transducer and the rate of change of temperature, dT/dt. The minimum detectable temperature change or the resolution or the sensitivity of the sensor depends on the front-end amplifier. The lower the input-referred noise of the charge amplifier the higher is the resolution of

the sensor. It is the goal at the circuit designer's end to minimize the input-referred noise so that the minimum amount of charge generated by the transducer could be amplified by the amplifier. In the PVDF-based temperature sensor proposed by Pullano *et al.* [25] the transducer (2 by 0.5 mm dimension) is illuminated with a LED light of 50 mW thus creating an absolute maximum temperature difference of 350 m°K. Fig. 2.7 shows the temperature detected by the sensor as the impulse of infrared light (0.3 ms of duration) is radiated on the transducer. From the figure, it can be concluded that a charge amplifier realized with commercially available off-the-shelf components can detect temperature as low as 0.3 °C. The temperature decreases exponentially as the PVDF reaches thermal equilibrium.

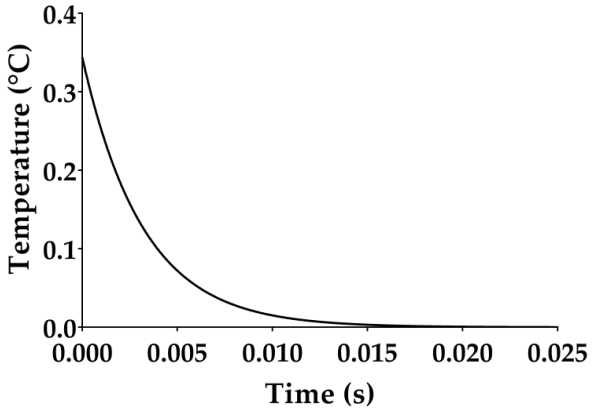

Figure 2.7: Temperature difference measured by the PVDF transducer for the infrared light (50mW) radiated for 3 ms duration [25].

Thus, it is possible to develop a temperature model for the estimation of the maximum temperature difference between the upper and the lower plates of the transducer by illuminating an infrared light at a given radiance power and measuring the experimental voltage at the charge amplifier output. This experiment also allows one to determine the temperature resolution of the sensor. From the experimental results published in [25], it can be concluded that a resolution in the m°C range can be obtained using the PVDF transducer and a low-noise charge amplifier.

2.5 Proposed System Overview

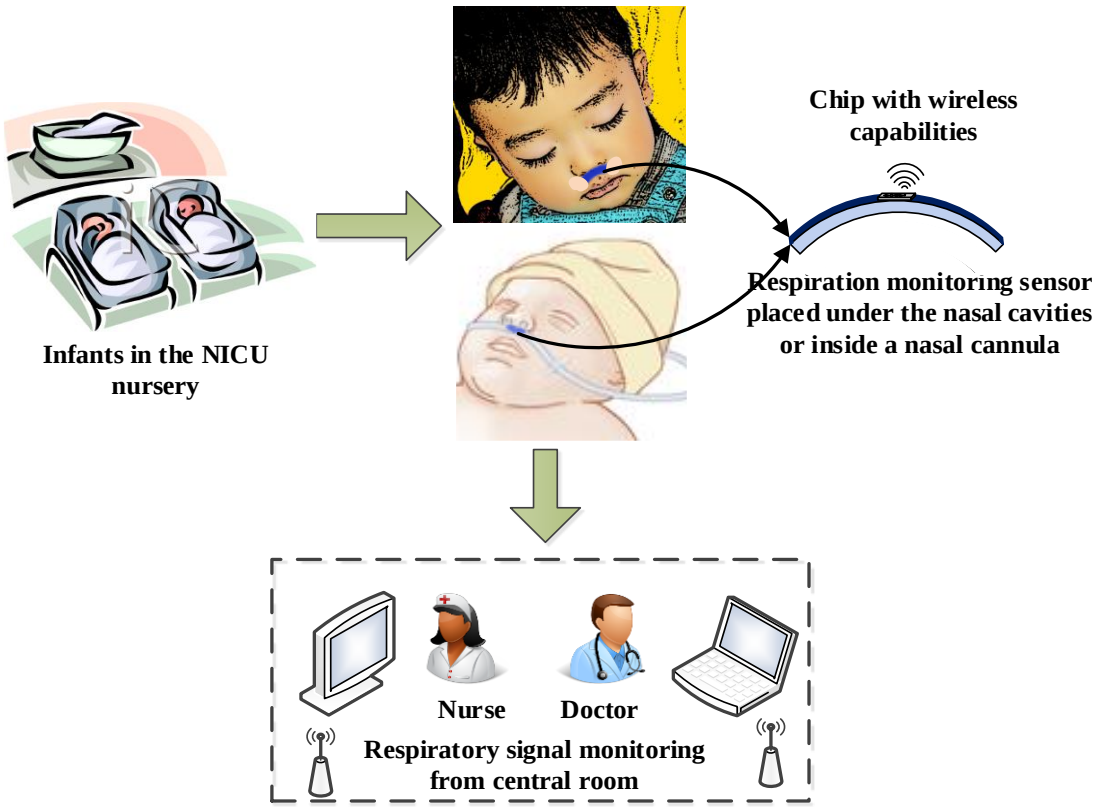

Figure 2.8: Overview of the proposed system.

The overview of the proposed system is shown in Fig. 2.8. At the front-end of the device, a pyroelectric polymer transducer is used that generates a proportional charge as the temperature changes due to respiration. The transducer is composed of a metalized thin layer of *polyvinylidene fluoride* (PVDF). The transducer can either be lying on a patient-compatible soft bandage (20 μm in thickness) placed under the nasal cavities or can be attached to a nasal cannula placed in the nostrils of the patient. A front-end charge amplifier is designed to convert the charge generated due to the temperature change into a proportional voltage signal. The analog voltage signal is then digitized and transmitted wirelessly using a low-power ultra-wideband (UWB) transmitter. In the receiving end, the signal will again be converted back to the analog domain followed by subsequent

processing for eventual detection of various respiratory disorders such as apnea. The breathing signals from different patients are wirelessly transmitted to a central system so that a nurse or a care giver can monitor the respiratory pattern from a remote location. If apnea or any other respiratory disorder is detected, the system will send an alarm signal to the central system so that necessary actions can be taken immediately. A motor can also be mounted under the hospital bed so that it vibrates when sleep apnea occurs to wake the patient up immediately.

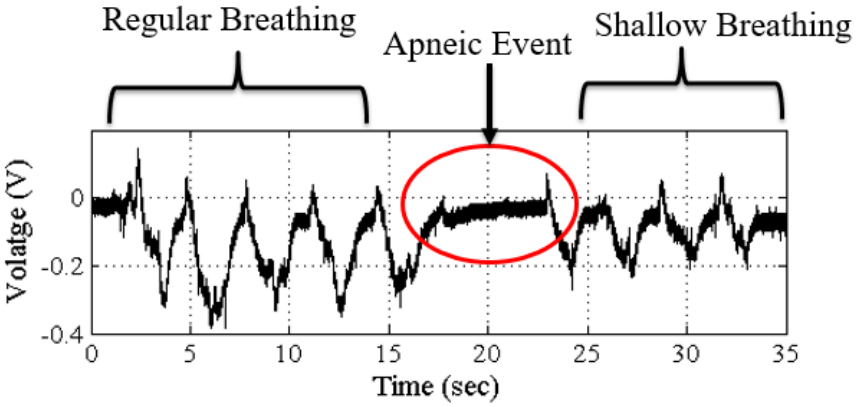

Figure 2.9: Respiratory signal acquired by the fabricated cannula sensor and charge amplifier.

To demonstrate the proof of concept, initial testing was performed by breathing through the nasal cannula with a PVDF film sensor attached inside the wall of the cannula. Apnea condition is emulated by holding breath for a certain period of time. The charge generated by the PVDF sensor is converted to amplified voltage signal using OPA 127 off-the-shelf amplifier and other components. The acquired breathing signal is shown in Fig. 2.9. The signal amplitude varied when normal breathing is maintained, but it remained almost constant when there was no valid breathing signal. From Fig. 2.9 it can be seen that the voltage signal acquired by the transducer ranges from 400 - 500 mV_{pp} for regular breathing condition. When there is a cessation of breathing, which is shown in Figure 2.9 (from 16 - 24 second), the amplitude of the signal is lower than 20 mV_{pp}. The objective of the front-end signal processing circuitry is to identify the apneic event by monitoring

this signal. Apneic event is identified if the amplitude of the voltage signal at the amplifier output is lower than a certain threshold amplitude for consecutive 20 seconds.

2.6 Summary

In this chapter, the characterization and an analysis of the sensitivity of the PVDF-based pyroelectric transducer for respiration monitoring application are presented. An overview of the proposed system along with the preliminary respiration signal acquired from the PVDF transducer and charge amplifier is also discussed.

Chapter 3 Front-End Readout Circuitry

In this chapter, a folded-cascode topology is utilized for the design of a front-end charge amplifier while achieving the design challenges of low-power consumption and low-noise contribution to the system. Since the lower cut-off frequency of the amplifier is in the sub-Hz range, it is highly suitable for the respiration monitoring application. The charge amplifier presented in this chapter converts the charge signal into a proportional voltage signal without the necessity of the inclusion of any high precision filter to remove the noise present in the PVDF-based pyroelectric transducer. The high flicker noise level in the low-frequency application based biomedical front-end circuits is a crucial design parameter. Among different topologies for designing the amplifier emphasizing low-noise, low-power design, a folded-cascode OTA is chosen in this work for its simplified architecture. Furthermore, the noise and the power tradeoff for this system has been obtained by current splitting with output branch current scaling technique [26]. Finally, the use of pseudo-resistor based feedback resistor configuration to achieve sub-Hz cut-off frequency reduces the active die area significantly.

This chapter is organized as follows: Section 3.1 describes an overview of the proposed charge amplifier architecture suitable for low-power respiration monitoring applications. The measurement results of the amplifier designed and fabricated using 0.5μm CMOS process and the comparison with other front-end amplifiers are presented in Section 3.2. Similar design architecture is followed for the front-end amplifier which has been realized using 130nm CMOS process, as presented in section 3.3 of this chapter. The following section includes the analysis of the simulation and the measurement data of the amplifier and the OTA, which is then followed by a conclusion in Section 3.5.

3.1 Design of the Charge Amplifier in 0.5µm CMOS Process

3.1.1 System Overview

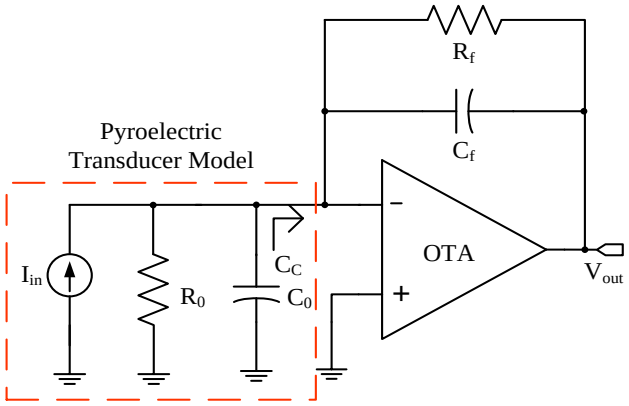

Figure 3.1: Schematic diagram of a typical charge amplifier circuit.

The performance of the front-end electronics such as charge amplifier is crucial for the overall performance of the respiration sensor. A charge amplifier is an interface between the charge signal generated by the transducer and the subsequent signal processing block. It is a current integrator that integrates the charges for a particular duration and results in an output voltage that is proportional to the integrated charge. A conventional charge amplifier is a charge-to-voltage converter with low input and output impedances. The schematic of a conventional charge amplifier is shown in Fig. 3.1 and includes an operational transconductance amplifier (OTA), a capacitor (C_f) and a resistor (R_f) connected in a negative feedback configuration. C_0 is the capacitance of the thin film transducer, which can be modeled as a parallel plate capacitor including a resistance, R_0 to account for the losses associated with the dielectric material. For a PVDF strip of 20mm x 5mm x 20µm in dimension, the value of C_0 is about 0.44 nF and R_0 is in the TΩ range. For efficient charge conversion, the input capacitance (C_c) at the negative node of the charge amplifier is required to be much larger than C_0, so that the charges flow through the lower impedance path. Assuming the feedback factor of the charge amplifier configuration and the open-loop gain of the

OTA are β and A, respectively, then C_c becomes $C_f(1+ \beta A)$. Hence, the equivalent input capacitance of the charge amplifier includes the input capacitance (C_c) of the OTA, which is much larger than C_0 due to the feedback factor [27]. The charge generated by the transducer, Q_{in} is stored across the capacitor, C_f. The input impedance of the charge amplifier requires to be low so that the high equivalent impedance of the pyroelectric transducer does not affect the charge signal even if the impedance of the transducer slightly changes due to the changes in the temperature. The charge generated by the transducer, Q_{in} is stored across the capacitor, C_f. The feedback capacitor is chosen to be much larger than the transducer input capacitance so that the charge transfer process is not affected by other parasitic capacitances at the input node. The input current pulse, I_{in}, or the charge, Q_{in} is generated for a time duration of t seconds from the temperature change due to breathing ($I_{in} = \frac{Qin}{t}$) while the output is a voltage signal, V_{out}. The simplified transfer function of a charge amplifier can be expressed as,

$$V_{out}(t) = -\frac{Q_{in}}{C_f} e^{-t/\tau} \tag{3.1}$$

The input charge, Q_{in} is converted to a voltage signal with a value of $-Q_{in}/C_f$. The working bandwidth of the proposed sensor is characterized by the thermal time constant, τ_{th} of the PVDF material and the electrical time constant, $\tau = (R_0 || R_c)(C_0 || C_c)$, which includes the input impedance of the charge amplifier and the impedance of the equivalent electric circuit model of the transducer. The charge generated by the pyroelectric element is amplified by a factor of $1/C_f$ and is 180^0 out of phase as the input is connected to the inverting terminal of the OTA. The output signal decays following the time constant, τ and the maximum value of the response is a measure of the temperature variation.

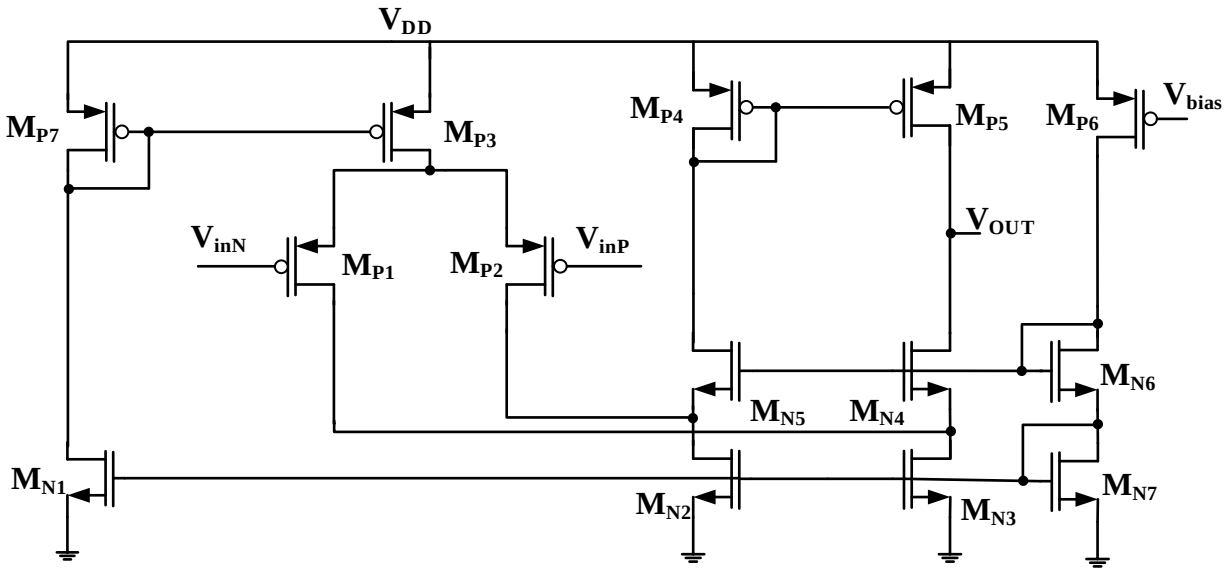

Figure 3.2: Circuit schematic of the PMOS input folded-cascode amplifier.

3.1.2 Charge Amplifier Circuitry

It is of particular importance to design the OTA to exhibit high gain-bandwidth product, high slew rate, and high signal-to-noise ratio to improve the efficiency of the charge conversion. The high open-loop gain and a high input impedance of the OTA in the charge amplifier help achieve efficient charge-to-voltage conversion as well. With these design objectives in mind, a folded-cascode OTA is conceived in 0.5µm CMOS process which is shown in Fig. 3.2. The folded-cascode configuration of the amplifier is chosen to achieve large output swing and high phase margin for stability. The PMOS input pair transistors have been selected to reduce the flicker noise which is present in the sub-Hz breathing signal. Although a telescopic amplifier achieves low power consumption, high gain, higher cut-off frequency, and low input referred noise, its output swing is less than that of the folded-cascode amplifiers. The bias current (I_{bias}) is chosen to be 1.5 µA and the transistor sizes are chosen so as to enable moderate to weak inversion region of

operation to minimize the overall power consumption. The moderate inversion current can be calculated using the following equation [28],

$$I_S = \frac{2\mu C_{ox} V_T^2}{k} \cdot \frac{W}{L} \tag{3.2}$$

where V_T is the thermal voltage ($\frac{k_B T}{q}$) and k is the subthreshold gate coupling coefficient. Typically the value of k is 0.7V or $\frac{1}{n}$, where n is the inverse of the change in surface potential, Φ_s due to the change in the voltage from the gate to the body terminal of the MOSFET [17]. The inversion coefficient can be calculated using the following equation,

$$IC = \frac{I_D}{I_S} \tag{3.3}$$

where I_D is the drain current and I_S is the inversion current of the transistor. If IC is greater than 10, it means that the transistor is operating in the strong inversion region and the transconductance (g_m) is proportional to the square root of drain current. If IC is greater than 0.1 but less than 10, it corresponds to moderate inversion region. Finally, if IC is less than 0.1, the transistor is operating in the weak inversion region and the g_m is proportional to the drain current [29]. Transconductance efficiency ($\frac{g_m}{I_D}$) can be expressed as [29],

$$\frac{g_m}{I_D} = \frac{k}{V_T\,(0.5+\sqrt{IC+0.25})} \tag{3.4}$$

Table 3.1 reports the operating points and dimension of each transistor in the amplifier shown in Fig. 3.2. From the table, it can be seen that the input PMOS transistors M_{P1}, M_{P2} are operating in weak inversion region. The transistors M_{P4}, M_{P5} in the cascode branch are operating in moderate inversion region and M_{N2}, M_{N3} are operating in moderate inversion region.

Table 3.1: Operating Conditions of the Transistors of the Folded-Cascode Amplifier

Transistor	$\frac{W(\mu m)}{L(\mu m)}$	I_D (μA)	IC	$\frac{g_m}{I_D}$ (V^{-1})	$\lvert V_{EFF}\rvert=\lvert V_{GS}-V_{th}\rvert$ (mV)
M_{P1}, M_{P2}	$\frac{60.3}{0.6}$	0.16	0.04	26.85	172.7
M_{N2}, M_{N3}	$\frac{5.1}{0.6}$	0.187	0.22	23.62	126
M_{N4}, M_{N5}	$\frac{12}{0.6}$	0.04	0.02	27.46	17
M_{P4}, M_{P5}	$\frac{120}{0.6}$	0.04	0.056	27.8	274.1
M_{P3}	$\frac{24}{0.6}$	0.3	0.21	23.76	98.1
M_{P7}	$\frac{24}{0.6}$	0.5	0.42	21.24	70.1
M_{N1}	$\frac{4.05}{0.6}$	0.5	0.9	17.87	56.8
M_{P6}	$\frac{1.95}{0.6}$	0.5	4.5	10.44	111
M_{N6}	$\frac{1.5}{0.6}$	0.5	2.1	13.8	10
M_{N7}	$\frac{4.05}{0.6}$	0.5	0.77	18.61	57.3

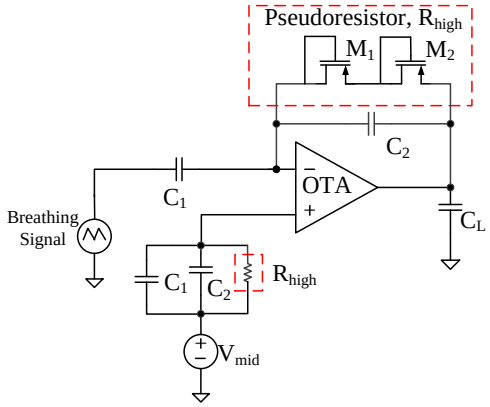

Figure 3.3: Schematic of the folded-cascade OTA.

The schematic of the folded-cascode OTA is shown in Fig. 3.3. Part of this charge amplifier design work has been published in [30], [31]. The OTA block amplifies the breathing signal acquired by the pyroelectric transducer. The op-amp is implemented using the single-stage folded-cascode amplifier as illustrated in Fig. 3.2. An AC-coupling capacitor C_1 of 4.2 pF is used to block the DC signal component of the transducer output and to restore the signal to mid-rail voltage (V_{mid}) which is about 900 mV for the supply voltage of 1.8 V. The capacitance, C_2 and the load capacitance, C_L are chosen to be 1.05 pF and 500 fF, respectively. The mid-band gain (A_0), the lower (f_L) and upper cut-off frequency (f_H) can be expressed as [32]

$$A_0 = \frac{C_1}{C_2} \tag{3.5}$$

$$f_L = \frac{1}{(2\pi \times R_{high} \times C_2)} \tag{3.6}$$

$$f_H = \frac{g_m}{A_0 \times C_L} \quad , given\ C_1, C_L \gg C_2 \tag{3.7}$$

where g_m is the transconductance of the OTA. Transistors M_1 and M_2 act like pseudo-resistors and are configured using diode-connected PMOS transistors having negative V_{GS}. The W/L ratios of M_1 and M_2 are identical ($\frac{6\mu m}{0.6\mu m}$). To achieve an ultra-low cut-off frequency, f_L without using an enormous resistor or capacitor in the feedback and thus occupying a large real-estate area, diode-

connected PMOS transistors M_1 and M_2 are used to emulate large resistances (R_{high}) of up to hundreds of GΩs. These transistors operate at a very low V_{DS} voltage and thus operate in the subthreshold region leaking only the subthreshold leakage current. The subthreshold current can be quantified as follows [33]:

$$I_{sub} = I_0 \exp\left(\frac{V_{GS}-V_{th}}{nV_T}\right)[1 - \exp(-\frac{V_{DS}}{V_T})] \tag{3.8}$$

where V_{th} is the threshold voltage of the transistor, n is the subthreshold slope factor, V_T is the thermal voltage (~25 mV) and,

$$I_0 = \frac{\mu_0 C_{OX} W}{L} \tag{3.9}$$

The incremental resistance is quantified as $\Delta V/\Delta I$. To make sure that the V_{GS} is smaller than the V_{th}, which is around 0.7 V for the 0.5μm CMOS process, it is important to keep the voltage swing across the transistors below the threshold voltage. The two transistors are connected in series with the purpose of further reducing the V_{DS} of each one of them.

As the voltage across the pseudo-resistor changes in small increment, the equivalent resistance increases up to hundreds of GΩs. Fig. 3.4(a) shows the pseudo-resistor configuration. Fig. 3.4(b) shows the difference in current (ΔI) due to the small incremental voltage change (ΔV). Fig. 3.4(c) shows the incremental resistance values of the pseudo-resistors for different ΔV values. From the figure, it can be seen the current is in the pA range for ΔV> -1 V and the resistance value is ~2 TΩ. For example, at 0.3V the incremental resistance is 2 TΩ, which makes the lower cut-off frequency to be 0.76 Hz. The transconductance, g_m of the input pair PMOS transistors is 4.3μA/V^2, which results in an upper cut-off frequency of 2.15 MHz. Since the frequency is much higher than the bandwidth of the breathing signal, it is not as critical as a design parameter compared to the lower cut-off frequency.

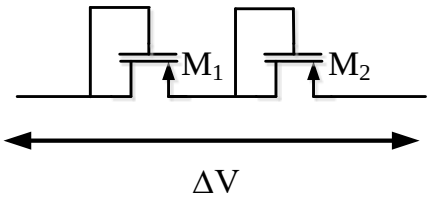

(a)

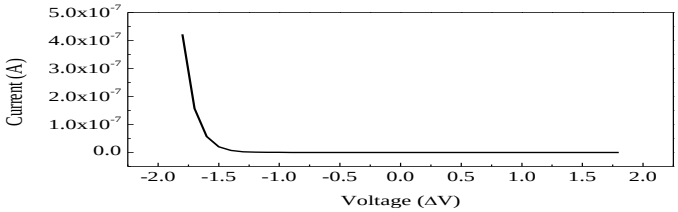

(b)

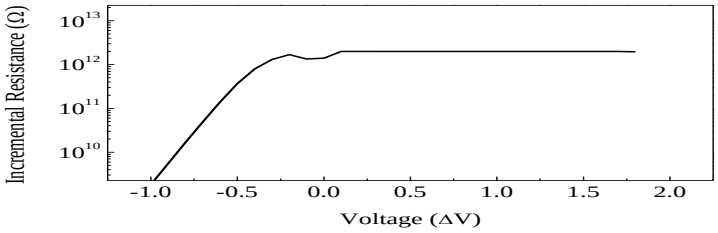

(c)

Figure 3.4: (a) Psuedo-resistor configuration (b) simulation result of the current vs. incremental voltage across the pseudo-resistor and (c) equivalent resistance of the pseudo-resistor for different incremental voltages.

3.1.3 Noise Analysis

In this section, different sources of noise in the charge amplifier circuitry are analyzed and discussed briefly.

3.1.3.1 Thermal Noise

The thermal noise in the CMOS transistors is generated due to the thermal variation in the channel. The thermal noise, modeled as a current source across the MOSFET can be expressed as [28]:

$$\overline{i_{n,th}^2} = 4KT\gamma g_m \tag{3.10}$$

where K is the Botlzmann constant, T is the temperature in Kelvin and γ is the bias-dependent complex noise parameter of the MOSFET. The value of γ varies from 1 to 2/3 depending the value of drain to source voltage, V_{DS}. The thermal noise current presented in equation 3.10 can also be represented as a voltage source at the gate terminal:

$$\overline{v_{n,th}^2} = \frac{4KT\gamma}{g_m} \tag{3.11}$$

3.1.3.2 Flicker Noise

The MOSFETs tend to have more flicker noise (also known as *1/f* noise) compared to the other devices because of their surface conduction mechanism. The flicker noise of the transistor at the drain terminal is expressed as [28],

$$\overline{i_{n,fn}^2} = \frac{K_f}{C_{ox}WL}\frac{g_m^2}{f} \tag{3.12}$$

Or the noise source in terms of the gate voltage,

$$\overline{v_{n,fn}^2} = \frac{K_f}{C_{ox}WL}\frac{1}{f} \tag{3.13}$$

where K_f is the noise parameter that is related to the gate area, C_{ox} is the oxide capacitance, W and L are the width and length of the transistor. The corner frequency, f_{co} is the frequency when the

flicker noise becomes equal to the thermal noise. The total gate referred noise voltage in terms of the corner frequency is [34],

$$\overline{v_n^2} = v_{n,th}^2 + v_{n,fn}^2 = \frac{4KT\gamma}{g_m}(1 + \frac{f_{co}}{f}) \tag{3.14}$$

3.1.3.3 Noise of the Folded-Cascode OTA

The output referred noise of the amplifier shown in Fig. 3.2 mostly comes from the input pair transistors, M_{P1}-M_{P2} and the folded pair, M_{N2}-M_{N3}. The total output referred noise can be quantified as,

$$\overline{v_{n,out}^2} = A_v^2\overline{v_{n,P1}^2} + R_0^2\frac{g_{m,N4}^2}{(g_{m,N4}+g_{ds,P1}+g_{ds,N3})^2}g_{m,N3}^2\overline{v_{n,N3}^2} + R_0^2\frac{g_{m,N4}^2}{(g_{m,N4}+g_{ds,P1}+g_{ds,N3})^2}g_{m,N2}^2\overline{v_{n,N2}^2} \tag{3.15}$$

where A_v is the mid-band gain of the amplifier, R_0 is the equivalent output resistance and $\overline{v_{n,P1}^2}$ and $\overline{v_{n,N3}^2}$ are the gate-referred noise of the transistors, M_{P1} and M_{N3}.

$$A_v = g_{m,P1}R_0\frac{g_{m,N4}}{g_{m,N4}+g_{ds,P1}+g_{ds,N3}} \tag{3.16}$$

The input-referred noise can be derived from equation 3.15 by diving it by A_v^2,

$$\overline{v_{n,in}^2} = \overline{v_{n,P1}^2} + \alpha_3^2\overline{v_{n,N3}^2} + \alpha_2^2\overline{v_{n,N2}^2} \tag{3.17}$$

where α_3 is $g_{m,N3}/g_{m,P1}$ and α_2 is $g_{m,N2}/g_{m,P1}$.

To reduce the overall input-referred noise, the transconductance of the M_{N3} and M_{N2} transistors, $g_{m,N3}$ and $g_{m,N2}$, respectively, are reduced by sizing the MOSFETs to be operating in the moderate inversion region and the transconductance of the M_{P1} transistor, $g_{m,P1}$ is increased by making the transistor operate in the weak inversion region.

The input-referred noise of the front-end amplifier (FEA) in terms of the input-referred noise of the OTA is as follows,

$$\overline{v_{n,in(FEA)}^2} = \left(\frac{C_1+C_2+C_{in}}{C_1}\right)^2 . \overline{v_{n,in}^2} \tag{3.18}$$

where C_{in} is the input capacitance of the amplifier. Therefore, to reduce the overall noise of the amplifier, the input-referred noise of the OTA is reduced. Apart from that, the high aspect ratio of the input pair transistor contributes to the input referred noise of the amplifier, so the W/L ratio needs to be optimized to achieve the best noise performance.

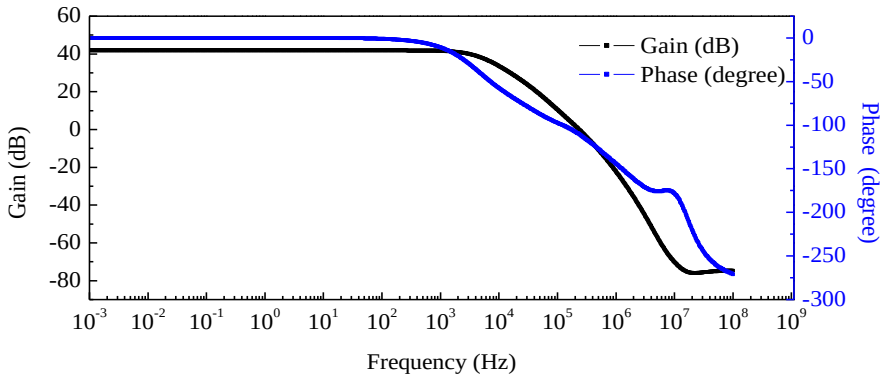

Figure 3.5: Simulation result of the AC analysis of the OTA in Fig. 3.2.

3.2 Simulation and Measurement Results of the Charge Amplifier Designed in 0.5μm CMOS Process

The open-loop gain of the OTA is about 42 dB, which is depicted in the simulation results shown in Fig. 3.5. The simulated offset voltage of the OTA is 13.62mV, which shifts the output DC voltage by ~54.5mV and does not have any impact in the peak-to-peak amplitude of the output signal. Simulation result of the transfer function of the OTA is shown in Fig. 3.6. From the plot, it can be observed that the mid-band gain is about 12 dB and the lower and the upper corner frequencies are 0.05 Hz and 100 KHz, respectively. The phase of the OTA transfer function at unity gain is -68^0, which results in a phase margin of 112^0 thus ensuring high stability. A small signal analysis with 100 mV_{pp} sinusoidal signal has also been performed to determine the mid-

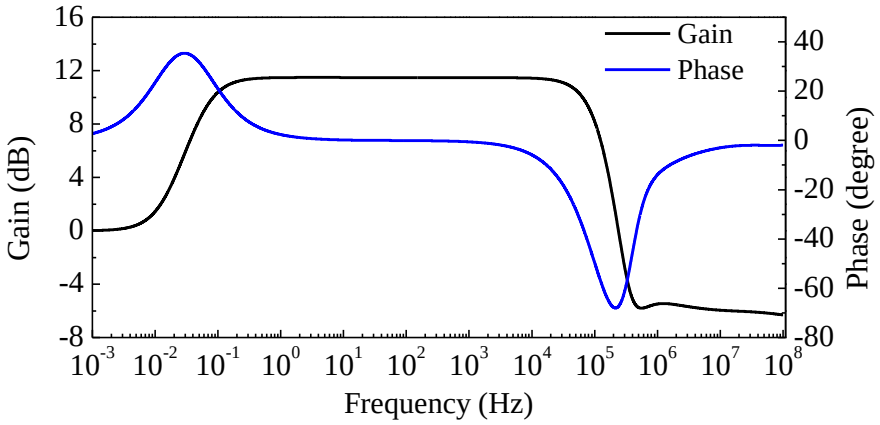

Figure 3.6: Simulated Bode plot of the front-end amplifier in Fig. 3.3.

band gain and the bandwidth of the OTA. The measured closed-loop gain and the phase plots are shown in Fig. 3.7. From the measured data, it can be seen that the lower cut-off frequency is much lower than 1 mHz. HP 33120A waveform generator is used to provide the input signal but the frequency of the input waveform could not be lowered below 1 mHz. The upper corner frequency is 9 kHz, and the measured mid-band gain is 13.62dB. The reason for the gain to be greater than the simulation result can be attributed to the mismatch of the capacitance values in the feedback path. Since the 0.5µm CMOS process does not have PDK capacitor models, all the capacitors were custom made, and the values were extracted from the post-layout simulation. With the addition of the parasitic capacitance, the value of C_1 might have increased which increased the gain slightly. Even though the upper cut-off frequency has shifted in measurement, it is still much higher than the bandwidth of the breathing signal. The phase plot is also depicted in Fig. 3.7. From the phase plot, it can be seen that the phase at unity gain is -92^0 which results in a phase margin of 88^0.

The simulation result of the input-referred voltage noise spectrum of the OTA is depicted in Fig. 3.8. From the figure, it can be noticed that the $1/f$ corner frequency is 0.4 Hz. By integrating

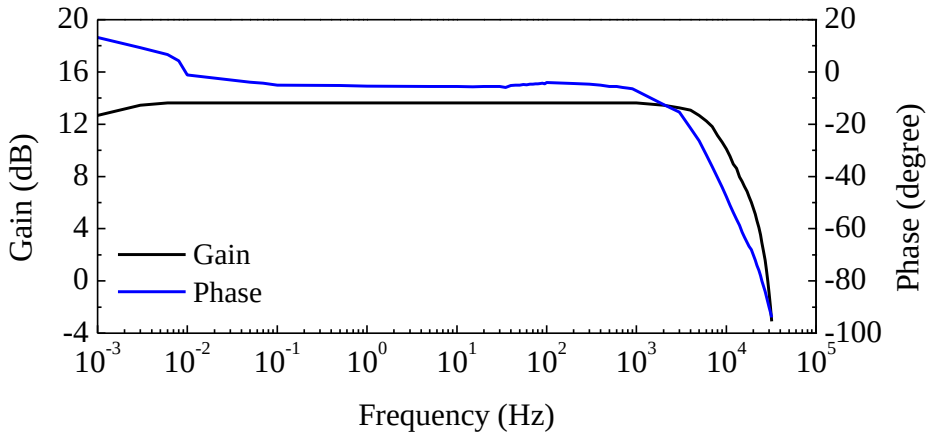

Figure 3.7: Measured closed-loop gain and phase plot of the front-end amplifier in Fig. 3.3.

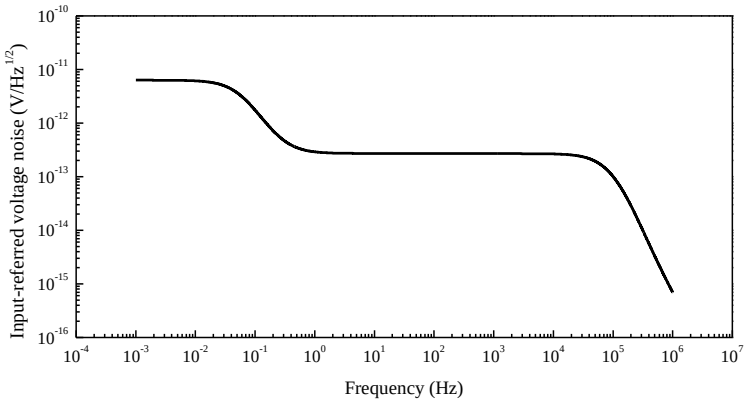

Figure 3.8: Input referred voltage noise spectra simulation of the front-end amplifier in Fig. 3.3.

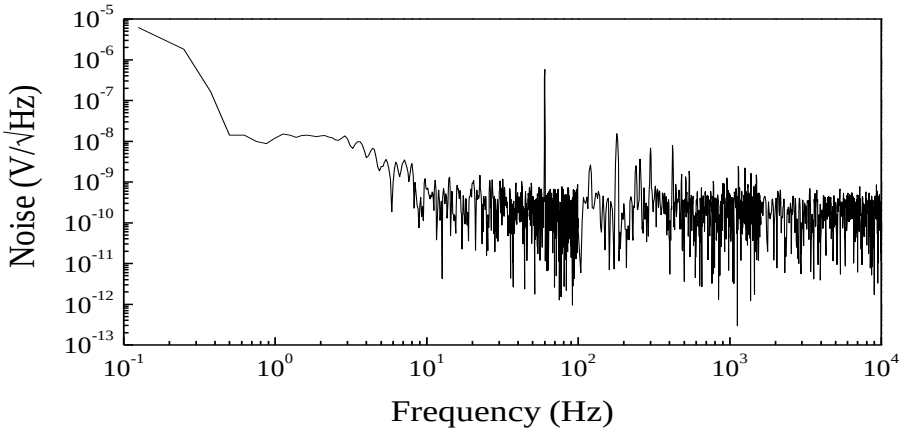

Figure 3.9 : Measured input referred voltage noise spectrum of the front-end amplifier in Fig. 3.3.

the noise curve from 1 mHz to 1 MHz, an RMS noise voltage of 28.7 nV is achieved. Since the RMS value of input referred noise is much lower than the amplitude of the regular breathing signal (400-500 mV_{pp}), the noise performance is suitable for this particular application. The measured input referred noise of the OTA for this design is presented in Fig. 3.9 from which it can be seen that the 1/*f* corner occurs near 10 Hz. The total RMS noise obtained by integrating the curve in the frequency range from 0.125 Hz to 10 kHz is 5.017 μV_{rms} and the noise efficiency factor (NEF) is calculated from the following equation,

$$\text{NEF}=V_{ni,rms}\sqrt{\frac{2I_{total}}{\pi.V_T.4k_BT.BW}} \tag{3.19}$$

where $V_{ni,rms}$ is total input referred noise voltage of the amplifier, I_{total} is the total supply current and *BW* is the amplifier -3dB bandwidth. Substituting these values in the above equation, the *NEF* of the amplifier is obtained to be 3.34. This amount of noise is believed to have less significance in the performance of the proposed system because of the charge generated during breathing is larger than the determined noise by about an order of 5. The front-end of the proposed respiration monitoring sensor includes a thin metalized layer of PVDF of 20mm in length, 5mm in width and

20μm in thickness which is attached to a soft bandage and placed under the nasal cavity of the patient to detect the respiration. Fig. 3.10 shows the achieved breathing signal waveform using the transducer and the proposed charge amplifier in which 400 mV_{p-p} is the average amplitude of the respiratory signal. To observe the frequency domain response of the breathing signal, 1024-point FFT is performed as depicted by Fig. 3.11, from which it can be seen that the frequency of the breathing signal lies in the sub-Hz range.

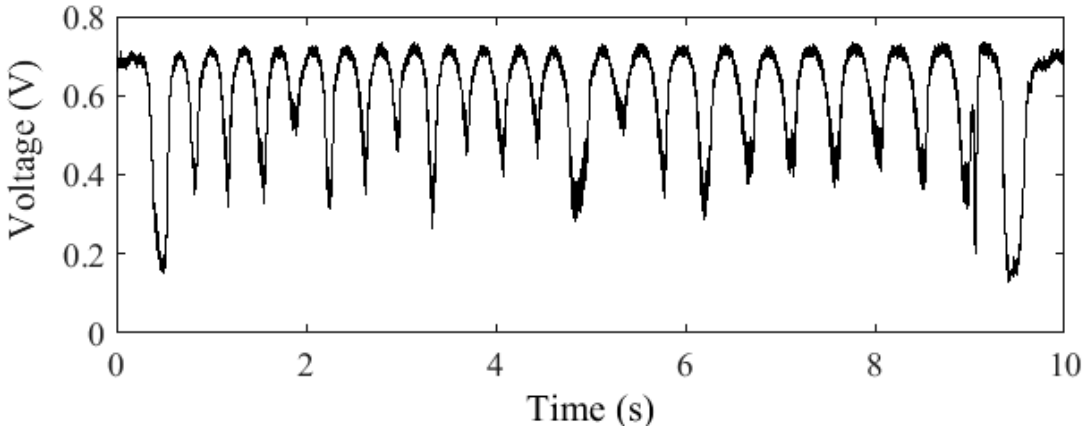

Figure 3.10: Respiratory signal from the charge amplifier output.

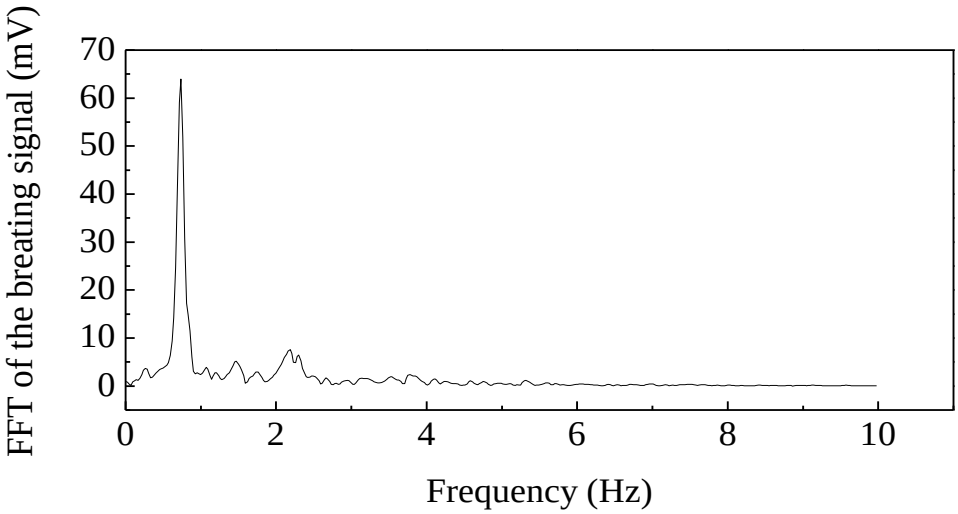

Figure 3.11: FFT of the breathing signal in Fig. 3.10.

The front-end amplifier consumes 5.4 µW of power from a 1.8 V power supply. Fig. 3.12 shows the chip microphotograph of the proposed charge amplifier which occupies an active die area of 0.026 mm^2. The performance of the proposed charge amplifier has been summarized and compared with other published works in Table 3.2. The gain of the amplifier is low compared to the other works but in can be improved by increasing the C_1 to C_2 ratio. The proposed amplifier also has the lowest cut-off frequency that makes it most suitable for application in low-frequency respiratory signal monitoring applications. The input referred noise and NEF are also low enough to detect small changes in temperature due to respiration.

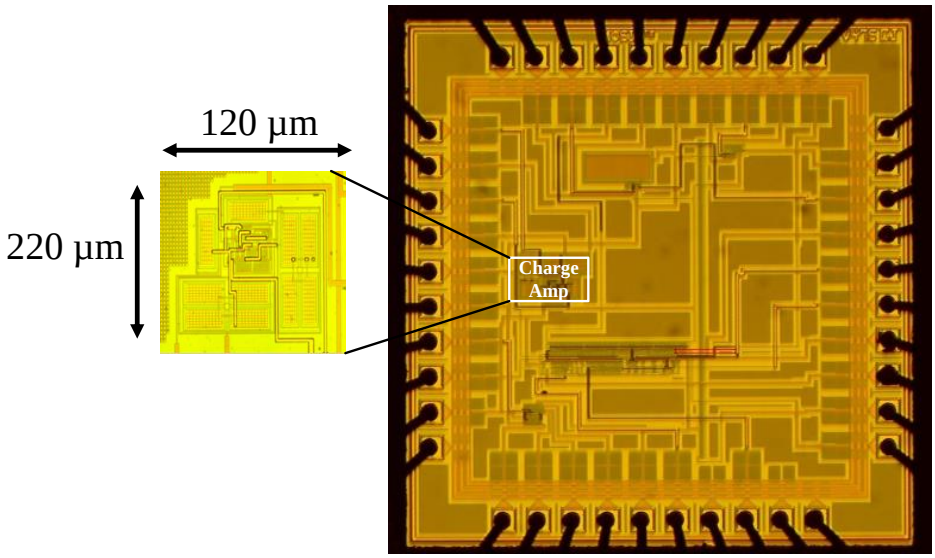

Figure 3.12: Chip microphotograph of the proposed charge amplifier in 0.5µm CMOS process.

Table 3.2: Performance Summary of the Proposed Charge Amplifier

	[17]	[16]	[18]	This work
Power Consumption	80 μW	1.8/3.3 μW	11 μW	5.4 μW
Bandwidth	0.025 Hz-7.2 kHz	0.05 Hz-180Hz	0.3 Hz- 9 kHz	0.001 Hz-10 kHz
Gain	39.5 dB	41/50.5 dB	48/60 dB	13.62 dB
Input Referred Noise	2.2 μV_{rms} 0.5 Hz-50kHz	0.95 μV_{rms} 0.05 Hz – 100 Hz	5 μV_{rms} 1 Hz – 8 kHz	5.017 μV_{rms} 0.125 Hz – 10 kHz
NEF	4	4.6/5.4	4.6	3.34
Die Area	0.160 mm^2	0.7 mm^2	0.065 mm^2	0.026 mm^2
Process	0.5 μm CMOS	0.8 μm CMOS	0.18 μm CMOS	0.5 μm CMOS

3.3 Design of the Charge Amplifier in 130nm CMOS Process

As the transconductance (g_m) of the input pair transistors determines the overall transconductance (G_M) of the OTA, for the 130nm CMOS process NMOS input pair transistors were chosen over their PMOS counterparts. Due to the lower mobility, PMOS transistors have lower g_m compared to the NMOS transistors.

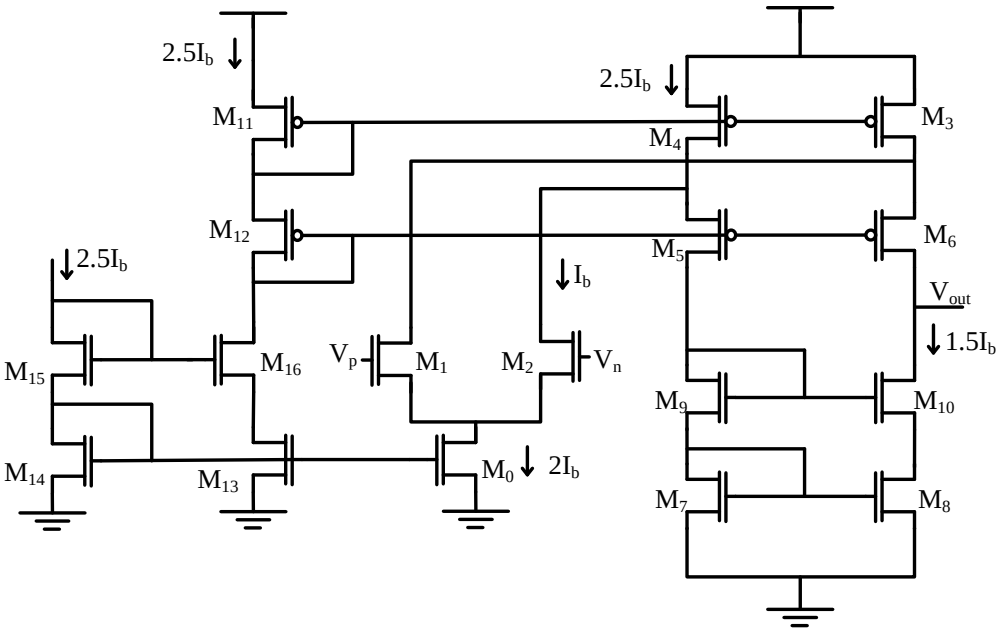

Figure 3.13: Circuit schematic of NMOS input folded-cascode amplifier.

3.3.1 Charge Amplifier Circuit Overview

The OTA (Fig. 3.13) consists of the differential input pair, M_1-M_2, which has a *W/L* ratio of 10µm/0.5 µm. The relatively wide transistors allow the devices to operate in the weak inversion region to achieve the maximum transconductance (g_m) and hence the maximum gain. In the weak inversion region, the transistor has an exponential characteristic and act like a BJT (Bipolar Junction Transistor). The overall transconductance (G_M) of the folded cascode amplifier can be expressed as,

$$G_M = g_{m1,2} = \frac{I_D}{nV_T} \tag{3.20}$$

where I_D is the drain current of the transistor, $V_T = kT/q$, *and* the slope factor, $n \sim 1.2$ in the weak-inversion region. The transconductance efficiency, g_m/I_d is ~34.31V^{-1}. All the current mirror transistors (M_{13}-M_{14}-M_0, M_{15}-M_{16}, M_{12}-M_5-M_6) are designed to be operating in the moderate

inversion region to reduce the noise and increase the output resistance. The transconductance, g_{mCM} of the current mirror transistors is expressed as,

$$g_{mCM} = \frac{I_D}{(V_{GS}-V_{th})} = K(V_{GS} - V_{th}) \tag{3.21}$$

where $K = \mu C_{OX} W/L$. The transistors in the folded branch (M_3-M_4) are biased in the strong inversion region to reduce their noise contribution in the overall circuit. The bias current, I_b is 240 nA, which makes the total power consumption of the amplifier ~1.8 μW. The unity gain frequency, f_0 or the gain bandwidth (GBW) is expressed as,

$$GBW = \frac{g_{m1}}{2\pi C_L} \tag{3.22}$$

The dominating pole frequency is,

$$f_p = \frac{1}{2\pi R_L C_L} \tag{3.23}$$

The maximum gain of the amplifier (without and load resistance) depends on the equivalent output resistance, R_0, which is equal to the parallel combination of the two resistances at the output stage as depicted in the equation 3.15,

$$R_0 = \mu_{10} r_{ds8} \,||\, \mu_6 r_{ds3} \approx \frac{1}{2}\mu r_{ds} \tag{3.24}$$

Then the mid-band open-loop gain becomes,

$$A_{VM} = G_M R_0 \approx \frac{1}{2} g_m \mu r_{ds} \approx \frac{1}{2}\mu_n \mu_p \tag{3.25}$$

3.3.2 Front-End Amplifier Design Considerations

Table 3.3 reports the operating points and the dimensions of each transistor in the amplifier circuit shown in Fig. 3.13. The schematic of the front-end charge amplifier, which consists of the folded-cascode OTA described earlier, is shown in Fig. 3.14.

Table 3.3: Operating Conditions of the Transistors of the NMOS Input Folded- Cascode Amplifier

Transistor	$\frac{W(\mu m)}{L(\mu m)}$	I_D (μA)	IC	$\frac{g_m}{I_D}$ (V^{-1})	$\lvert V_{EFF}\rvert=\lvert V_{GS}-V_{th}\rvert$ (mV)
M_1, M_2	$\frac{10}{0.5}$	0.24	0.008	34.31	105.2
M_3, M_4, M_{11}	$\frac{4}{1}$	0.5	0.825	21.13	8.76
M_5, M_6	$\frac{10}{0.5}$	0.27	0.2	25.9	102.6
M_9, M_{10}	$\frac{120}{0.6}$	0.27	0.06	31.71	27.5
M_7, M_8	$\frac{2}{1}$	0.27	1.32	24.9	56.5
M_0	$\frac{2}{1}$	0.48	0.88	28.02	25.3
M_{13}, M_{14}	$\frac{2}{1}$	0.5	0.52	27.88	25.3
M_{15}, M_{16}	$\frac{5}{1}$	0.5	0.44	30.38	8.2
M_{12}	$\frac{10}{0.5}$	0.5	0.3	24.57	71.4

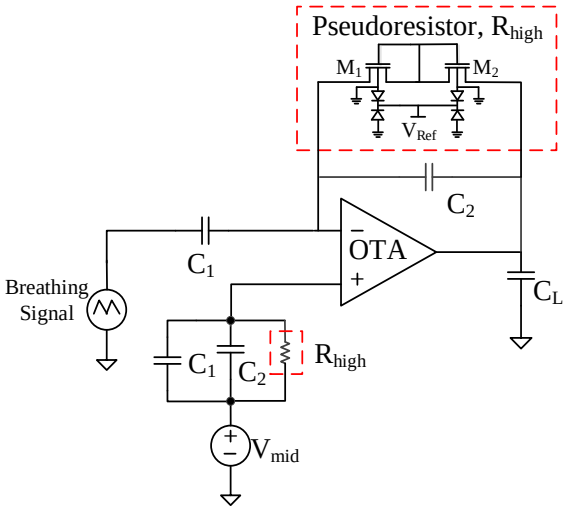

Figure 3.14: Schematic of the folded-cascode OTA with triple-well NMOS pseudo-resistor.

The OTA block amplifies the breathing signal acquired by the PVDF-polymer transducer. An AC-coupling capacitor, C_1 of 1 pF is used to block the DC signal component of the transducer output and to restore the signal to mid-rail voltage (V_{mid}) which is about 600 mV for the supply voltage of 1.2 V. The capacitance, C_2 and the load capacitance, C_L are chosen to be 2 pF and 1 pF, respectively. The design equations for the mid-band gain (A_0), the lower (f_L) and upper cut-off frequency (f_H) are similar to the equations 3.5, 3.6 and 3.7.

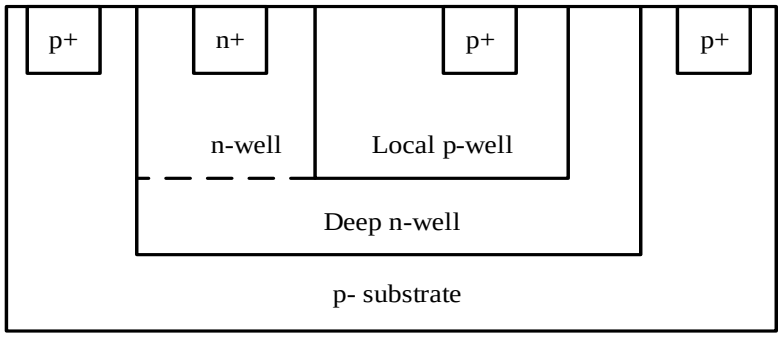

Figure 3.15: Cross-section of an NMOS transistor in a triple-well 130nm CMOS process.

For implementing the pseudo-resistors (M_1-M_2) double-gated *n*-type triple-well MOSFETs with a *W/L* ratio of 0.36 μm/0.24 μm is chosen. It is similar to the pseudoresistor proposed by Holleman *et al.* [35] except the use of two triple-well NMOS transistors. NMOS transistors provide better linearity over the PMOS transistors and to reduce the noise contribution, the substrate of the transistor is isolated by implementing pseudoresistor configuration. The cross-sectional view of the triple-well NMOS transistor is illustrated in Fig. 3.15 which shows that the *p*-well is embedded within a deep *n*-well creating an isolated body for the NMOS from the *p*-substrate. This configuration is efficient because the resistance value can be adjusted by changing the V_{Ref} voltage. As the two diodes in the transistors are connected in an anti-parallel fashion, if the value of V_{Ref} is small, none of the diodes would conduct strongly and the effective resistance would be large. Two transistors are stacked in series to ensure their operating region is within the high-resistance region.

3.4 Simulation and Measurement Results of the Charge Amplifier Designed in 130nm CMOS Process

As the voltage across the pseudo-resistor changes in small increment, the equivalent resistance increases up to hundreds of GΩs. Fig. 3.16(a) shows the pseudo-resistor configuration. Fig. 3.16(b) shows the difference in current (ΔI) due to the small incremental voltage change (ΔV). Fig. 3.16(c) shows the incremental resistance values of the pseudo-resistors for different ΔV values. From the figure, it can be seen that the incremental current change is in the fA range for -1.2 V<ΔV<0.6V range and the resistance value is ~ 0.5 TΩ. The resistance value is almost constant over this range.

The open-loop mid-band gain of the OTA is about 58.18 dB, which is depicted in the simulation result shown in Fig. 3.17. With a load capacitance of 1 pF, the unity gain bandwidth (GBW) and the phase margin are 5.5 MHz and 82.56°, respectively. The high phase margin ensures the stability of the OTA. The simulated input offset voltage of the OTA is 134.03 μV. The simulated design parameters of the proposed folded-cascode amplifier designed in 130 nm CMOS process have been summarized in Table 3.4.

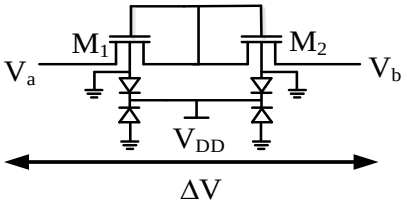

(a)

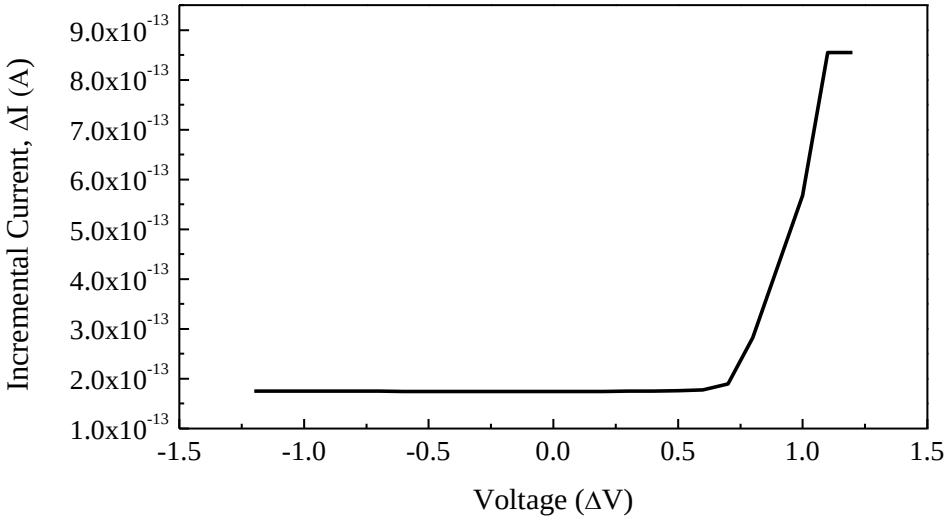

(b)

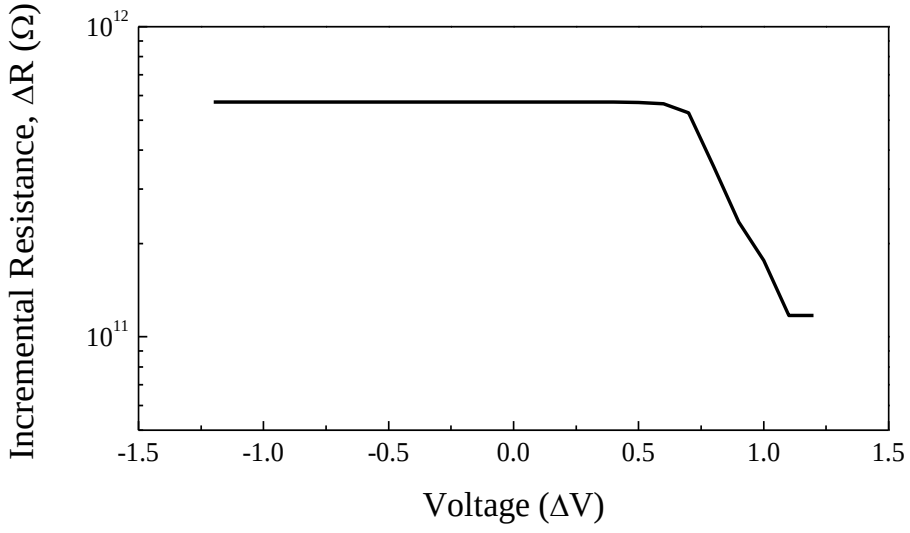

(c)

Figure 3.16: (a) Double gated triple-well NMOS Psuedo-resistor, (b) simulation result of the current vs. incremental voltage across the pseudo-resistor and (c) equivalent resistance of the pseudo-resistor for different incremental voltages.

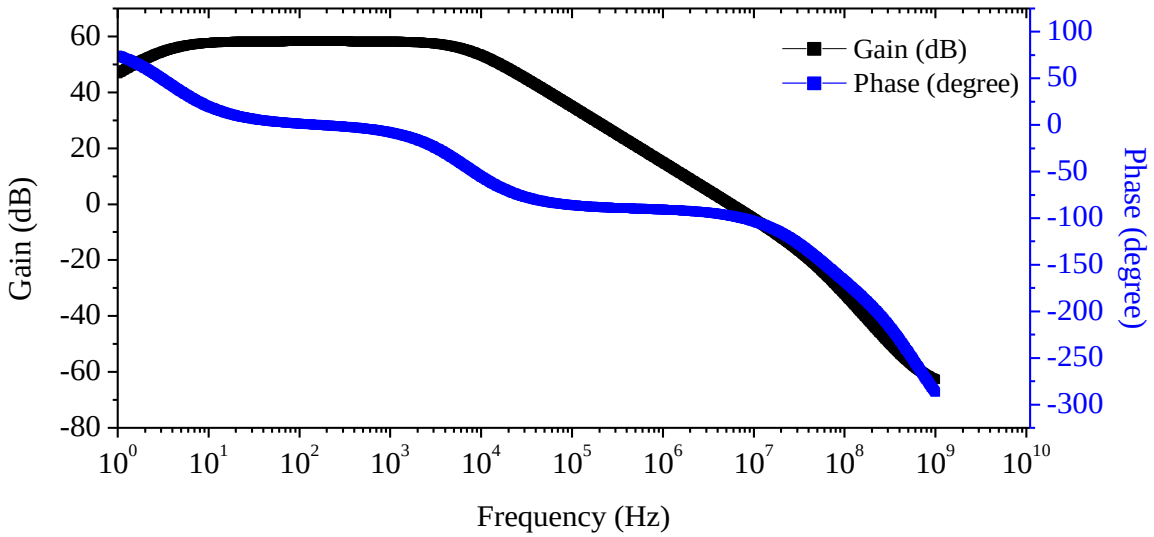

Figure 3.17: Simulation result of the AC analysis of the OTA in Fig. 3.13.

Table 3.4: Simulated Design Parameters of the Folded-Cascode OTA in 130nm Process

Parameters	This Work
Supply Voltage	1.2 V
Current Consumption	1.5 μA
Phase Margin	82.56°
Unity Gain Bandwidth	5.5 MHz
Open-loop Gain	58.18 dB
CMRR	104.37 dB
PSRR	74.62dB
Input Common Mode Range	90 mV – 1.1 V
Slew Rate	3.62 mV/μs

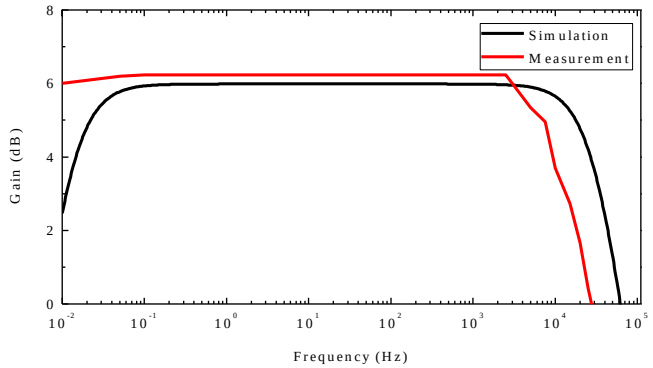

Figure 3.18: Simulation and measurement results of the gain of the front-end amplifier in Fig. 3.14.

Simulation and measurement results of the transfer function of the OTA with feedback are shown in Fig. 3.18. From the plot, it can be observed that the simulated mid-band gain is about 6 dB and the lower (f_l) and the upper (f_h) corner frequencies are 11.2 mHz and 34.7 kHz, respectively with 10 pF load capacitance. The measured mid-band gain is 6.23 dB with f_l is less than 10 mHz and f_h is ~ 13 kHz. A small signal (100 mV_{pp}) sinusoidal signal is used as an input to derive the measured bode plots. The reason for the gain to be greater than the simulation result can be attributed to the mismatch of the input capacitor (C_1). With the addition of the parasitic capacitance, the value of C_1 might have increased which increased the gain slightly. The measured load capacitance (C_L) is also higher than 10 pF due to the parasitic capacitance in the printed circuit board, thus reducing the f_h. Even though the upper cut-off frequency is lower than the simulation result, it is still much higher than the bandwidth of the breathing signal.

Simulation and measurement result of the input-referred voltage noise spectrum of the OTA is depicted in Fig. 3.19. A spike at 60 Hz is also observed in the measurement data due to the supply source noise. By integrating the simulated noise over the 125 mHz to 12.8 kHz bandwidth, a noise voltage of 6.853 µV or 4.847 µVrms is calculated. Since the RMS value of

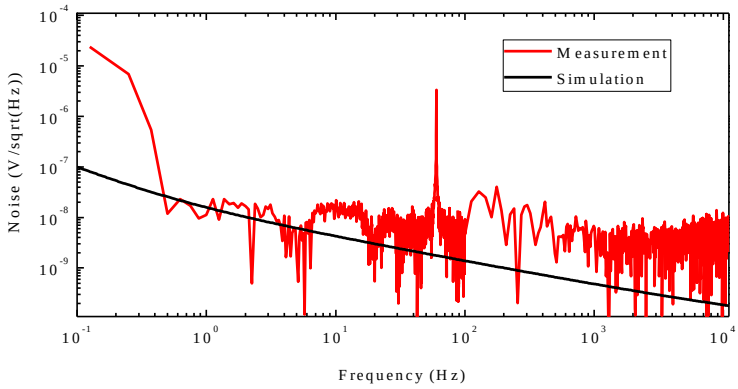

Figure 3.19: Simulation and measurement results of the input-referred noise of the front-end amplifier in Fig. 3.14.

input referred noise is much lower than the amplitude of the regular breathing signal (400-500 mV_{pp}), the noise performance is suitable for this particular application. From the measured input referred noise it can be seen that the *1/f* corner occurs near 0.4 Hz. The total RMS noise obtained by integrating the curve in the frequency range from 0.125 Hz to 12.8 kHz is 6.54 μVrms. The noise efficiency factor (NEF) calculated from equation 3.18 is 2.79.

To record the respiration signal the thin metalized layer of PVDF which is attached to a soft bandage is placed under the nasal cavity to detect the respiration signal. Fig. 3.20(a) shows the achieved breathing signal waveform using the transducer and the proposed charge amplifier. As the transducer is placed near the nasal cavity, the highest peak-to-peak amplitude is almost 1.1 V_{pp}. When the fabricated cannula with the PVDF sensor is used as the breathing sensor, the peak-to-peak amplitude of the breathing signal is reduced to 400 mV_{pp} (Fig. 3.20(b)). To observe the frequency domain response of the breathing signal, 1024-point FFT is performed as shown in Fig. 3.21, from which it can be seen that the frequency of the breathing signal lies in the 1-2 Hz range. Since the final goal is to implement the cannula based respiration monitoring sensor specifically for neonatal infants in a hospital settings, the performance of the transducer placed inside the cannula as well as the charge amplifier satisfies the design specifications efficiently.

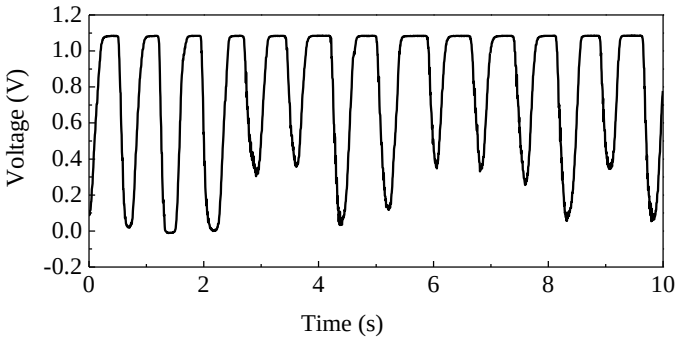

(a)

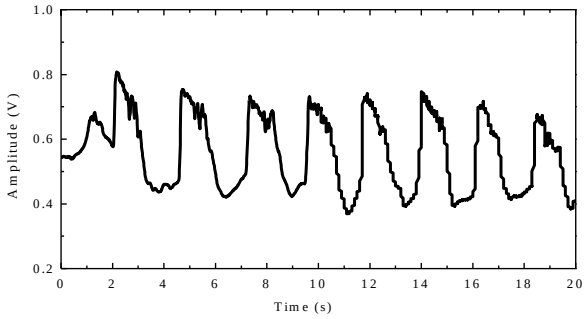

(b)

Figure 3.20: Respiratory signal from the front-end amplifier in Fig. 3.14 using, (a) PVDF strip and (b) cannula.

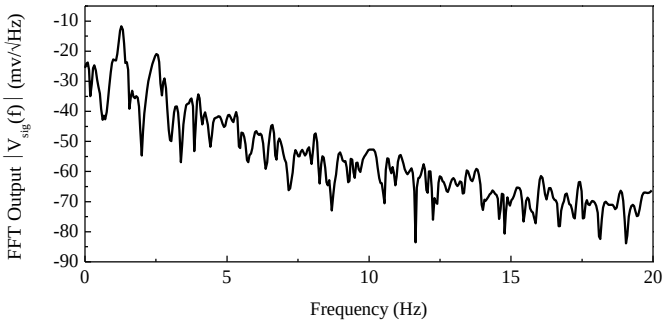

Figure 3.21: FFT of the breathing signal in Fig. 3.20 (a).

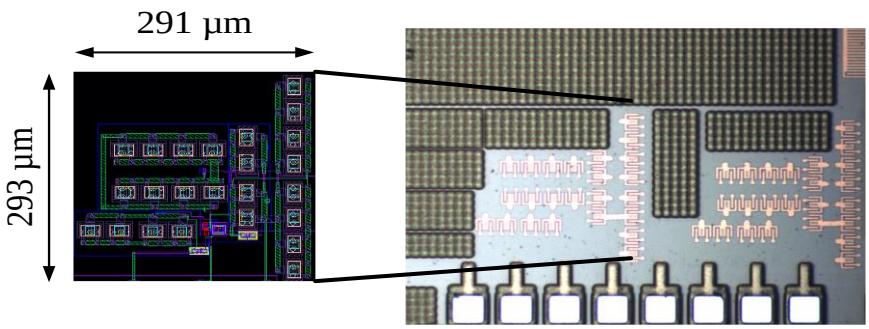

Figure 3.22: Chip microphotograph of the proposed charge amplifier in 130nm CMOS process.

The front-end amplifier consumes 1.8 µW of power from a 1.2 V power supply. Fig. 3.22 shows the chip microphotograph of the proposed charge amplifier designed using 130nm CMOS process which occupies an active die area of 0.085 mm^2. The measured performance parameters of the proposed front-end amplifier designed in 130nm CMOS process have been summarized and compared with other state-of-the-art works in Table 3.5. From the table, it can be seen that the power consumption for the proposed amplifier designed with a supply voltage of 1.8 V is very low compared to the other works as well as the previous amplifier designed in which 0.5 µm CMOS process. The proposed amplifier also has the lowest cut-off frequency that makes it most suitable for application in low-frequency respiratory signal monitoring. The NEF is also the lowest compared to other designs because of the low bias current.

Table 3.5: Performance Summary of the Proposed Charge Amplifier

	[17]	[16]	[18]	This work
Power (μW) Consumption	80	1.8/3.3	11	1.8
Bandwidth	0.025 Hz-7.2 kHz	0.05 Hz-180Hz	0.3 Hz-9 kHz	10 mHz-13 kHz
Gain (dB)	39.5	41/50.5	48/60	6.23
Input Referred Noise (μV_{rms})	2.2 (0.5 Hz - 50 kHz)	0.95 (0.05 Hz - 100 Hz)	5 (1 Hz - 8 kHz)	6.54 (125 mHz - 12.8 kHz)
NEF	4	4.6/5.4	4.6	2.79
Die Area (mm^2)	0.160	0.7	0.065	0.08
CMOS Process	0.5 μm	0.8 μm	0.18 μm	130 nm
CMRR (dB)	83	100	48	104.37
PSRR (dB)	85	-	55	74.62

3.5 Summary and Conclusion

Two low-power low-noise fully integrated charge amplifiers designed in 0.5μm and 130 nm standard CMOS processes, respectively, are presented in this chapter. The proposed charge amplifier designed in 0.5μm CMOS process features low power consumption of 5.4 μW and very low input referred noise of 5.017μV_{rms} along with the lower cut-off frequency of 1 mHz obtained by a pseudo-resistor based diode-connected MOSFET in the feedback configuration. These features make this charge amplifier a potential candidate to be used as the front-end circuitry of a respiration monitoring system using pyroelectric transducer. A brief noise analysis of the amplifier is also presented with the design optimizations for lowering the input-referred noise. Measured data presented in the paper shows that the proposed folded-cascode configuration for the OTA has achieved a significant improvement over the conventional OTA designs regarding the noise-power trade off. To reduce the power consumption even further, the charge amplifier is also designed using 130nm CMOS process. With a power consumption of only 1.8 μW, the amplifier has a -3

dB bandwidth of 10 mHz to 13 kHz and a NEF of 2.79. The high CMRR value also ensures that the common mode noise is rejected and filtered out at the input.

Chapter 4 Overview of Impulse Radio Ultra-Wideband (IR-UWB) Transmitter

It is of crucial importance to design a transmitter that operates in the desired allocated spectrum and does not interfere with the co-existing bands. Similarly, interference from other bands can significantly deteriorate the radio performance. To minimize this problem as much as possible Federal Communications Commission (FCC) has limited the radiation characteristics of a radio operating in certain bands. Unlike GSM or CDMA which operate in a licensed spectrum, FCC has also approved many unlicensed bands where the radio only needs to comply with the emission mask. Since 2002 when FCC allocated 3.1 to 10.6 GHz of the frequency spectrum as ultra-wideband, many transmitter designs have been reported with a pulse generator and an oscillator to up-convert the baseband signal to RF signal [36], [37]. For a commercial wearable sensor such as the respiration monitoring system discussed in Chapter 2, the cost is also an important factor, which can be minimized by making the wireless telemetry operate in the unlicensed ultra-wideband (UWB) spectrum. In this chapter, the UWB emission mask imposed by the FCC is studied and the design of the impulse radio ultra-wideband (IR-UWB) transmitter that follows the spectral mask constraints is discussed.

4.1 UWB Communication and FCC Spectral Mask

Pulsed-based communication requires a broad bandwidth as the narrow impulse signal in the time domain corresponds to a wider bandwidth in the frequency domain. That is why this type of communication is also known as ultra-wideband (UWB) communication. Traditional continuous wave (CW) signal is also referred to as a narrowband signal as the frequency bandwidth is very low. According to the FCC regulation, the fractional bandwidth of the emitted signal is

required to be either 500 MHz or 20% of the carrier frequency to be considered as UWB signal [38]. The fractional bandwidth is defined as, $\frac{f_h - f_l}{f_c}$, where f_h and f_l are the upper and the lower -10dB cut-off frequencies, respectively and f_c is the center frequency. Because of the narrow pulse nature of the UWB communication, it is possible to accurately localize a subject (for example senior citizen for assisted living) [39] or even monitor the rhythmic chest movement due to respiration [40]. It has also been extensively utilized for high-data rate communication applications. Chae *et al.* demonstrated a neural recording system for neuron spike extraction with 128 recording channels and 90 Mbps data rate [41]. All these unique features of UWB communication offer many attractive areas of research.

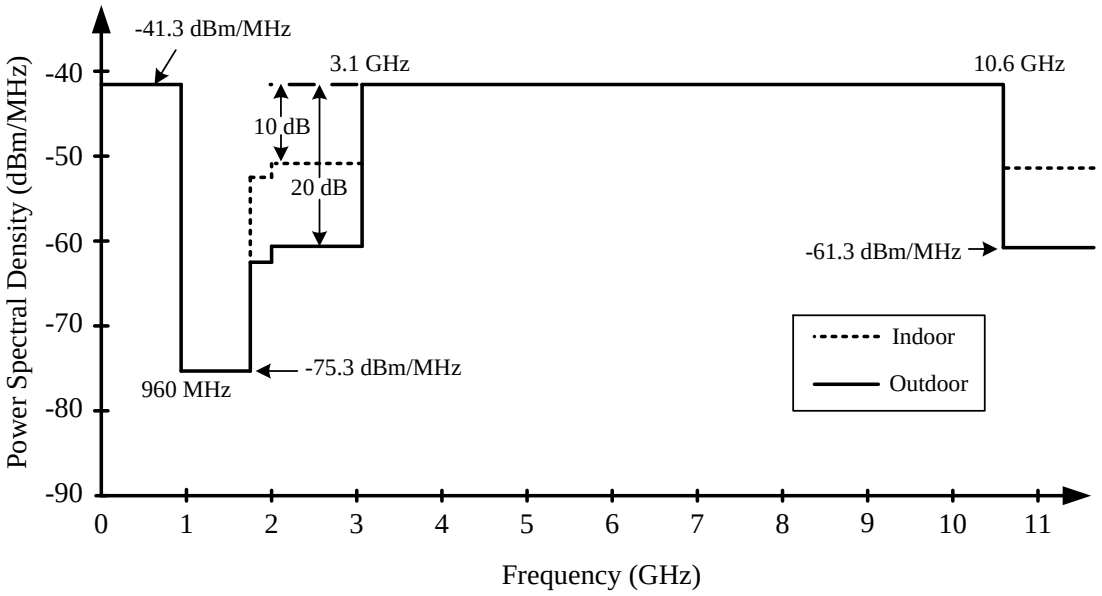

Figure 4.1: FCC mask for UWB communication.

In February 2002, FCC released a regulation for the UWB communication power spectrum emission. Fig. 4.1 shows the FCC spectral mask for UWB communication. According to the FCC regulation, the maximum emission power must not exceed -41.3 dBm/MHz. The reason for this restriction is to assure that a UWB device does not interfere with other medical devices operating

in the Wi-fi or Bluetooth frequency bands because of its low transmission power. FCC has also imposed an even higher restriction on the emission mask for outdoor communication compared to indoor communication so that there is no interference with cellular or aircraft radar communication. A deep notch around 1.5 GHz is imposed not to create interference with the Global Positioning System (GPS). Thus, the UWB communication does not impose any interference with the existing bands such as 2.4 GHz ISM band. Because of the lower emission power the range of communication is also limited to a distance of less than 10 meter.

4.2 UWB Pulse Shaping Techniques

Many approaches have been studied over the last one and a half decade to implement the pulse shaping technique to achieve the desired UWB spectrum that follows the FCC mask regulation. These approaches can be broadly categorized as the carrier based and carrier-less UWB communication. For a carrier-less UWB radio, the pulse spectrum falls within the 0-960 MHz or 3.1 -10.6 GHz bandwidth, without the requirement of RF up-conversion. The duration of the pulse is less than 1 ns with one or more Gaussian function like wavelets. Impulse generators have been implemented that generate Gaussian waveform or its derivative for carrier-less UWB communication. A filter is sometimes incorporated after the pulse generator to make sure the power spectrum lies within the FCC spectral mask [42]. The higher order derivative of the Gaussian pulse has sharper roll-off which helps meet FCC spectrum regulation without using any additional filter. Kim *et al.* presented a 5^{th} derivative Gaussian impulse waveform generator using a digital CMOS circuitry that does not require any additional filtering and occupies 7.2 GHz of the bandwidth [43]. It is difficult to calibrate the variations of standard deviation parameters and the derivative order of the Gaussian wavelet due to process and temperature variation (PVT), violating the FCC spectral mask regulation. In the carrier-based UWB communication system, the UWB

spectrum is sub divided into several bands, each with a bandwidth of 500 MHz or higher, as shown in Fig. 4.2. Carrier-based UWB communication enables multi-user application such as where each user would be assigned particular center frequency and bandwidth in the multi-band UWB system. In the sub-banded UWB system, the baseband data is first converted to a particular pulse shape, (e.g. triangular, *sinc*, square, *tanh* etc.) with narrow width and then the wavelet is up-converted by a local oscillator (LO) with the help of a mixer, as shown in Fig. 4.3.

In order to choose the right pulse shaping that would be optimum for any particular application designers first have to look into the spectral efficiency, out-of-band emission and side-lobe rejection of each shape. Spectral efficiency or bandwidth efficiency is a measure of how efficiently the spectrum of the pulse wavelet occupies a given bandwidth. If the data rate is *R* and the bandwidth is *B*, then the spectral efficiency is defined as $\frac{R}{B}$ (bits per second per Hz). The *sinc* shaped pulse has a spectral efficiency of 100% due to having rectangular spectrum in frequency domain while the square-shaped pulse has a spectral efficiency of only 58% due to having *sinc* shaped spectrum [44]. Out-of-band emission is also an important factor while choosing the optimum pulse shaping. Out-of-band emission is the power emitted by the transmitter in the adjacent channel which would possibly interfere with other radio communication in the nearby frequency bands. The *sinc* wave shape has 0% out-of-band emission while the square wave has 12.8% (-8.9 dB) out-of-band emission [44]. Side-lobe rejection primarily displays the severity of the out-of-band emission. It is the difference of the power emitted in-band and out-of-band. The *sinc* and the Gaussian waveforms have no side-lobes and the side-lobe rejection for square-shaped wavelet is -13 dB [44]. In this work, both triangular pulse shaping and *sinc* pulse shaping are presented.

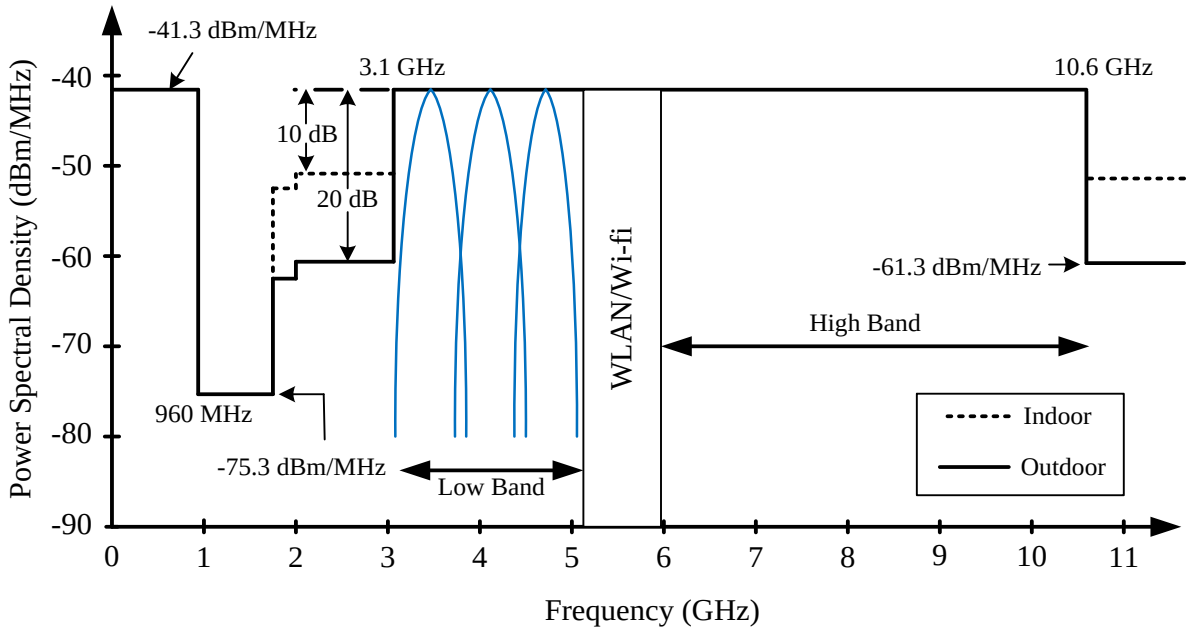

Figure 4.2: FCC mask for UWB communication.

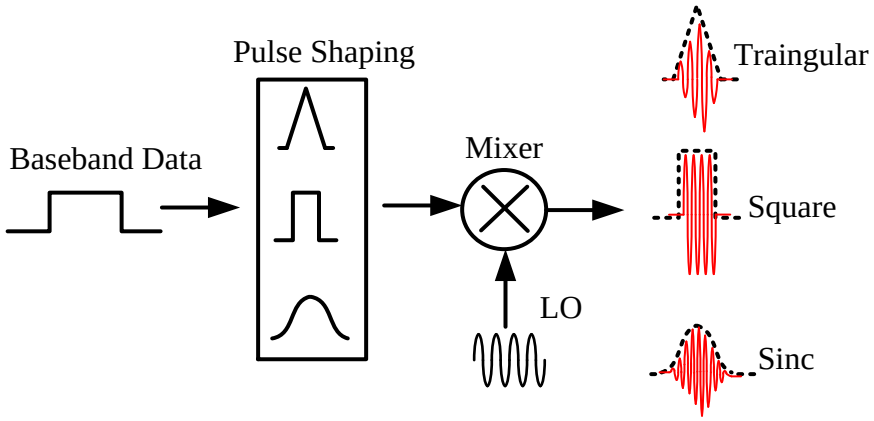

Figure 4.3: Carrier-based UWB wavelet generation scheme.

4.3 Impulse Radio UWB Transmitter for Low-Data Rate Application

For any biomedical sensor such as the respiration monitoring sensor described in chapter 2, the transmitter is expected to transmit data wirelessly at a steady low-data rate. Since the transmitter usually consumes most of the power of a sensor system, any reduction in the power consumption of the transmitter block is expected to save the overall power consumption by tenfold. To reduce the average power consumption, it makes sense to duty-cycle the radio communication as much as possible, so that the transmitter is on for a short period and thus dissipating power only when it is active.

Fig. 4.4 (a) shows the duty-cycling approach, where the transmitter is turned off most of the time, thus dissipating only the leakage current. Unlike conventional continuous wave (CW) transmitter where data is encoded by the phase or the frequency of the carrier waveform, the UWB data can be encoded using short duration pulses. This type of radio communication is known as impulse radio ultra-wideband (IR-UWB) because of their pulsed nature. It is the transmission of very low energy narrow pulses (in the range of sub-nanoseconds to few nanoseconds) with fine time resolution. IR-UWB has been a popular choice for high-data rate application for its wide bandwidth nature. For the CW transmitters or the duty-cycled IR-UWB transmitter, the static power (leakage and overhead power) consumption is fixed no matter what the data rate is. It is the dynamic power that increases with the increasing data rate. The dynamic power can be expressed as the product of E_b and R, where E_b is the energy per bit and R is the data rate. For an IR-UWB transmitter, E_b is much lower than a CW transmitter, thus resulting in a reduced overall power consumption of the transmitter (Fig. 4.4 (b)). For the receivers in wearable biomedical sensor applications most of the time there are not much of a power restriction ensuring that the receivers are always active for communication. For IR-UWB communication many modulation schemes

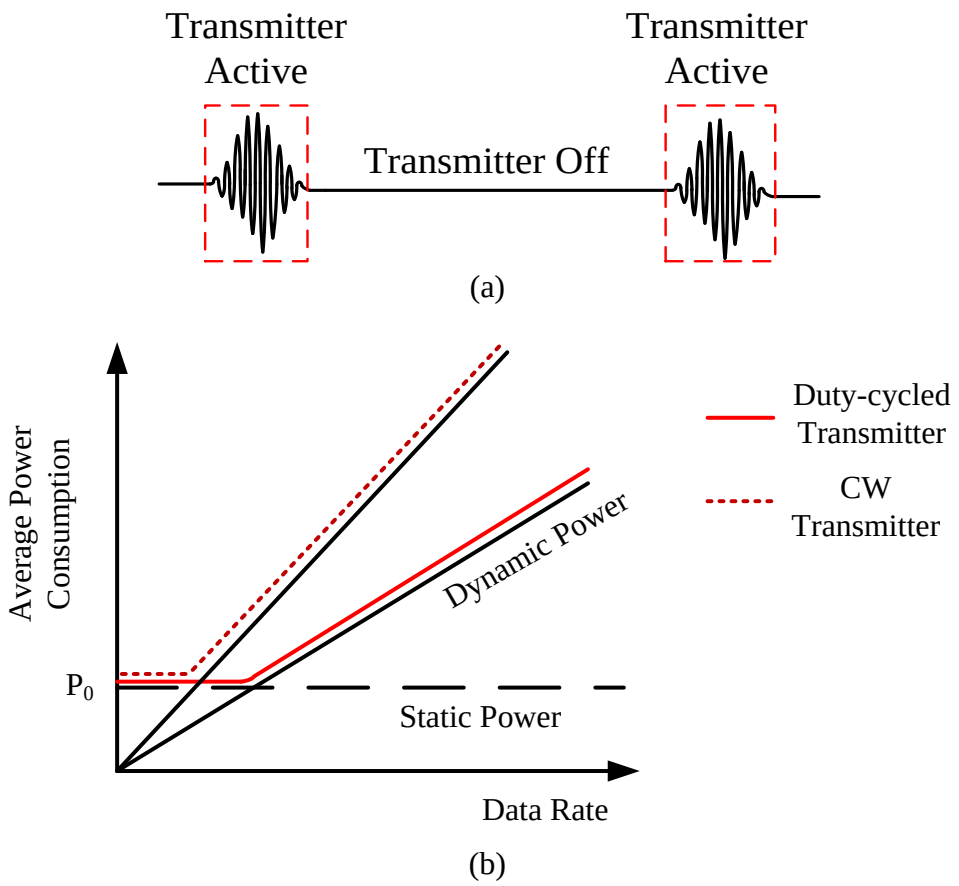

Figure 4.4: (a) Transmitter duty-cycling approach and (b) static and dynamic power consumption of duty-cycled and CW transmitter.

such OOK (on-off-keying) [36], pulse amplitude modulation (PAM) [45], binary phase shift keying (BPSK) [46], pulse position modulation (PPM) [47] have been investigated. With the motivation of achieving simplicity in transmitter architecture and low-power design, OOK modulation is an ideal candidate for low-data rate applications. In a hospital environment, as the data is transmitted from multiple sensor nodes, the carrier based IR-UWB architecture operating in 3.1 to 5 GHz frequency range with OOK modulation scheme is chosen for the transmitter design. CMOS process has been selected for the design of the transmitter considering its availability and low cost of fabrication. The next section describes the transmitter architecture that was designed and fabricated using 180nm high voltage CMOS and 130nm RF CMOS processes, respectively.

4.4 Radio Implementation Using Decawave DWM1000 Module

To establish a proof-of-concept design a commercially available off-the-shelf UWB transceiver module (Decawave DWM 1000 IEEE 802.15.4-2011 UWB transceiver module) [48], [49] and ARM Cortex-M3 SAM3S Microcontroller IC [50] are used to digitize and transmit the data acquired from the charge amplifier designed in 0.5 µm CMOS process. The performance of the charge amplifier and the PVDF transducer for respiration monitoring is discussed in the previous chapter. Although Decawave DWM1000 module has been used extensively for UWB ranging and positioning applications [51], [52] it has not been used for wireless communication for biomedical application. Fig. 4.5 shows the overview of the proposed system. There are total 10 analog I/O ports for the ADC in the microcontroller IC and the output of the charge amplifier goes to the ADC1 port. The respiration signal output from the charge amplifier is sampled at 1 kSps rate and the ADC converts the sampled data to an 8-bit digital data with 1 stop bit and no parity bit. The Decawave transceiver modules were placed 2 feet apart for the data communication. Table 4.1 lists the different operation modes of the transceiver module [51].

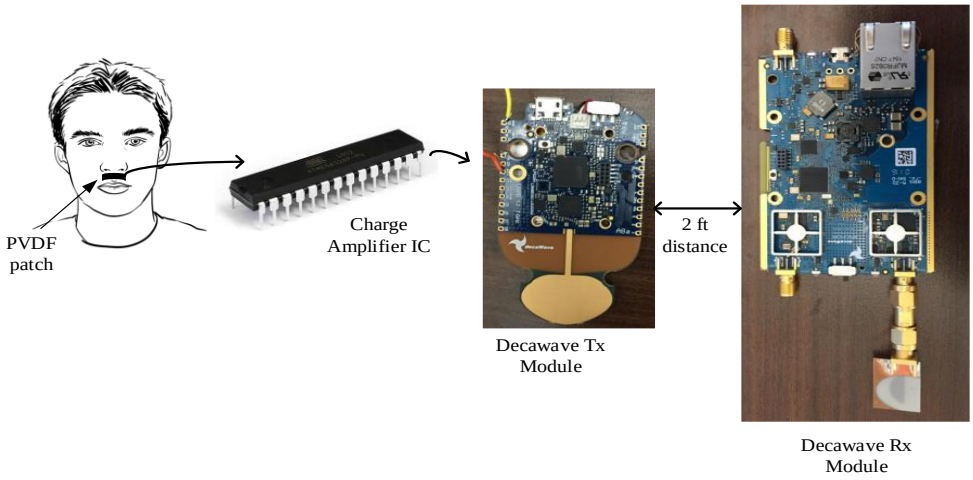

Figure 4.5: Overview of the proposed system with PVDF transducer, CMOS charge amplifier IC, Decawave DWM10000 transmitter and receiver module.

Table 4.1: Operation Modes of the DecaWave DWM1000 Module

Mode	Carrier Frequency (GHz)	Data Rate (bps)	Bandwidth (MHz)	Preamble (bit)	PRF (MHz)
1	4	110k	500	1024	64
2	4	6.8 M	500	128	64
3	6.5	110k	500	1024	16
4	6.5	6.8 M	500	128	16
5	6.5	110k	900	1024	64
6	6.5	6.8 M	900	128	64

Mode 1 (4 GHz carrier frequency and 110 kbps data rate) is selected for transmitting the data and 50 packets of data are transmitted per second (each packet having a maximum of 26 bytes of data). The receiver tag is placed at a distance of 2 feet (0.61 m) from the transmitter module. Fig. 4.6 shows the digitized breathing signal at the transmitter end and the Fig. 4.7 shows the received signal at the receiver end. While the breathing signal patterns look pretty similar, there is approximately 2-4 seconds of a time lag between the transmitted and the received signals. Even after aligning the highest peaks of the two signals, the other peaks are at different time stamps. Since the data is sent when the output buffer is full (50 packets of data in this case) this may contribute to a delay. According to the data sheet, the receiver sensitivity at the data rate of 110 kbps is -102 dBm/500 MHz with 1% packet error rate. Apart from that, the peak amplitudes of the transmitted and the received signals look pretty similar. To minimize the delay between the transmitted and the received signals, a calibration can be made by cross-correlating the two signals and advancing the received signal as needed. The effective update rate at the receiver-end is limited and is lower than the update rate at the transmitter due to packets being discarded or corrupted.

The transmitter module antenna is a planer monopole antenna by DecaWave with a gain of 2.2 dBi at 4 GHz frequency. It is an omni-directional antenna with a operating frequency bandwidth 3- 6 GHz. The receiver module antenna is also an omni-directional planer monopole antenna. It has a gain of -2.4 dBi at 3.5 GHz and an operating frequency bandwidth of 3.6 - 10 GHz. With a 500 MHz bandwidth, the peak emitted power by the transceiver module is about -12 dBm. The transceiver modules consume 520 mWs of power with 3.3 V supply voltage which is supplied by the 3.7 V 1000 mAh Li-poly battery.

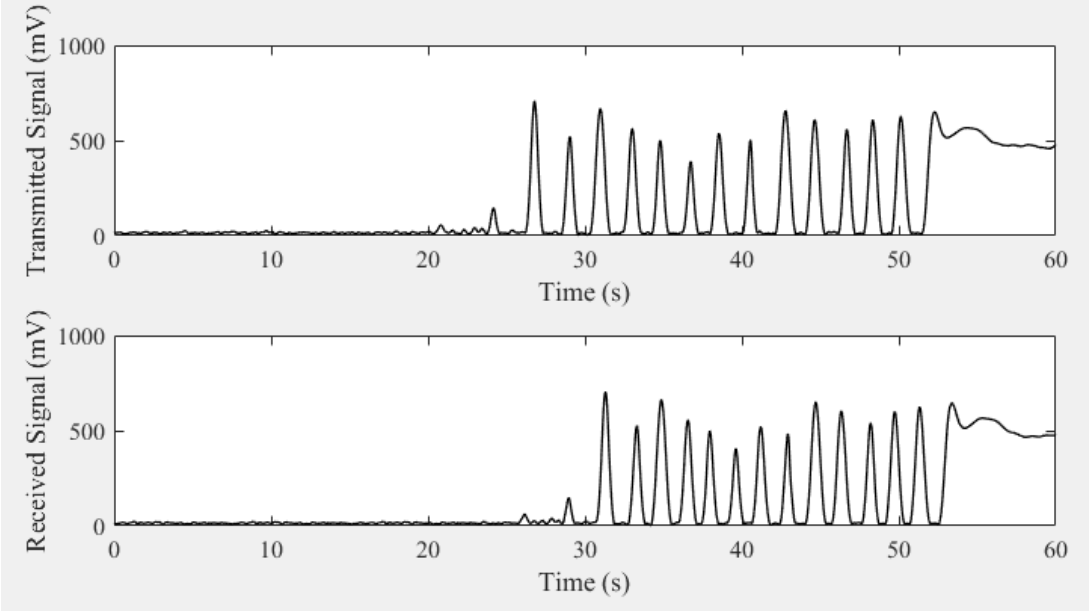

Figure 4.6: ADC output from the transmitter module (top) and receiver DAC output (bottom).

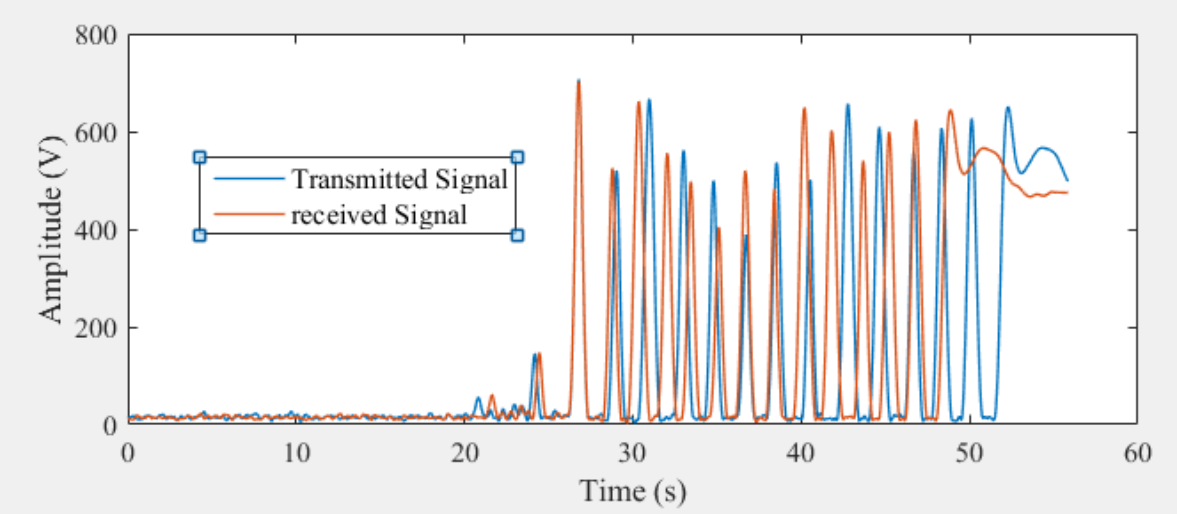

Figure 4.7: The transmitted and the received signals after the highest peaks are aligned.

4.5 Summary and Conclusion

In this chapter, a brief overview of the UWB communication is presented, along with an introduction to the spectral mask regulation imposed by FCC in 2002. Different pulse shaping techniques and their pros and cons in terms of spectral efficiency, side-lobe rejection, and out-of-band emission are presented. Later in the chapter, the feasibility of IR-UWB communication as a potential low-power low-data rate transmitter is analyzed. Finally, the chapter concludes with a proof-of-concept UWB communication system implemented using the Decawave DWM1000 transceiver module, ARM Cortex-M3 SAM3S Microcontroller by Atmel, the front-end amplifier IC and the pyroelectric transducer. While there is a timing mismatch between the transmitted and the received signals, the respiration signals have the same amplitudes of peaks. To reduce the high power consumption of the commercially available transceiver module, in the following chapters low-power IR-UWB transmitter design schemes are presented.

Chapter 5 Low-Power Voltage Controlled Oscillator and Driver Circuitry

5.1 Low-Power Voltage Controlled Oscillator

Voltage controlled oscillator (VCO) is widely used in the communication system of a radio transceiver circuit and plays a critical role as a clock generator and in RF circuits. The performance of the VCO in terms of phase noise and tuning range determines the overall performance of a transceiver. The current trend towards multiband transceiver architecture and the broadband system has led to the interest of VCOs with a broad tuning range and low phase noise performance [53]. Even though relaxation oscillators can easily achieve very wide tuning range, their poor phase noise performance make them unsuitable for various wireless applications. An LC VCO is chosen mainly for its good phase noise performance compared to ring oscillators or other types of relaxation oscillators. VCO is one of the key blocks of radio-frequency (RF) communication circuits, which are primarily used for up-converting the baseband signal in the transmitter-end and down-converting the high-frequency carrier signal in the receiver-end. Designing CMOS VCO requires the designer to optimize various parameters such as tuning range, power consumption, phase noise, output power etc. depending on the intended application. As the LC oscillators demonstrate better spectral purity over the ring oscillators, they are mostly used in high-frequency communication circuits. It is even more important to achieve low jitter for the proposed time domain carrier based IR-UWB transmitter architecture [54].

The output of the VCO is usually a periodic voltage signal and the oscillation sustains for an indefinite amount of time without requiring an input excitation signal. For a negative feedback circuit configuration as shown in Fig. 5.1, the transfer function equation is as follows,

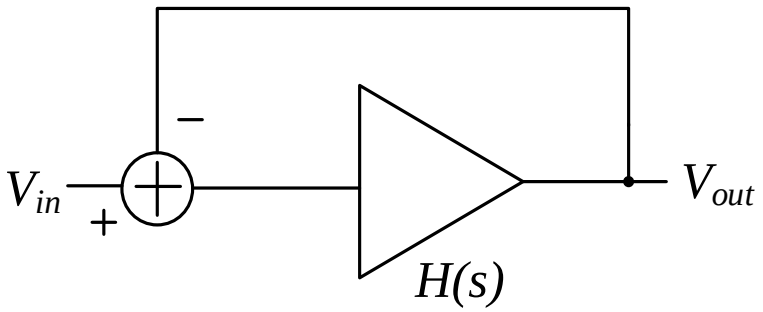

Figure 5.1: Block level schematic of a negative feedback system.

$$\frac{Vout}{Vin}(s) = \frac{H(s)}{1+H(s)} \tag{5.1}$$

where $s = j\omega_0$ and ω_0 is the oscillation frequency. To achieve an infinite loop-gain at the oscillation frequency, the two conditions, which are also known as Barkhausen's criteria are:

$$|H(jw_0)| \geq 1 \tag{5.2}$$

$$\angle H(jw_0) = 180^0 \tag{5.3}$$

These two conditions are necessary but not sufficient for oscillation to continue. In general, the loop-gain has to be two or three times the minimum start-up condition to make sure the oscillation sustains in the presence of process, voltage and temperature variations.

Fig. 5.2 shows the typical LC oscillator structure, where R_L is the loss associated with the parallel LC tank. At the oscillation frequency, $f_0 = \frac{1}{2\pi\sqrt{LC}}$ only the resistance R_L remains, which corresponds to the quality factor Q of the LC tank. When an active circuit with an equivalent impedance of - R_L is connected in parallel to the LC tank, the parallel impedance becomes infinite at the oscillation frequency. Once the Barkhausen's criteria are met as discussed in the previous section, the oscillation sustains indefinitely.

To achieve the negative resistance, an active gain cell with a transconductance, g_m is connected in the positive feedback configuration. To meet the Barkhausen's criteria, the loop gain,

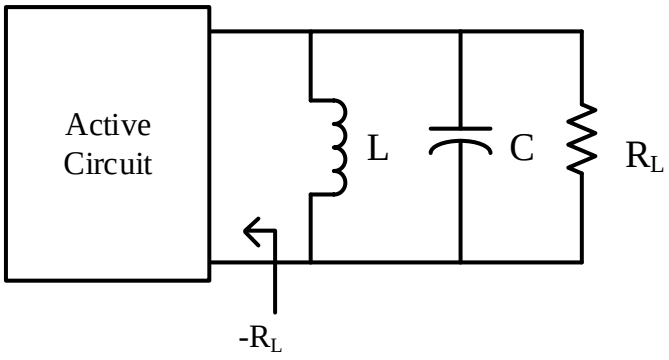

Figure 5.2: Circuit schematic of a negative feedback system.

$g_m R_L$ needs to be equal to one. In reality, $g_m > \frac{1}{R_L}$ which on the other hand sets the minimum bias current that is required to start-up the oscillator.

5.1.1 Theory of Operation

Most of the biomedical data transmission applications require the frequency of the oscillator to be tunable so that it can be calibrated if the oscillation frequency is shifted due to PVT variation. In addition, the tuning range of the oscillator allows multiple carrier frequencies for multiple sensor nodes, each having a certain bandwidth. The output frequency of the voltage controlled oscillator is linearly related to the DC control voltage, V_{CTRL}, as shown in the following equation,

$$f_{out} = f_0 + K_{VCO} V_{CTRL} \tag{5.4}$$

where f_0 is the center or the mid-frequency of the total linear oscillation frequency range and K_{VCO} is the conversion gain of the VCO, expressed in Hz/V. The tuning frequency range is the range of frequency for which the K_{VCO} is constant ensuring linear relationship as shown in equation 5.4.

Apart from the tunability, the VCO also needs to provide a high output amplitude for improving the noise performance. The output amplitude depends on the supply voltage, power dissipation, and the tuning range. Due to the noise contribution of the active circuits in the VCO,

the output spectrum shows the presence of noise, which is also known as jitter and phase noise. More details about the phase noise are presented in the following section.

5.1.2 Phase Noise Modeling of VCO

If the VCO is noiseless, the output voltage of the oscillator can be expressed as, $V_{out}(t) = A_0 \sin(2\pi f_0 t + \theta)$, where A_0 is the output voltage amplitude of the VCO and θ is the phase reference. This corresponds to an impulse signal at the frequency, f_0 in the frequency domain (Fig. 5.3 (a)). In reality, both the amplitude as well as the phase fluctuate over the time and the VCO voltage output spectrum is no longer an impulse signal. Assuming the amplitude fluctuation is negligible for well-designed VCOs, the phase noise becomes the dominant noise contributor. The output voltage of the VCO can be modeled as,

$$V_{out}(t) = A\sin[2\pi f_0 t + \theta(t)] \tag{5.5}$$

The output spectrum of the VCO demonstrates two side lobes due to phase noise, as shown in Fig. 5.3(b). To quantify the phase noise, the noise power over 1 Hz bandwidth at a frequency offset Δf from the oscillation frequency is divided by the VCO output signal power at the oscillation frequency. The unit of the phase noise is dBc/Hz. Thus, the single-sided power spectral density of phase noise can be expressed as,

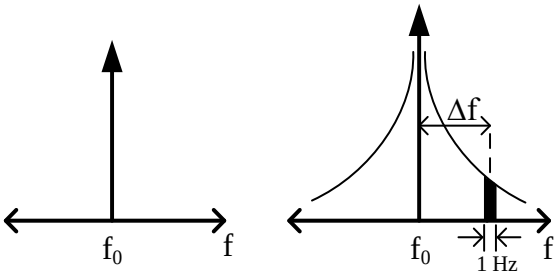

(a) (b)

Figure 5.3: Frequency domain output of the oscillator for (a) noiseless and (b) with phase noise.

$$L(\Delta f) = 10\log\left(\frac{Noise\ power\ in\ 1\ Hz\ band\ at\ the\ f_0+\Delta f\ frequency}{Power\ at\ f_0\ frequncy}\right) \quad (5.6)$$

Phase noise being a random noise is hard to analyze. For the simplicity of analysis, let us assume that the phase noise has a sinusoidal tone such that $\theta(t) = \theta_n sin(2\pi f_n t)$ where f_n is the offset from the oscillation frequency. Equation 5.5 can then be rewritten as,

$$V_{out}(t) = Asin[2\pi f_0 t + \theta_n sin(2\pi f_n t)]$$

$$= Asin(2\pi f_0 t)\cos[\theta_n sin(2\pi f_n t)] + Acos(2\pi f_0 t)sin[\theta_n sin(2\pi f_n t)] \quad (5.7)$$

Since θ_n is very small, we can rewrite the equation 5.7 as,

$$V_{out}(t) = Asin(2\pi f_0 t) + \frac{A}{2}\theta_n[sin\{2\pi(f_0 + f_n)t\} + sin\{2\pi(f_0 - f_n)t\}] \quad (5.8)$$

From the above equation, it is clear that due to the presence of phase noise there are two side lobes at an offset of f_n frequency from the carrier frequency. Equation (5.7) can also be expressed as [55],

$$L\{\Delta\omega\} = 10\log\left(\frac{P_{sideband}(\omega_0+\Delta\omega),at\ 1Hz\ offset}{P_{Carrier}}\right) \quad (5.9)$$

where $\omega_0 = 2\pi f_0$ and $\Delta\omega = 2\pi\Delta f$. Fig. 5.4 shows the phase noise responses of a free-running VCO and with the phase locked loop (PLL). The noise corner frequency, $1/\omega^3$ predominantly depends on the transistors flicker noise. The PLL essentially acts like a high-pass filter thus suppressing the low frequency phase noise. For the frequencies higher than the -3 dB cut-off frequency of the PLL, the phase noise is not suppressed anymore and thus the noise performance of the VCO needs to be improved to improve the overall noise performance.

The famous phase noise modeling equation for the $1/\omega^2$ region derived by Leeson is as follows [56],

$$L\{\Delta\omega\} = 4kTR_L F\left(\frac{\omega_0}{\Delta\omega}\right)^2\left(\frac{1}{2Q}\right)^2\frac{2}{{V_p}^2} \quad (5.10)$$

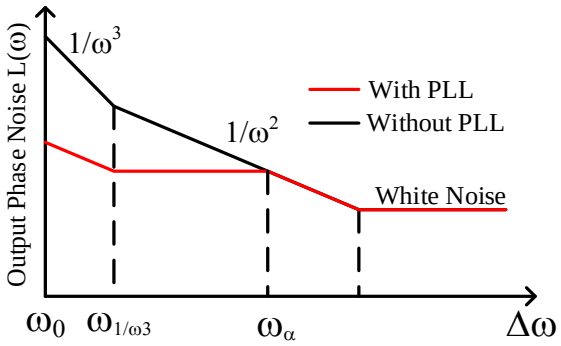

Figure 5.4: Phase noise of the VCO with and without the PLL.

where F is the effective noise figure based on empirical data, k is the Boltzmann's constant, Q is the effective quality factor, V_p is the output voltage swing and R_L is the equivalent loss resistance of the LC oscillator. From the equation, it is clear that the phase noise has an inverse relationship with the Q of the tank and the output voltage swing, thus increasing them improve the phase noise performance.

Taking into account the non-linearity of the active elements and their noise conversion, Hajimiri [55] proposed the *impulse sensitivity* function, which is a small-signal transfer function depicting the noise contribution of the all the odd harmonics of the oscillation frequency through the up-conversion to the fundamental frequency. The phase noise of the VCO in the $1/\omega^2$ region in terms of the ISF is expressed as,

$$L\{\Delta\omega\} = 10\log\left[\frac{\Gamma_{rms}^2}{q_{max}^2}\frac{\overline{i_n^2}/\Delta f}{4.\Delta\omega^2}\right] \tag{5.11}$$

Where q_{max} is the charge across the capacitor at the output node and Γ_{rms} is the RMS value of the ISF, $\Gamma(\omega t)$. ISF is an amplitude and phase independent function that depicts the amount of phase shift due to the current impulse injected at time t. $\overline{i_n^2}$ is the representation of all the noise current power sources that are present at the output node. The ISF is a periodic function with a

period of 2π and it peaks when the output voltage of the oscillator crosses zero and it is minimum when the output voltage peaks. From equation 5.11, it becomes clear why LC oscillator has comparatively lower phase noise than ring oscillator for the same amount of power consumption. For ring oscillator, both the PMOS and NMOS transistor are on during the transition, which increases $\overline{i_n^2}$ and thus the ISF high. On the other hand, LC oscillators discharge $2\pi/Q$ of the total energy in each cycle. Thus the q_{max} is smaller for LC oscillator than ring oscillator. Ring oscillators are also prone to PVT (process, voltage, and temperature) variations compared to LC oscillators. For LC oscillator, the oscillation frequency is determined by the resonance of the LC tank, which does not vary rapidly due to PVT variation. On the other hand, the oscillation frequency of the ring oscillator depends on the delay of the individual inverter cell and the delay varies rapidly due to PVT variations. Even though the ring oscillators occupy less die area and consume much less of a power compared to the LC oscillator, for the reliable wireless communication in the UWB frequency range LC oscillator is still most widely used. In the following section, different CMOS LC VCO architectures will be highlighted along with their design advantages and drawbacks.

5.1.3 LC VCO Topologies

As discussed earlier, to compensate for the loss associated with the LC tank, an active circuit element is necessary to provide the negative resistance in the loop. To sustain the oscillation, one transistor or two cross-coupled transistors can be used to emulate the positive resistance. Several topologies such as NMOS/PMOS cross-coupled LC oscillator and complementary cross-coupled LC oscillator with transistors connected in the common source configuration are shown in Fig. 5.5. The cross-coupled structure has a pair of NMOS or PMOS transistors along with the LC tank which latch up at the oscillation frequency. The oscillation frequency by varying the voltage (V_{CTRL}) across the varactor and the start-up condition requires

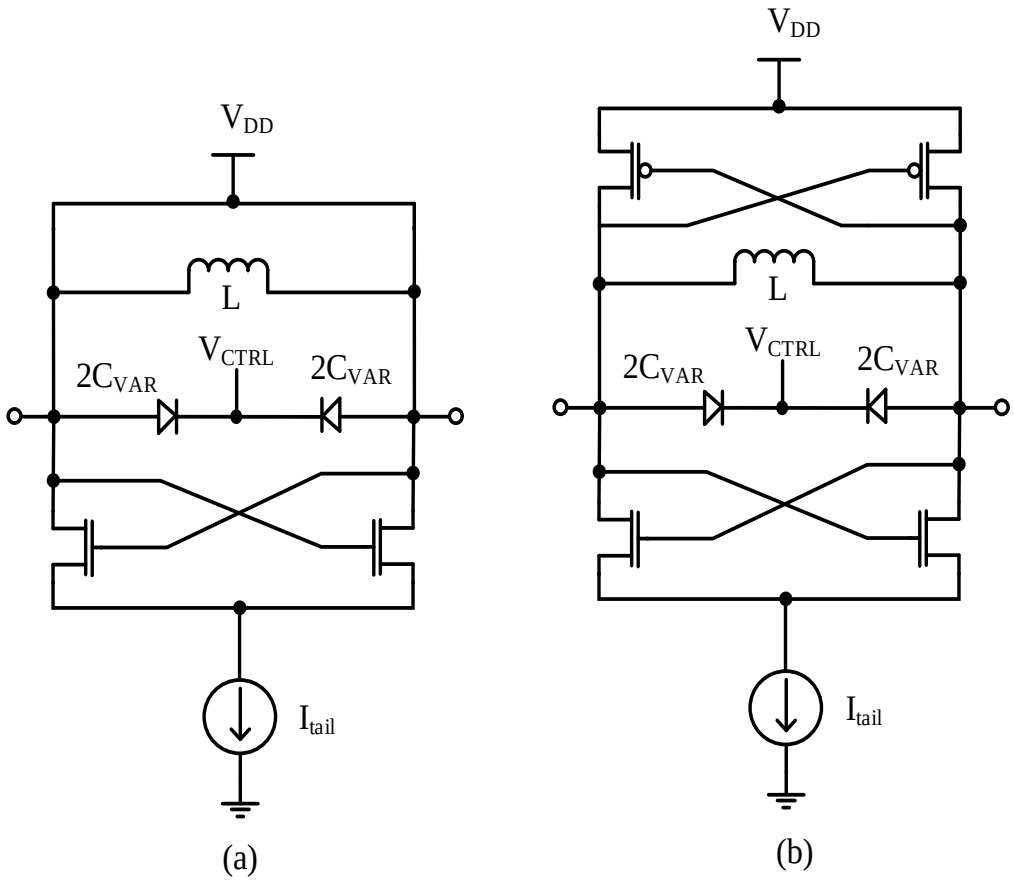

Figure 5.5: (a) NMOS cross-coupled LC oscillator and (b) Complimentary cross-coupled LC oscillator.

the transconductance (g_m) of each transistor to be greater than or equal to $2/R_L$. The complementary cross-coupled LC oscillator consists of a pair of cross-coupled inverters. The benefit of this structure is that it relaxes the start-up requirement ($g_{mn} + g_{mp} \geq 2/R_L$) and thus the bias current can be reduced.

In the complementary cross-coupled design, the overall transconductance, G_M is the summation of both g_{mn} and g_{mp} whereas, for the NMOS cross-coupled topology, $G_M = g_{mn}/2$. The peak-to-peak voltage amplitude of the NMOS cross-coupled LC oscillator is [57],

$$V_p = \frac{2}{\pi} R_L I_{tail} \tag{5.12}$$

where V_p is the voltage output swing of the oscillator, R_L is the equivalent loss resistance of the tank and I_{tail} is the bias current. For the same bias current, the output voltage swing for the complementary cross-coupled LC oscillator is [57],

$$V_p = \frac{4}{\pi} R_L I_{tail} \tag{5.12}$$

Thus the design of the complementary cross-coupled LC oscillator achieves better phase noise performance for the same power consumption compared to the NMOS or PMOS cross-coupled LC oscillator. The tank in this kind of oscillator provides considerable attenuation at frequencies other than the oscillation frequency thereby giving superior phase noise performance. This configuration facilitates high-speed and differential designs with large swing, reasonable tuning range, and low power consumption. The structure also allows low-supply operation. Depending on the inductor *Q*, the complementary cross-coupled oscillators can achieve sufficiently low phase noise for most applications.

5.1.4 Design Considerations

LC VCO topology is chosen for the IR-UWB transmitter designed using 130nm CMOS process due to the advantages of the complementary cross-coupled LC oscillator mentioned in the

previous section. The design objective is to achieve wide tuning range and low phase noise while consuming the minimum power. The LC tank includes an integrated inductor (L) of 2.323 nH and a varactor pair (C_{VAR}) to tune the oscillation frequency using V_{CTRL} voltage as shown in Fig. 5.6. Cross-coupled RF NMOS transistors, M_3 and M_4 along with cross-coupled RF PMOS transistors, M_5 and M_6 form a positive feedback loop. A bias current (I_{bias}) of 20 µA is mirrored and amplified by the M_0 - M_1 current mirror transistors. The tail current of the oscillator is 360 µA which makes the total power consumption of the VCO 432.7 µW with 1.2V supply voltage. The transistor, M_2 is designed to duty-cycle the VCO using the impulse signal, V_{VCO} generated from the impulse generator. A DC blocking dual-MIM capacitor, C_b of 2 pF is used to block the DC components of the VCO output voltage. A load capacitance of 0.25 pF is used in the simulated test-bench to represent the capacitance of the next stage, which is the driver circuit. Table 5.1 summarizes all the design parameters of all the transistors in the design.

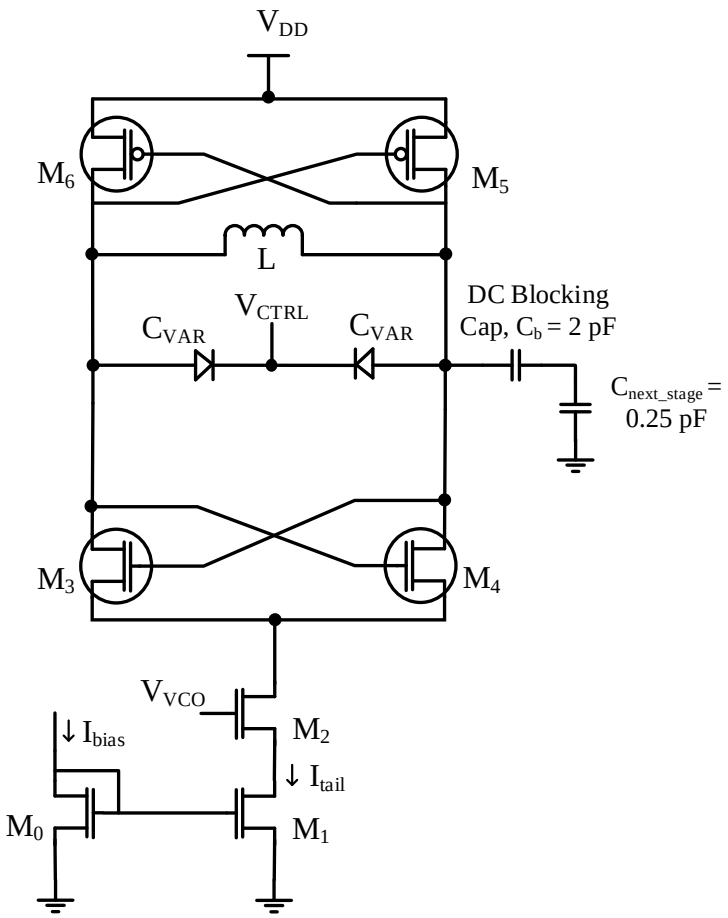

Figure 5.6: Complementary LC VCO designed in 130nm CMOS process.

Table 5.1: Summery of the Transistor Parameters of the VCO in Fig. 5.6

Components	W/L	i_d (mA)	g_m (S)	g_m / i_d (V^{-1})
M_0	4μm/120nm	0.02	426.7μ	21.34
M_1	80μm/120nm	0.36	7.91m	21.95
M_2	32μm/120nm	0.36	645.6 μ	1.79
M_3 - M_4	16μm/120nm	0.18	3.28m	18.19
M_5 - M_6	68μm/120nm	0.18	2.73m	15.16

The design challenge lies in the spiral inductor design with minimum loss resistance (thus achieving high *Q* for the tank). To achieve very high width of the inductor (8.8 μm) the spacing between the turns is chosen to be 5 μm. Secondly, the bias current for the VCO also needs to be optimized to achieve lower power consumption and faster start-up time. Lastly, the flicker noise up-conversion through the tail current transistor M_1 also needs to be minimized.

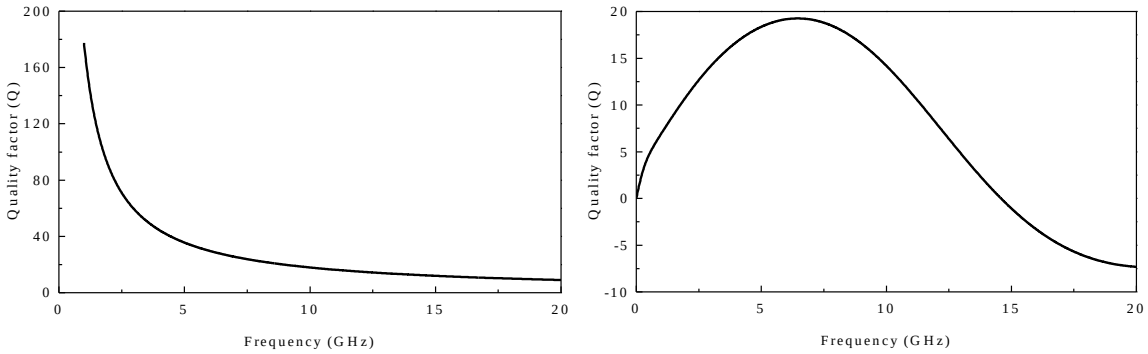

(a) (b)

Figure 5.7: Simulation of the Q of the (a) varactor and (b) inductor of the VCO.

5.1.5 Design Strategies

The varactor C_{VAR} is implemented using a high *Q* diode varactor. As the voltage (V_{CTRL}) across the varactor changes, it changes the capacitance of the varactor and thus the oscillation frequency is tuned. As the (C_{max} - C_{min}) range determines the tuning range of the VCO, the *n*-junction of the *pn* diode includes implants to enhance the tunability and increase the range. Fig 5.7 shows the simulated Q factor of the varactor and the spiral inductor in the VCO. The Q factor of the varactor at around 5.7GHz is about 40, and the inductor has a Q value of 17 at the same frequency. The width of the inductor, the spacing between each turn and the diameter have been optimized to achieve the high Q factor for the inductor. After 7 GHz, the parasitic capacitance associated with the inductor dominates and the Q starts to decrease. To reduce the flicker noise contribution of the VCO, the aspect ratio of the tail current transistor M_1 is chosen to be much

higher (80µm/120nm) compared to the other transistors. The aspect ratio of the PMOS cross-coupled pair (68µm/120nm) was chosen to be about 4 times higher than the PMOS cross-coupled pair (68µm/120nm) to make their transconductance and the transconductance efficiency almost the same. This helps achieve a symmetrical VCO output voltage and thus reduces the noise injection due to an unbalanced oscillation. The VCO is designed using 130 nm CMOS process. In the following section, simulation results of the proposed VCO are presented.

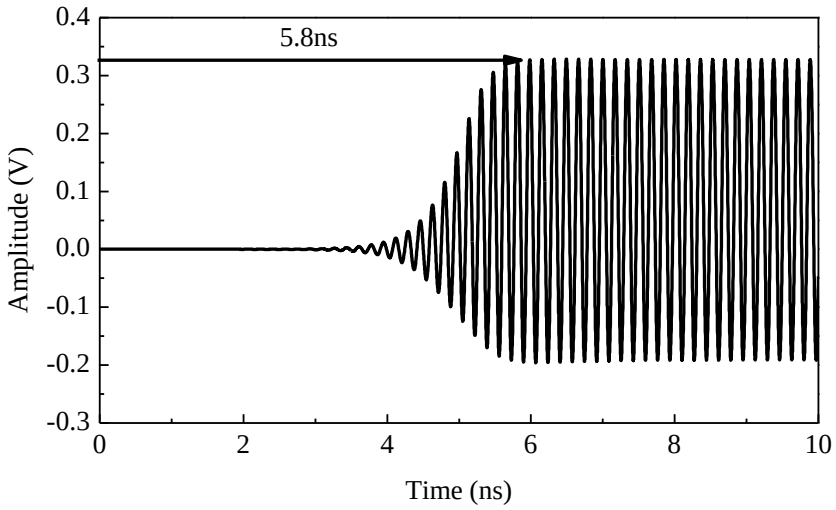

Figure 5.8: Transient simulation of the VCO.

5.1.6 Simulation Results of the VCO

To evaluate the performance of the VCO a test-bench is set up in Cadence with the V_{VCO} set as 1.2 V (on state of the VCO) and an I_{bias} current set as 20 µA. The tuning voltage V_{CTRL} is set as 800 mV and a two-shunted package parasitic capacitance of 250 fF and series inductance of 1 nH for bond wire were also included for all the off-chip supply voltages and currents. Fig. 5.8 shows the transient simulation of the output voltage of the VCO. From the figure, it can be observed that the start-up time is 5.8 ns and the output voltage amplitude is ~ 520 mV_{pp}. Fig. 5.9 shows the frequency spectrum of the output voltage of the oscillator. At the fundamental oscillation

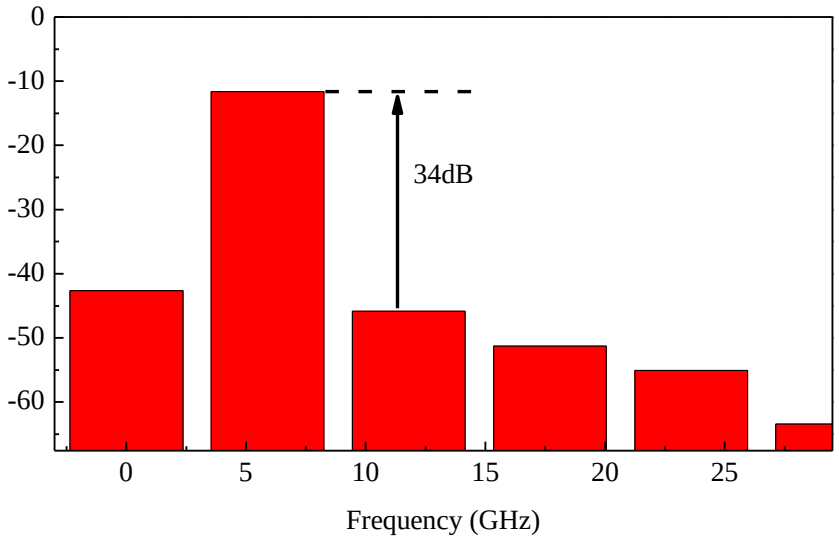

Figure 5.9: Output voltage spectrum of the VCO.

frequency of 5.8 GHz the output signal amplitude is -11.64 dBV and at the second harmonic (11.8 GHz) the output voltage amplitude is -45.85 dBV. The difference between the two amplitudes is about 34 dB, which makes the degradation of the performance due to second harmonics negligible. Fig. 5.10 shows the phase noise of the VCO for 5.8 GHz oscillation frequency. The phase noise at 1 MHz offset is -97.5 dBc/Hz for an output voltage amplitude of 520 mV_{pp}. The $1/f^2$ corner frequency is around 64 MHz. To find out the tuning range, the tuning voltage V_{CTRL} is varied from -0.1 V to 1.7 V (Fig. 5.11 (a)). The output frequency ranges from 5 GHz to 6.24 GHz over the voltage range, which makes the average conversion gain about 800 MHz/V. The total tuning range is thus 22.1% of the oscillation frequency of 5.6 GHz. Fig. 5.11 (b) shows how the varactor capacitance varies over the V_{CTRL} range. For the V_{CTRL} value of - 0.1 V, the capacitance is 288 fF and that reduces to 146.7 fF for the V_{CTRL} value of 1.7 V. The phase noise and the output voltage also vary over the V_{CTRL} range as shown in Fig. 5.12(a) and (b). From the two figures, it can be seen that the phase noise improves from - 80.15 dBc/Hz to -108.29 dBc/Hz as the V_{CTRL} is increased from -0.1 V to 0.2 V. The reason for the improvement becomes clear from the Fig. 5.12 (b). The

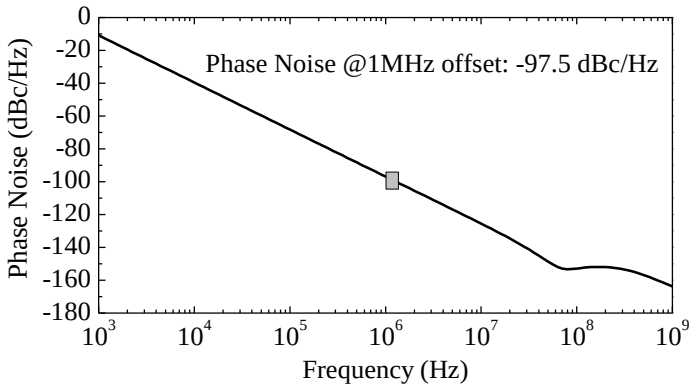

Figure 5.10: Simulated phase noise at 5.8 GHz.

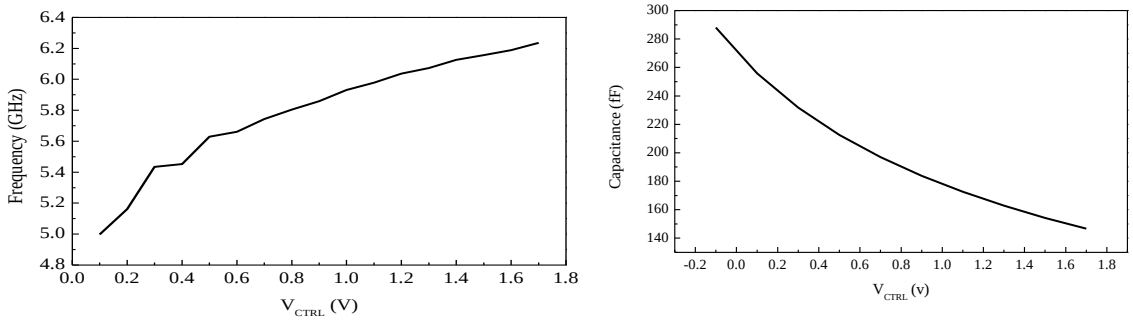

(a) (b)

Figure 5.11: (a) VCO output frequency versus V_{CTRL} and (b) varactor capacitance versus V_{CTRL}.

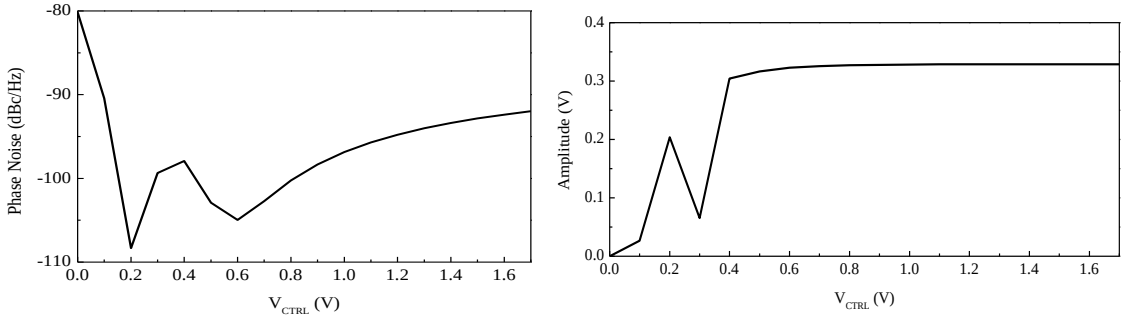

(a) (b)

Figure 5.12: (a) Phase noise versus V_{CTRL} and (b) VCO output voltage versus V_{CTRL}.

amplitude of the VCO output signal increases from 27 mV (54 mV_{pp}) to 328.6 mV (657 mV_{pp}) and thus the phase noise improves as evident from equation 5.10. To evaluate the performance metrics of the well-known equation of the figure-of-merit [58] is used,

$$FOM = 10\log_{10}\left[\left(\frac{f_0}{\Delta f}\right)^2 \frac{1}{L(\Delta f)P}\right] \tag{5.13}$$

where f_0 is the oscillation frequency, $L(\Delta f)$ is the phase noise at a Δf offset frequency, and P is the power consumption in mW. Using the obtained -97.5 dBc/Hz phase noise at 1 MHz offset frequency, 5.8 GHz oscillation frequency, 0.43 mW power consumption the FOM can be calculated to be 89.04. While this is not one of the best FOMs compared to the CW radio due to its high power consumption, as the VCO is duty-cycled, the average power consumption reduces significantly.

5.2 Buffer/Driver Circuit

The antenna driver or the buffer circuit is another power-hungry block in the transmitter. The key challenges in the design of the driver circuit for the IR-UWB transmitter include optimization of the design parameters to achieve energy efficiency and FCC spectral mask compliance. The traditional analog power amplifiers can achieve spectral compliance by operating far below the 1-dB compression point but the efficiency would be very low [20]. Digital driver circuitry, on the other hand, suffer from PVT mismatches and their leakage current also increases exponentially as the CMOS process scales down.

5.2.1 Classes of Driver Circuits

There have been studies going on for many years on different classes of the amplifier circuit for improving energy efficiency. They can be broadly categorized as linear-mode and switched-mode amplifier. In the following section, a brief introduction to these two categories is presented.

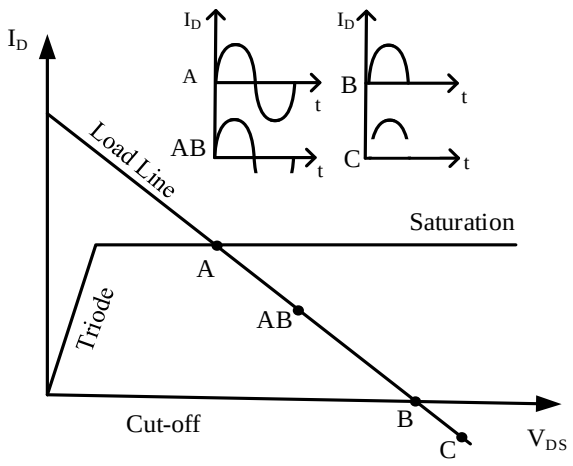

Figure 5.13: Operating points for different classes of power amplifiers.

Linear mode amplifiers are categorized based on their drain current waveform of the transistor for an applied input. Fig. 5.13 shows the different operating points of the RF transistor in the driver for different classes. In Class A operation, the transistor operates most linearly. The Q point is selected in the middle of the I_D-V_{DS} load-line and the transistor does not enter the cut-off or triode region. Fig. 5.13 also shows the quiescent current waveform, which shows that for Class A the current flows throughout the cycle. Thus, theoretically, the maximum achievable efficiency for Class A amplifiers is 50% [57]. For Class B amplifiers, the transistor is ON for half of the RF period thus reducing the average DC power consumption. As the drain efficiency is defined by the ratio of the RF output power and the DC power consumption, lowering the power consumption improves the efficiency. Theoretically, Class B amplifiers can achieve a maximum efficiency of 78.5%. Since the transistor is not ON for the entire RF cycle like Class A amplifier, its linearity is also reduced. The gain is also lower compared to the Class A amplifier. The bias point of Class AB amplifier is in between Class A and B amplifiers. The linearity of the Class AB amplifier is better than the Class B amplifier but the efficiency is worse than Class B amplifier.

One of the common examples of Class B amplifier is the push-pull configuration where the PMOS and NMOS transistors are turned on and off alternatively for half of the period.

The performance of the driver or the filter circuitry determines the pulse amplitude and the shape of the output signal of the transmitter. In Class C amplifier the transistor is ON for less than half cycle, thus consuming much lesser power compared to Class A and AB amplifiers. The linearity of Class C amplifier is worse than the Class A and AB amplifiers but the efficiency is much higher. Theoretically, Class C amplifiers can achieve 90% efficiency.

In literature, different Class A and AB amplifiers have been designed to amplify the impulse signal generated by the delay cell based generator and the VCO [59], [37] circuit. While these amplifiers readily achieve pulse shaping readily, the energy efficiency is poor. The amplifier architecture also does not allow duty-cycling feature which means that the buffer or the driver circuit continuously dissipates power due to the static bias current.

In switched-mode amplifier, the transistor is implemented as switches and current-controlling device. When the transistor is ON, it has zero voltage across it, while the transistor has zero current flowing through it when it is OFF. Thus, the static power consumption (product of voltage and current) is always zero. Classes D, E and F amplifiers are the prime examples of the switched-mode power amplifier. Cascaded inverters with progressively increasing W/L ratio are also implemented as digital buffers to drive 50 Ω load antenna [60]. Even though this technique might seem like an attractive option as a buffer circuit, the dynamic power consumption increases proportionally as the frequency increases in the UWB range. Additionally, it is difficult to implement pulse shaping in cascaded inverter based driver circuit.

5.2.2 Design Considerations

Before discussing the design considerations of the driver circuit designed to be operating in the UWB frequency range, it is important to highlight the design parameters that can be traded-off for optimizing the performance of the driver. The first parameter, which is the drain efficiency, η_D is defined as,

$$\eta_D = \frac{P_{RF,out}}{P_{dc}} \tag{5.14}$$

where $P_{RF,out}$ is the RF output power and P_{dc} is the static power consumption. For any power amplifier circuitry, the design objective is to increase the efficiency. Another important efficiency parameter, which is known as power-added efficiency, *PAE* is defined as,

$$PAE = \frac{P_{RF,out} - P_{RF,in}}{P_{dc}} \tag{5.15}$$

where $P_{RF,in}$ is the RF input power. The linearity of the amplifier is quantified by the term called third-order intercept point, IP3. Any amplifier, being a non-linear device generates harmonics. In the presence of two-tone input signals which are closely spaced in frequency, the amplifier generates intermodulation products. The third-order intermodulation products lie close to the fundamental components of the RF output in the frequency domain, which makes it harder to filter them out using a band-pass filter. It is difficult to measure the IP3 point of an amplifier directly as it enters into the compression point before that. The 1-dB compression point is defined as the input power for which the output power is 1-dB lower than the linear model of the amplifier (Fig. 5.14). The IP3 point can be derived graphically by expanding the fundamental and the 3rd order intermodulation distortion products. The input power for which the fundamental tone power and the 3rd order intermodulation product converges is called the input-referred IP3 as shown in Fig. 5.14. As a rule of thumb, the input-referred IP3 power, P_{IIP3} is usually 10 dB higher than the 1-dB compression point.

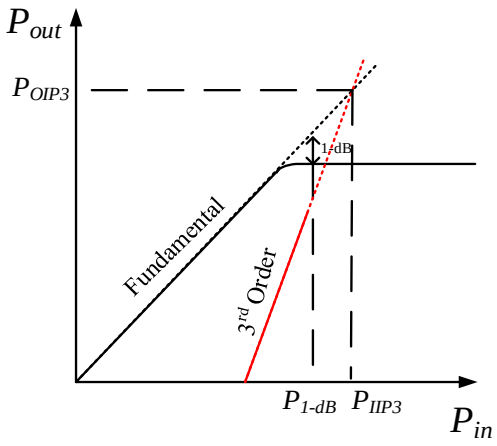

Figure 5.14: 1-dB compression point and IIP3 of an amplifier.

A Class C based driver circuit is designed using 130 nm CMOS process to drive the 50 Ω load (Fig. 5.15). The driver consists of the RF NMOS transistor, M_8 and M_7 NMOS transistor for implementing triangle pulse shaping. The bias voltage for the M_8 transistor, V_{bias} of 450mV is chosen to be lower than the threshold voltage to ensure the transistor on for less than 50% of the RF cycle. A 1 kΩ resistor, R is used to drive the gate of the M_8 transistor. The output voltage of the VCO, V_{IN} first passes through the DC blocking capacitor, C_b of 2pF to remove any DC signal present in the VCO output. Triangle pulse signal (V_{PA}) generated by the charge pump circuit discussed in the previous chapter shapes the output waveform. Table 5.2 lists the transistor parameters in the design. Both M_7 and M_8 transistors have high W/L ratios to reduce their flicker noise contribution. The choke inductor, L_2 is 2.323 nH, which is the same spiral inductor that has been used in the VCO circuit block. For all the simulation test benches of the driver circuit, two shunted capacitors of 250 fF for the bond pad and packaging parasitic and a series inductor of 1 nH for the bond wire were included with all the input and output ports. With 1.2 V supply voltage, the bias current is 1.464 mA, which makes the static power consumption of the driver circuit ~1.76 mW.

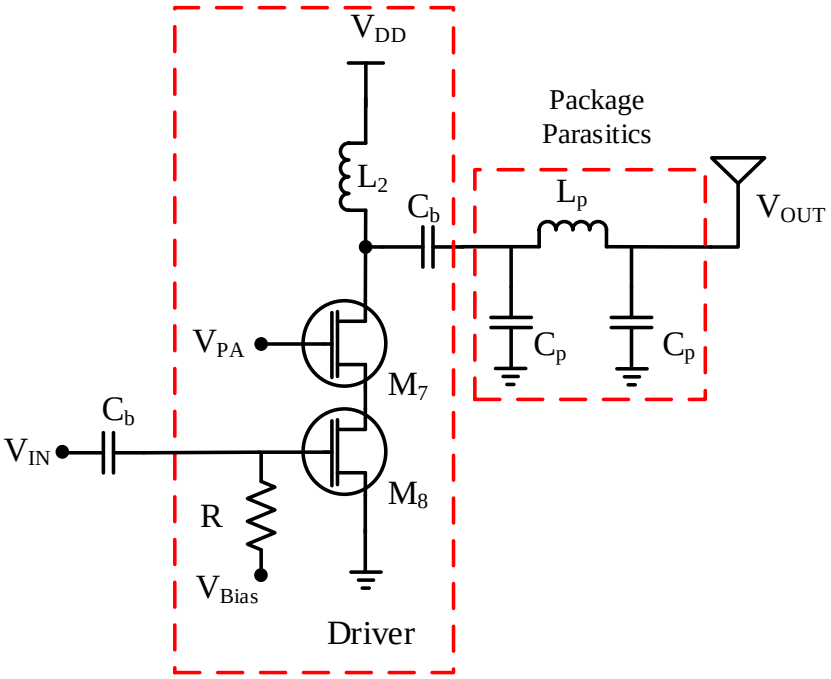

Figure 5.15: Class-C driver circuit with package parasitics.

Table 5.2: Summary of the Transistor Parameters of the Driver Circuit in Fig. 5.6

Components	W/L	i_d (mA)	g_m (S)	g_m / i_d (V^{-1})
M_7	120µm/120nm	1.464	26.04m	17.79
M_8	120µm/120nm	1.464	26.55m	18.14

5.2.3 Simulation Results of the Driver Circuit

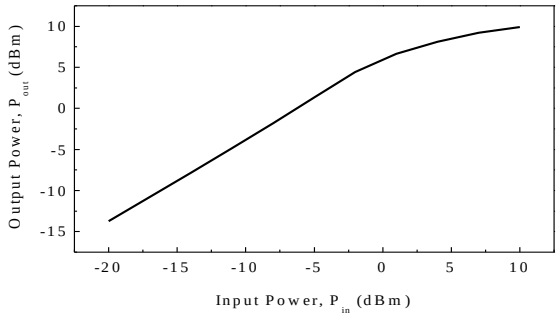

Figure 5.16: Output power versus input power of the driver.

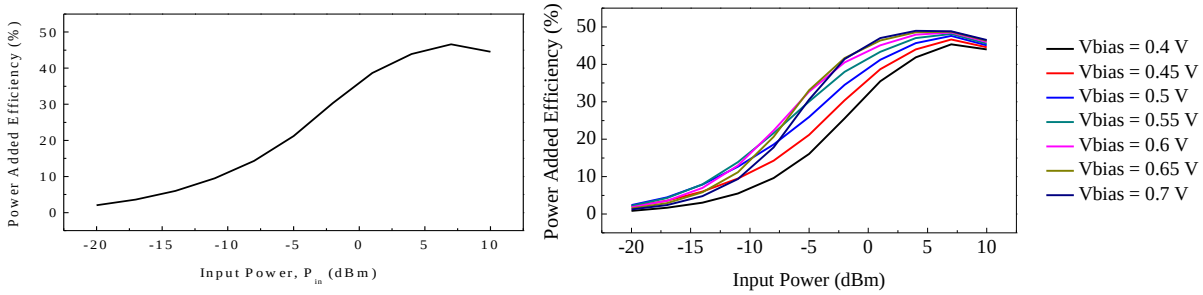

(a) (b)

Figure 5.17: (a) PAE simulation for V_{bias} = 450 mV and (b) PAE for different V_{bias} voltages.

Fig. 5.16 shows the simulation results of the output power, P_{out} of the driver for different values of the input power. The RF input power with a frequency of 4 GHz is swept from -20 dBm to 10 dBm and the amplifier shows a constant gain of 4dB up to the 1-dB compression point. The PAE is plotted in Fig. 5.17(a). For the V_{bias} of 450 mV, the maximum PAE is 46.6% at an input power of 7dBm. The bias voltage is swept from 0.4V to 0.7V with 50 mV interval and the PAE plots are shown in Fig. 5.17(b). The maximum PAE is 48.94% for an input power of 4 dBm and V_{bias} of 0.7V.

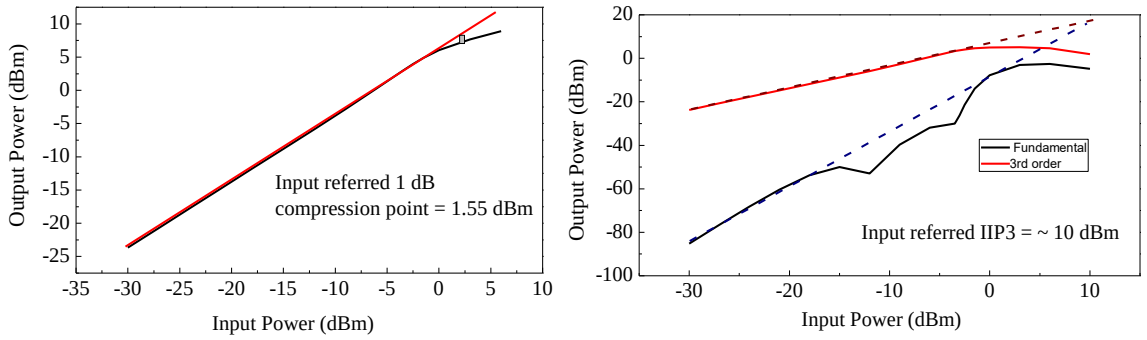

(a) (b)

Figure 5.18: Simulation result of (a) -1-dB compression point and (b) IIP3.

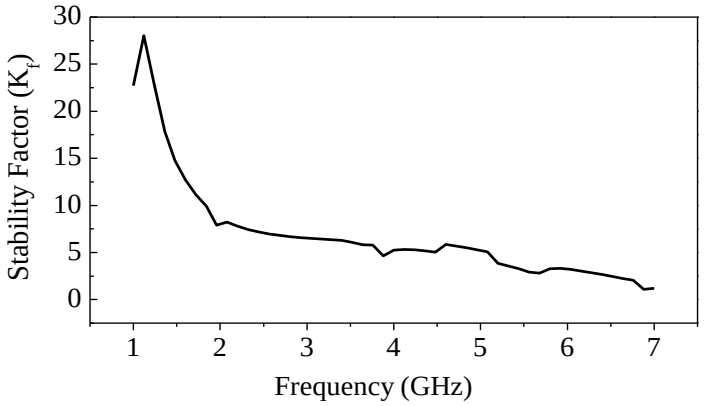

Figure 5.19: Stability factor (K_f) simulation for P_{in} = 0 dBm.

Fig. 5.18 shows the linearity performance of the driver/amplifier. Fig. 5.18 (a) highlights the $P_{1\text{-}dB,input}$ to be 1.55 dBm. The simulated fundamental and the 3rd order intermodulation products in Fig. 5.18 (b) are extrapolated to achieve the input-referred IIP3 power, $P_{IIP3,input}$ of 10 dBm.

Fig. 5.19 shows the simulation result of the stability factor (K_f) for an input power of 0 dBm, where the K_f factor is greater than 1 for the 3 to 7 GHz frequency range. This ensures the stability of the amplifier in the frequency range of interest. To match the output impedance of the driver with the 50 Ω load antenna, a *pi* matching network as shown in Fig. 5.20 is designed. The matching network is implemented on the PCB board to have the flexibility of tuning the network

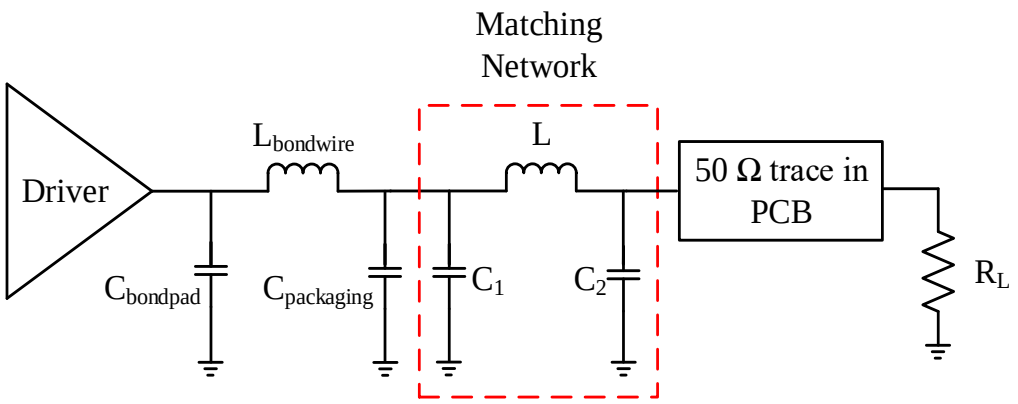

Figure 5.20: Driver output matching network along with package parasitic.

as needed. The calculated values of *L*, C_1 and C_2 are 2.5 nH, 100 fF and 2 pF, respectively. The simulated scattering parameters of the driver circuit are shown in Fig. 5.21. No matching network is designed for the input matching as the output of the VCO is a voltage signal. The value of *S11* is -0.4 dB at 5 GHz, which is worse than the *S22* value. (-18.7 dB at 5 GHz). The gain (*S21*) is 13 dB at 5 GHz and the isolation parameter (*S12*) is -28.2 dB at 5 GHz.

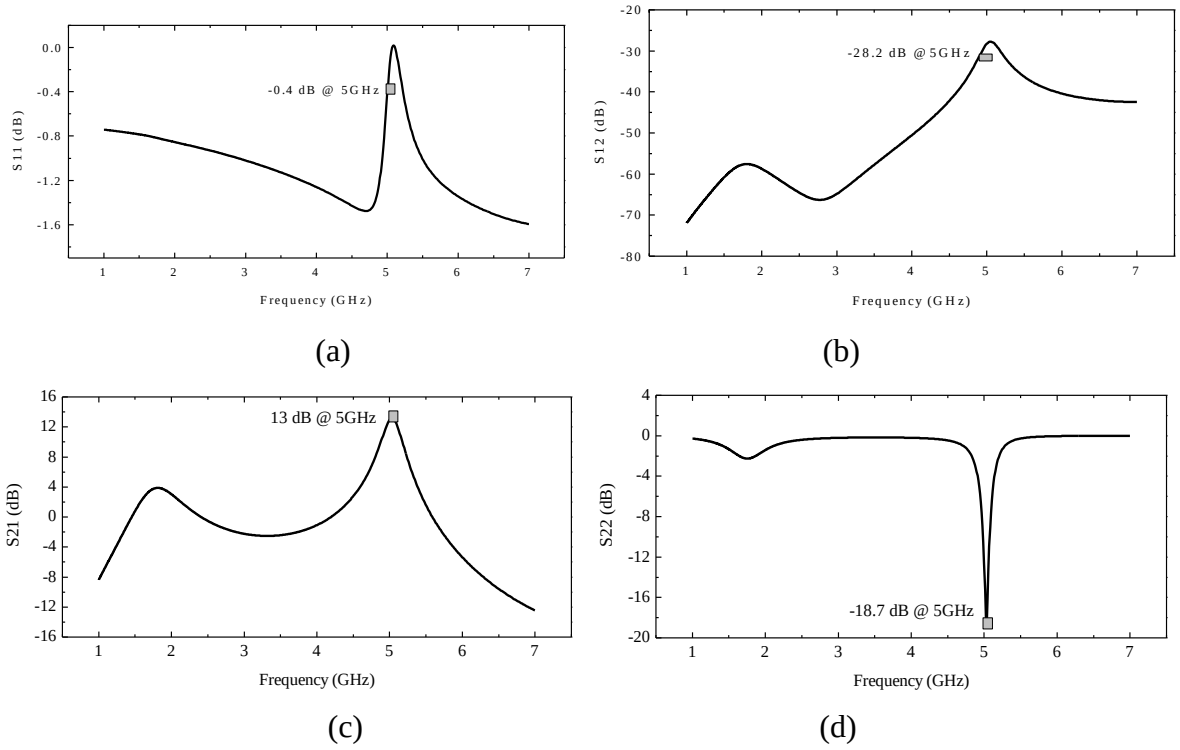

Figure 5.21: Simulated (a) S11, (b) S12, (c) S21 and (d) S22 parameters of the driver circuit.

5.3 Simulation Results of the VCO Along with the Driver

The combined performance of the VCO and the driver circuit is presented in this section. The schematic is shown in Fig. 5.22. The gate bias voltage of the driver (V_{bias}) is 450 mV and the V_{PA} is 1.2 V. The VCO is also enabled by having a bias voltage of 1.2 V as V_{VCO}. The combined phase noise is -100.64 dBc/Hz at 1 MHz offset as shown in Fig. 5.23 (a). The amplitude modulated (AM) noise and the phase modulated (PM) noise are shown in Fig. 5.23 (b). The PM noise is -97.6 dBc/Hz which is 3 dB higher than the phase noise shown in Fig. 5.23 (a) as it considers the double spectrum of the design. The output frequency of the VCO and the driver changes from 5.26 GHz to 6.1 GHz as the tuning voltage, V_{CTRL} changes from 0.2 V to 1.8 V (Fig. 5.24(a)). The frequency change (Δf) vs. the tuning voltage, V_{CTRL} is plotted in Fig. 5.24(b), which shows that as the voltage increases, Δf decreases.

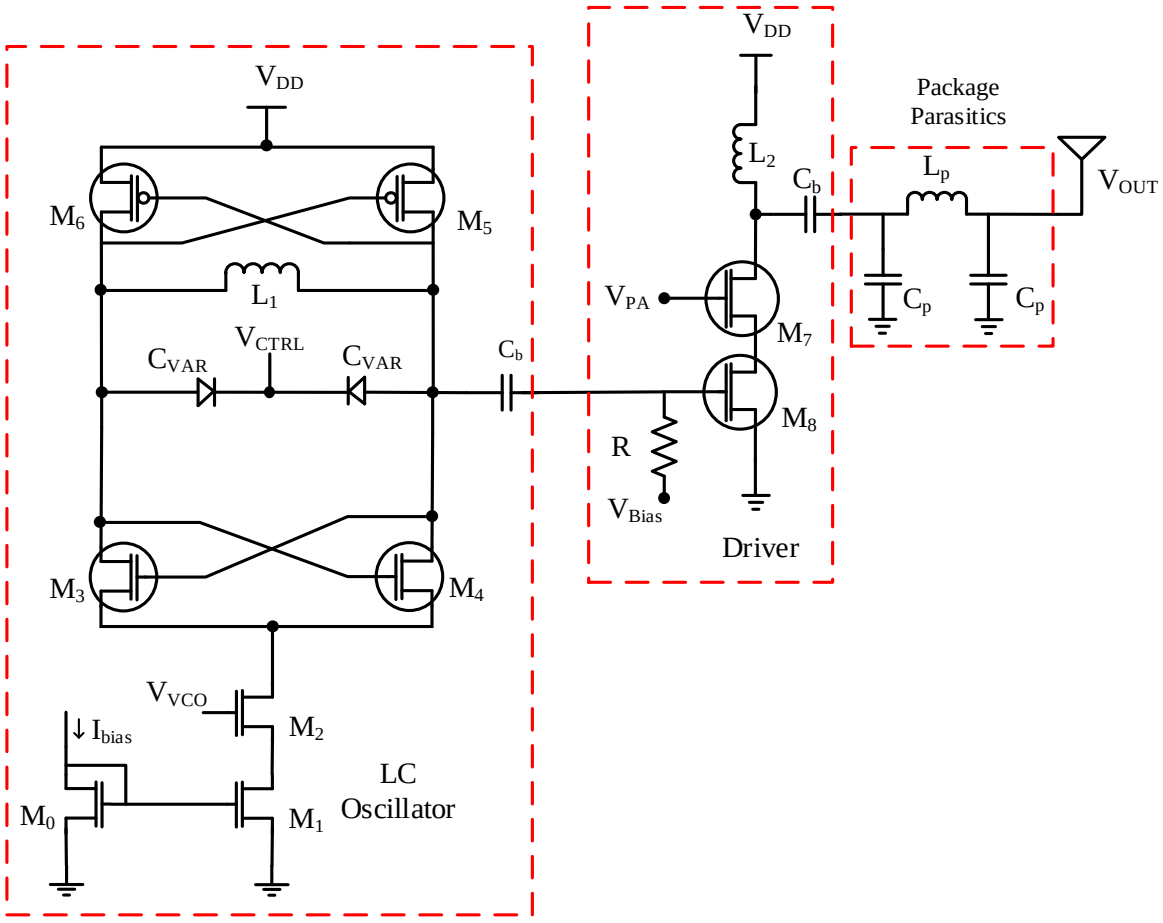

Figure 5.22: VCO and the driver circuit.

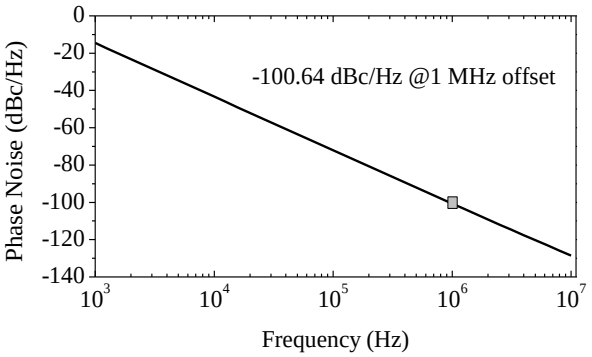

(a)

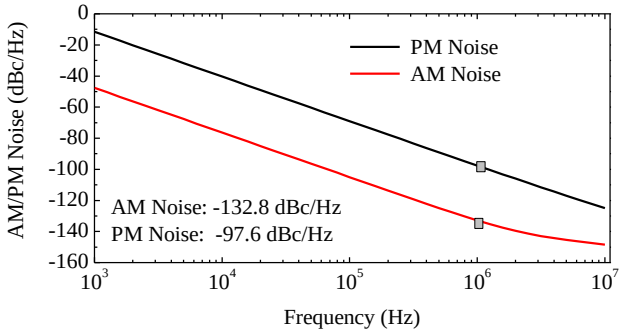

(b)

Figure 5.23: (a) Phase noise and (b) AM and PM noise performance of the VCO and the driver.

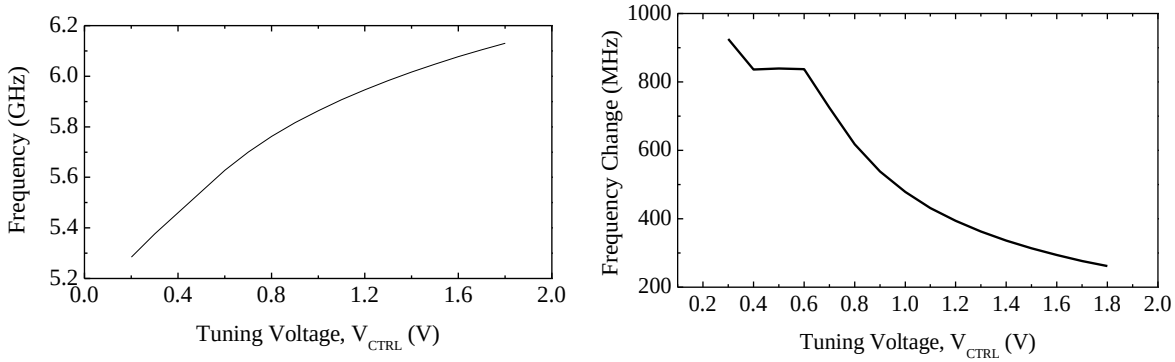

Figure 5.24: (a) VCO and driver output frequency versus V_{CTRL} and (b) Δf versus. V_{CTRL}.

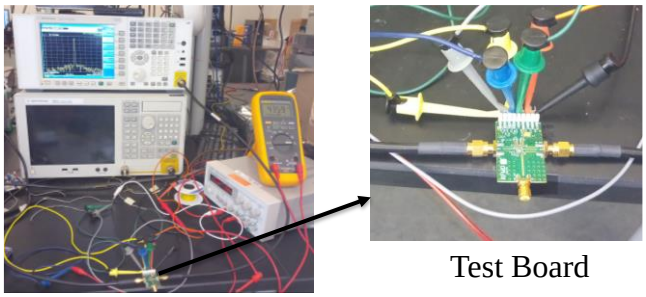

Figure 5.25: Driver/ power amplifier circuit test bench.

5.4 Measurement Results of the Driver/Power Amplifier

The driver circuit is tested separately to evaluate its performance. The bare die is attached to the board using non-conductive epoxy and the test pads in the CMOS die are wire-bonded to the board using gold wire-bonds. The test-bench and the pre-fabricated test board with the die are shown in Fig. 5.25. An RF signal generator (MG3693C by Anritsu) is used to generate 4 GHz sinusoidal signal as an input of the power amplifier. The input power is incremented from -20 dBm to 4 dBm with a 2 dB interval. The measured (shown in red color) and the simulated (shown in black color) output power of the driver amplifier with respect to the input power are shown in Fig. 5.26. From the measured data it can be seen that the measured 1-dB compression point input power is -1.5 dBm whereas the simulated 1 dB compression point input power is 1.55 dBm. The loss in the traces in the board is one of the reasons why the output power is lower than expected. Additionally, as there was no provision for designing an off-chip matching network in the pre-fabricated test-board. The poor matching at the input and output of the power amplifier is another reason for the drop of the gain of the driver amplifier. The simulated and the measured gain plots are shown in Fig. 5.27. From the measurement results, the mid-band gain is 3.6 dB, which is 2.4 dB lower than the simulated mid-band gain. The simulated and the measured PAE plots are shown in Fig. 5.28 for different input powers. The maximum measured PAE is 10.55% at the input power of -2 dBm

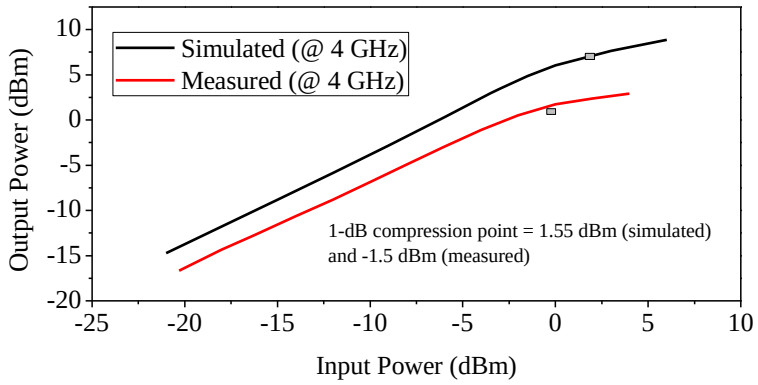

Figure 5.26: Simulated and measured output power of the driver for different input powers

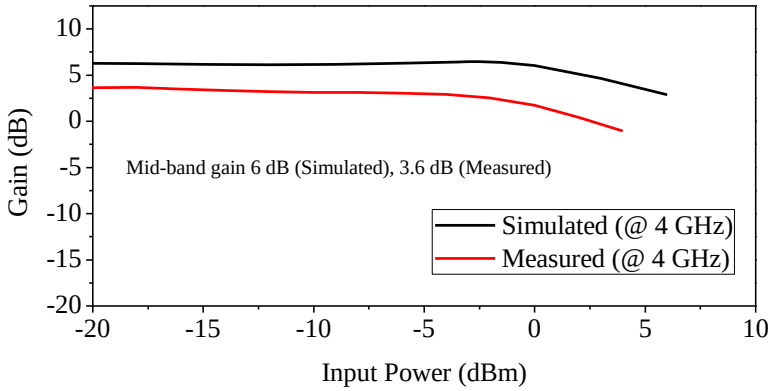

Figure 5.27: Simulated and measured gain of the driver for different input powers

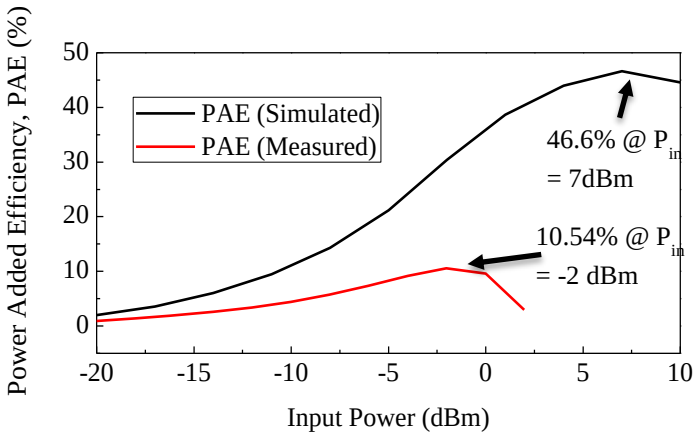

Figure 5.28: Simulated and measured PAE of the driver for different input powers

whereas the simulated maximum PAE is 46.6% at an input power of 7 dBm. Because of the losses associated with the trace and the board discussed earlier, the PAE is also lower than the simulated result. The measured reflection coefficients at the output and the input ports are shown in Fig. 5.29 (a) and Fig. 5.29 (b) respectively. The S11 at 4 GHz is measured to be -5 dB, which is due to not having a matching network at the input side of the driver amplifier. The measured S22 is -8 dB at 4 GHz, which could be further improved by designing an off-chip matching network using off-the-shelf components. For the IR-UWB transmitter application, since the maximum output power is limited by the FCC mask regulation, even with low gain and low PAE the driver amplifier is able to efficiently transmit data in the UWB frequency range.

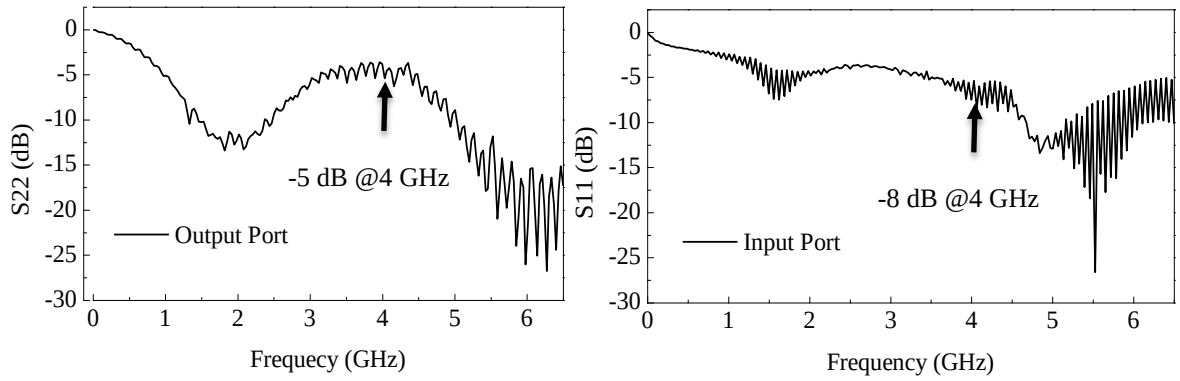

(a) (b)

Figure 5.29: Measured reflection coefficient at the (a) output and (b) input port

5.5 Summary and Conclusion

In this chapter, the VCO operation principals as well a brief introduction to phase noise are presented. Different LC VCO topologies are also discussed along with the pros and cons of various topologies. This is followed by a presentation of a complimentary cross-coupled LC oscillator designed in 130 nm CMOS process. With a supply voltage of 1.2 V, the VCO consumes 432.7 µW

power while achieving a 22.1% tuning range with a mid-oscillation frequency of 5.6 GHz. At 1 MHz offset, the phase noise is -97.5 dBc/Hz.

In the later sections of the chapter, the driver circuitry that follows the VCO is presented. A Class C driver amplifier operating in the 5 to 6 GHz frequency range with a PAE of 46.6% and a DC power consumption of 1.76 mW. With a gain of 13 dB, the input-referred 1-dB compression point power is 1.55 dBm and input IIP3 power is 10 dBm. The combination of the VCO and buffer also demonstrates similar phase noise and tuning range, thus making it suitable to be used in the IR-UWB transmitter system.

Chapter 6 Low-Power IR-UWB Transmitter Design

In this chapter, various IR-UWB transmitters designed using 180nm and 130nm CMOS processes are presented. Their design specifications are also highlighted and a comparison with the state-of-the-art research works are also presented at the end.

Non-coherent energy detection receiver with OOK modulation scheme is suitable for a low-data rate wireless link because it facilitates simplicity in design, thus ensuring low cost and low power consumption. Before the design specification of the proposed system is investigated, it is important to look into the bit error rate (BER) performance of the OOK modulation. BER is the error in the number of bits per unit interval time. It can also be computed by dividing the number of error bit by the total number of bits transmitted for a given period. In Fig. 6.1, BER for transmitting 10^7 number of bits using OOK modulation scheme is presented. The BER is computed with a sampling rate of 10 kSps with each sample containing 10 bit resulting in the data rate of 100 kbps. Considering the duration of the pulse to be 2 ns, the duty-cycling ratio (2 ns/0.01 ms) becomes 0.02%.

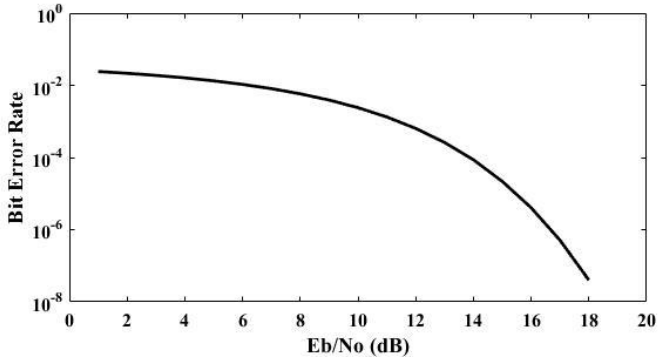

Figure 6.1: BER simulation using MATLAB for OOK modulation.

Table 6.1: IR-UWB Transmitter Design Specifications

Parameter	Unit	Equation	Value
Data Rate (R)	kbps	-	100
Distance (D)	m	-	1
Bandwidth (BW)	MHz	-	528
Pulse Duration	ns	$\frac{1}{BW}$	2
Average Tx Power (P_{avg})	dBm	$-41.3\frac{dBm}{MHz}+10log_{10}(BW)$	-14.3
Duty-Cycling Gain (G_{duty})	dB	$10log_{10}\left(\frac{BW}{R}\right)$	37
Tx Peak Power	dBm	$P_{avg.}+G_{duty}$	22.7
Center Frequency (f_c)	GHz	-	3.1–5

For a low-data rate application, the target bit error rate can be set as 10^{-4}, which makes the required energy per bit to noise density ratio (E_b/N_o) to be 14. Some of the transmitter design specifications can be acquired based on the power emission constraints, which are presented in Table 6.1.

6.1 Design of the IR-UWB Transmitter in 180nm CMOS Process

6.1.1 System Overview

Based on the analysis and design constraints that were discussed in the previous sections, the proposed transmitter is designed and the design architecture is presented in Fig. 6.2. It includes an impulse generator designed with digital gates, a tunable cross-coupled LC oscillator for up-converting the baseband impulse signal to UWB frequency range and a buffer to drive the 50Ω antenna. The transmitter is designed using a standard 180 nm CMOS process. It follows on-off keying (OOK) modulation scheme where "1" bit is represented by a short pulse and "0" bit is represented by the absence of a pulse signal. The core building block of the impulse generator is a

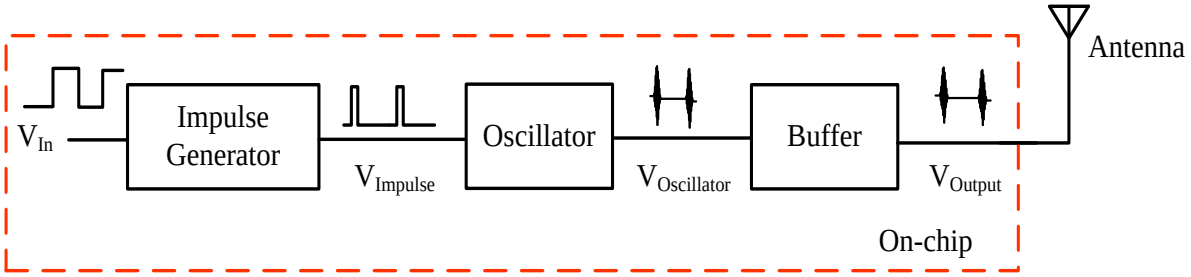

Figure 6.2: System level block diagram of the proposed IR-UWB transmitter in 180 nm HV CMOS process.

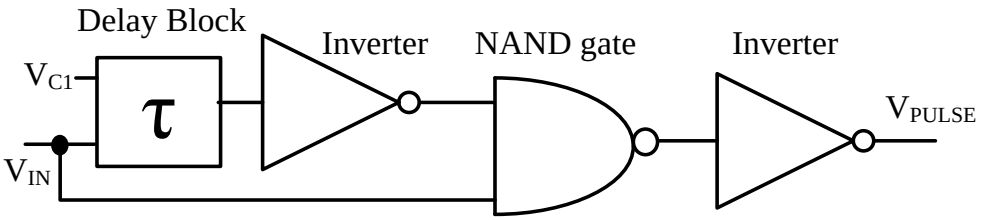

Figure 6.3: Schematic of the impulse generator block.

tunable delay block, an inverter, a NAND gate and another inverter to generate the desired impulse signal (Fig. 6.3). The input signal, V_{IN} is the digitized breathing signal acquired by the charge amplifier. The frequency of this input signal depends on the sampling rate and the resolution of the ADC (analog-to-digital converter). The delay in the delay block is controlled by changing the biasing voltage, V_{C1} of the current-starved inverters as shown in Fig. 6.4. By changing the pulse width of the impulse signal, the spectrum can be modified to make it FCC regulation compliant.

For the oscillator block, LC tank oscillator scheme is chosen over ring oscillator for its lower process variability and lower phase noise characteristics. The LC voltage controlled oscillator (VCO) core consists of the cross-coupled NMOS pair ($M_{2–3}$) and LC tank with inductors ($L_{1–2}$) and two variable capacitors (C_{var}) implemented using MOS capacitor based varactors as shown in Fig. 6.5. The center frequency of oscillation can be tuned by changing the control voltage V_{CTRL}.

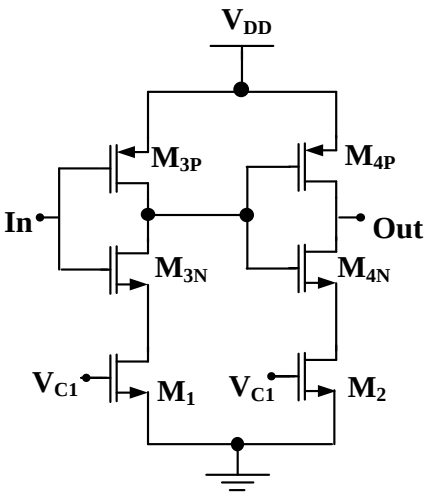

Figure 6.4: Delay block circuitry.

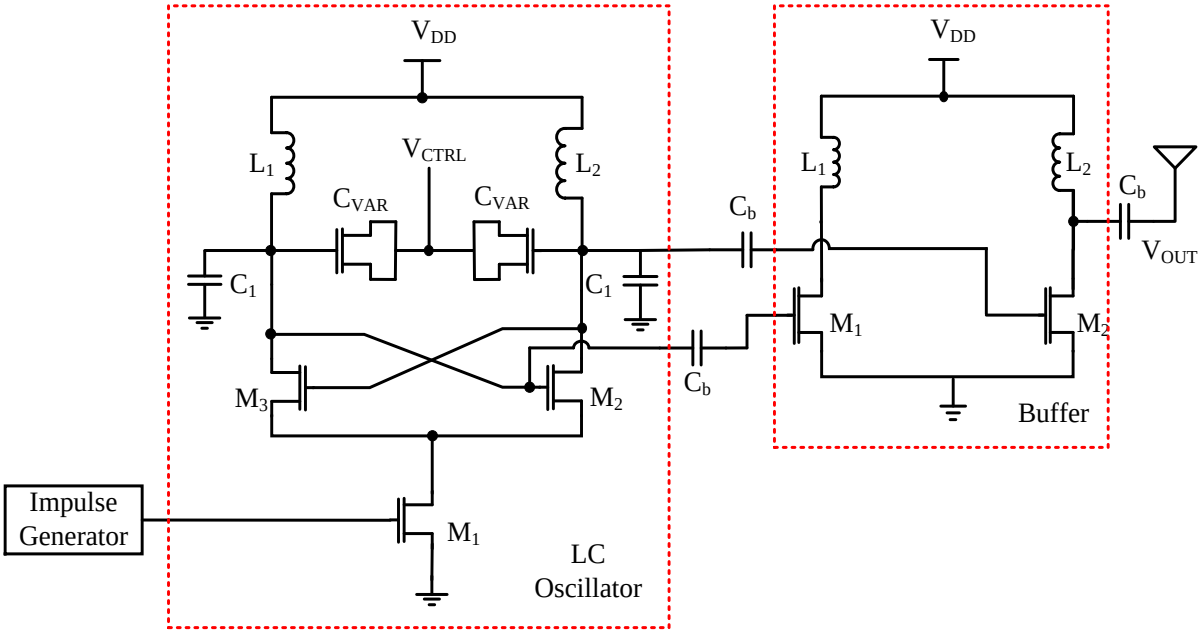

Figure 6.5: Crossed-couple LC oscillator and buffer with the impulse generator.

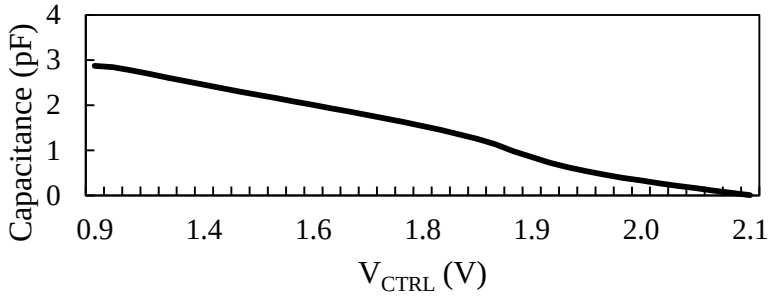

Figure 6.6: The capacitance of the varactor as a function of the V_{CTRL} voltage.

The W/L ratio of the MOS capacitor is $\frac{80\mu}{0.18\mu}$. A simulation result of the variance of capacitance over the change of control voltage is shown in Fig. 6.6. Additional capacitances of ~100fF (C_1) were added at the output node of the oscillator. The values of the inductor, L_1, and the varactor capacitor, C_{var} can be calculated based on the following equation,

$$f_{osc} = \frac{1}{2\pi\sqrt{L(C_1+C_{var})}} \tag{6.1}$$

where f_{osc} is the oscillation frequency of the LC tank. The impulse signal coming from the impulse generator block controls the ON/OFF operation of the VCO through the tail transistor M_1. The sizing of the transistor, M_1 is chosen in such a way so that it ensures sufficiently fast turn on time for the pulse generation. High energy efficiency is obtained by turning on the LC VCO only during the pulse generation and turning it off for the rest of the time. The start-up time of the oscillator, which determines the lowest bound of the pulse duration is minimized by minimizing the gate capacitance of the tail current transistor using multiple fingers. It can also be decreased by decreasing the tank Q value or the open-loop gain of the oscillator, but the power consumption is expected to increase in both cases. A differential buffer is cascaded after the LC VCO to isolate the oscillator from the load impedance variation. The source-follower topology is chosen for the buffer stage with proper sizing of the inductors and bias to drive the 50 Ω antenna as shown in Fig. 6.5.

6.1.2 Simulation Results

The simulation result of the output waveform of the impulse generator is shown in Fig. 6.7. The simulated pulse width is 1.2 ns and the peak-to-peak output voltage amplitude is 1.3 V. The simulations are performed with an input signal data rate of 100 kbps or a pulse repetition frequency of 100 kHz. The baseband signal from impulse generator is then fed into the gate of the tail current transistor of the LC oscillator. The DC content of the output of the oscillator is blocked by the DC blocking capacitor, C_b (1pF). The time domain output waveform of the transmitter signal is shown in Fig. 6.8. The amplitude of the signal is 285 mV_{pp} while the duration of the pulse is ~3 ns. The PSD (power spectral density) of the transmitter is shown in Fig. 6.9. From the figure, it can be seen that the oscillation frequency is at 2.7 GHz and the peak emission power is -41.83 dBm/MHz. The -10 dB bandwidth is about 753 MHz. Clearly, this violates the FCC mask regulation and does not fall into the 3.1 – 5 GHz frequency spectrum. This happens because of the fact that C_b in series with C_{gs} forms an equivalent capacitance $C_{eq} = (C_b \,||\, C_{gs})$ which is added to the total capacitance at the oscillator output node, thus reducing the oscillation frequency. Without the C_b capacitor, the output of the transmitter is shown in Fig. 6.10. The pulse width of the waveform is about 3 ns with an additional 1.8 ns of pulse tail, which was not evident in the Fig. 6.8. The corresponding PSD is shown in Fig. 6.11. From the figure, it can be seen that the peak emission power at 3.6 GHz is -42.28 dBm/MHz and the -10 dB bandwidth is about 572 MHz and the overall power spectrum follows the FCC mask regulation. The first prototype designed in the 180 nm process included the C_b capacitance. As a result, the measured frequency spectrum is also shifted. In the future work, the inductor value of the LC tank will be reduced accordingly to achieve the oscillation frequency of 3.5 GHz.

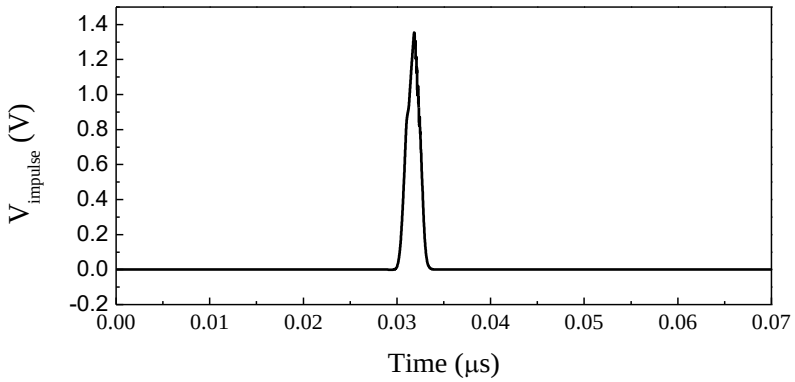

Figure 6.7: Simulation result of the impulse waveform from the impulse generator.

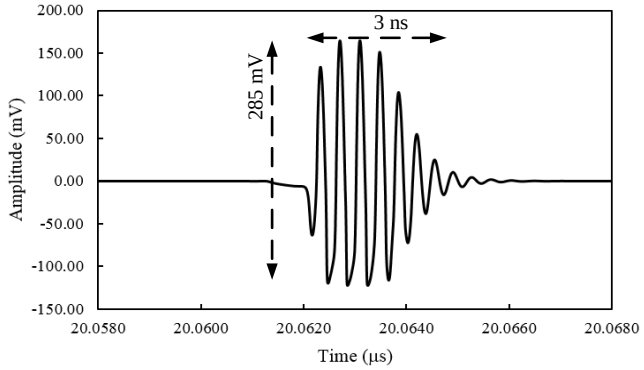

Figure 6.8: The output waveform of the transmitter with C_b capacitor between the LC oscillator and the buffer.

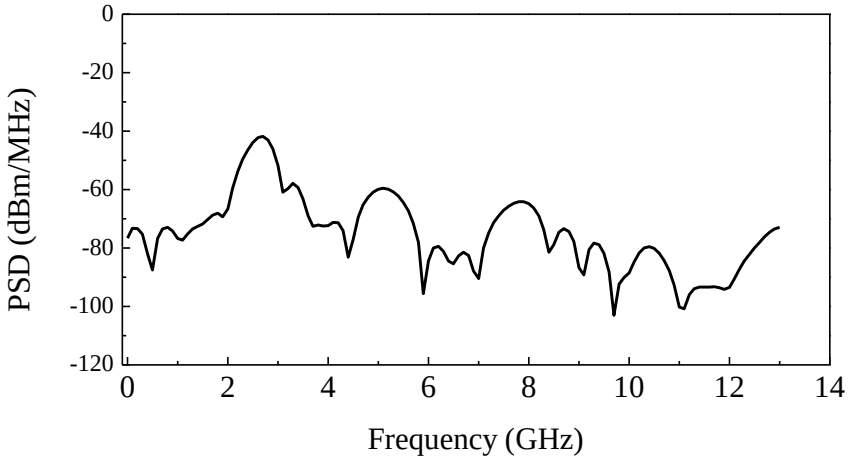

Figure 6.9: Power spectral density (PSD) of the waveform in Fig. 6.8.

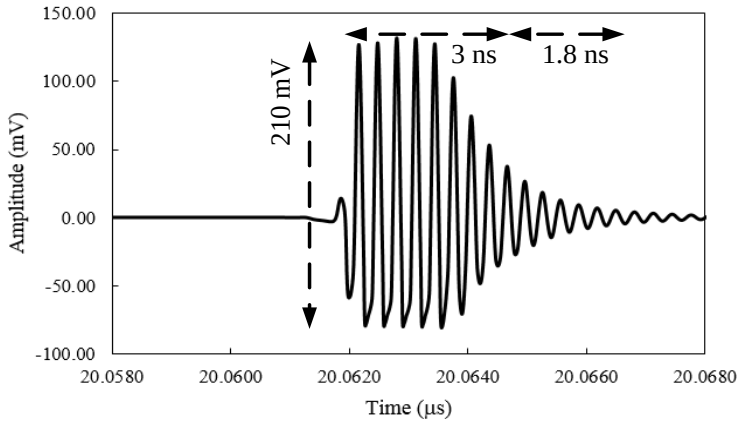

Figure 6.10: The output waveform of the transmitter without the C_b capacitor between the LC oscillator and the buffer.

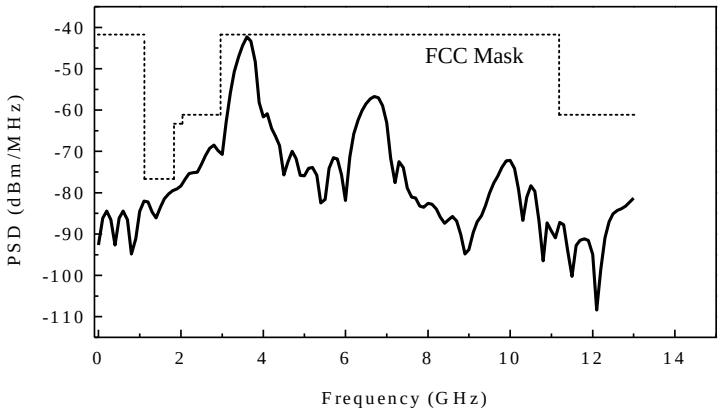

Figure 6.11: Power spectral density (PSD) of the waveform in Fig. 6.10.

6.1.3 Measurement Results

For acquiring the measurement data, the CMOS die was attached to the test PCB (62 mil width FR4 board) by using non-conductive epoxy material and then wire bonded to the board directly. The test setup of the PCB board with the wire bonded die is shown in Fig. 6.12. At first, the time domain signal output of the impulse generator block was measured using DSO-X 3104A oscilloscope by Agilent Technologies. The baseband impulse signal for a data rate of 100kbps is shown in Fig. 6.13. The measured signal is about 670 mV_{pp} in amplitude and the pulse width is 1.24 ns. An additional buffer was used after the impulse generator to drive the pad capacitance. The corresponding PSD of the impulse signal measured using N9010A EXA Signal Analyzer by Agilent Technologies is shown in Fig. 6.14. From the figure, it can be seen that the -10dB bandwidth of the signal to be around 806 MHz.

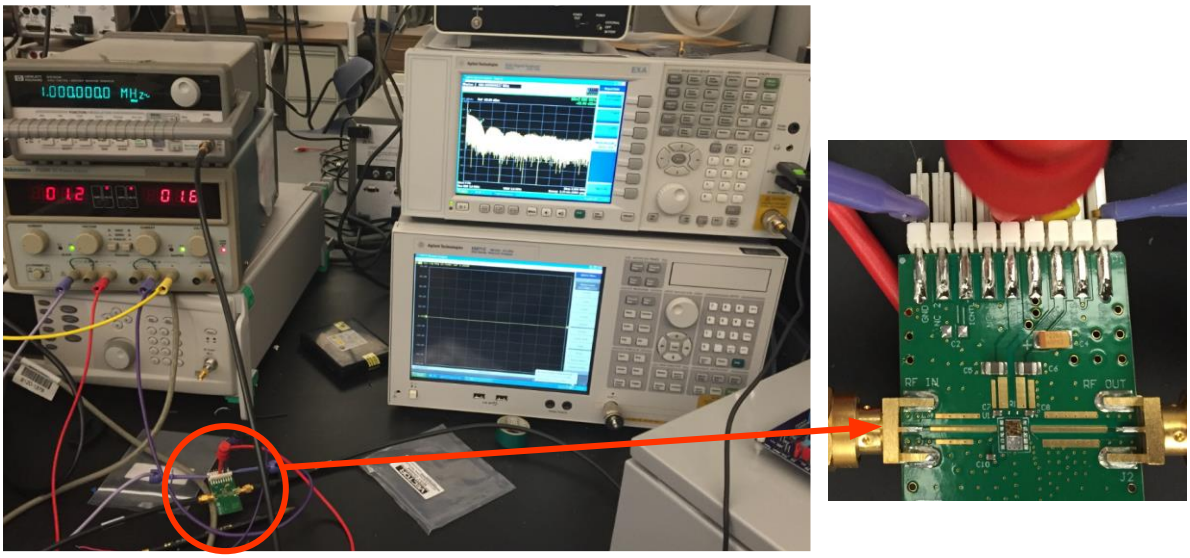

Figure 6.12: Test setup with the test PCB.

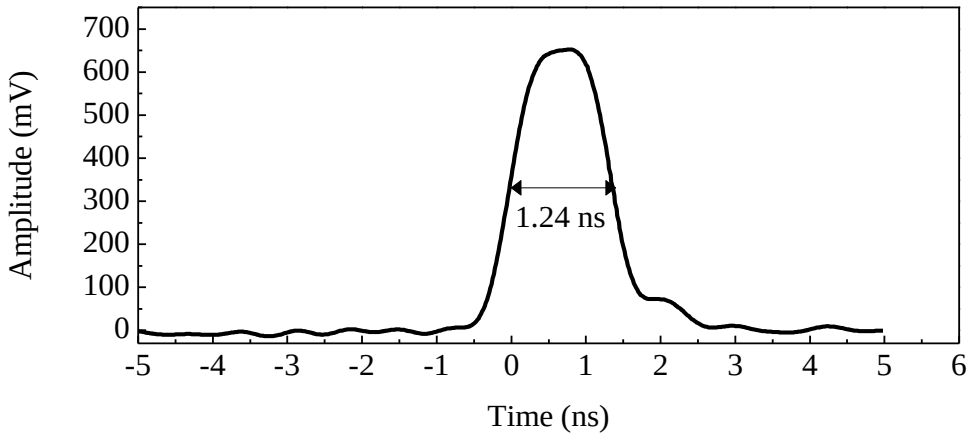

Figure 6.13: The measurement result of the impulse waveform.

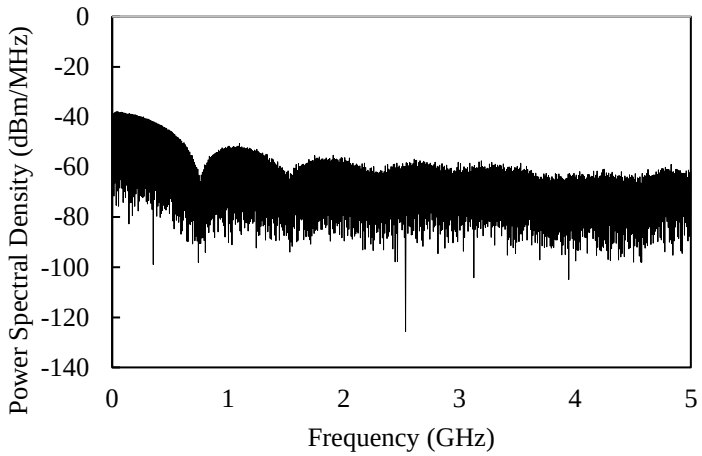

Figure 6.14: PSD of the baseband impulse signal from the impulse generator.

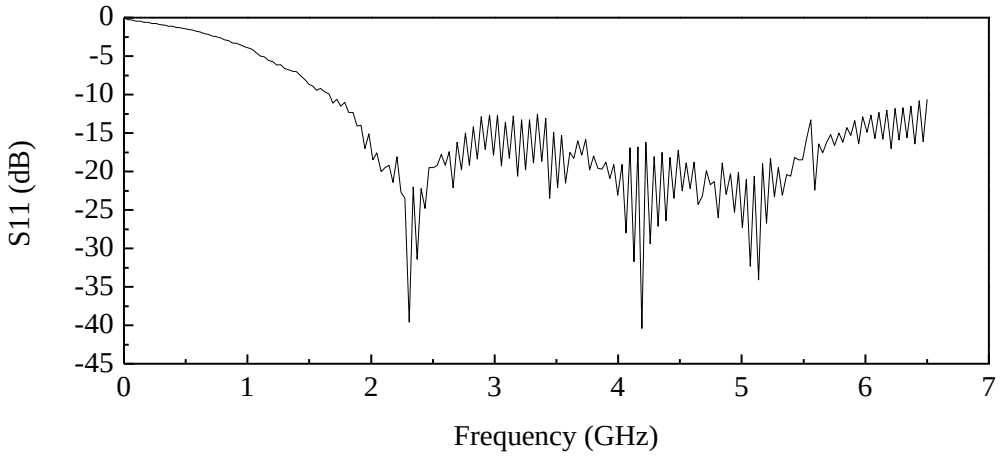

Figure 6.15: Measured reflection coefficient at the RF output node.

The time domain waveform output of the transmitter and the data stream of "10101…" is shown in Fig. 6.15. The amplitude of the output impulse signal is 65 mV_{pp}, which is lower than the simulated value (285 mV_{pp}). This could be due to the attenuation resulting from the cable and the bond wire inductances. The oscilloscope that has been used to measure the time domain waveforms has a sampling rate of 5 Gsamples/s. As a result, the waveform looked discontinuous because the frequency of the transmitter output is more than 2.4 GHz and the sampling rate of the oscilloscope barely meets the Nyquist criteria. A plot of *S11*of the RF output node measured using E5071C Network Analyzer by Agilent Technologies is shown in Fig. 6.16. The figure shows a maximum reflection coefficient of -40 dB around 2.4 GHz. Unfortunately, the oscillator and the buffer blocks were not connected to test pads in this tape-out to test them individually. The PSD of the transmitter output waveform is shown in Fig. 6.17. Even though the frequency is shifted to 2.47 GHz, the peak emission power (-41.92 dBm/MHz) and the -10 dB bandwidth (720 MHz) follows the FCC regulation. The core area of the design is 0.315 mm^2 which is highlighted in the chip microphotograph (Fig. 6.18).

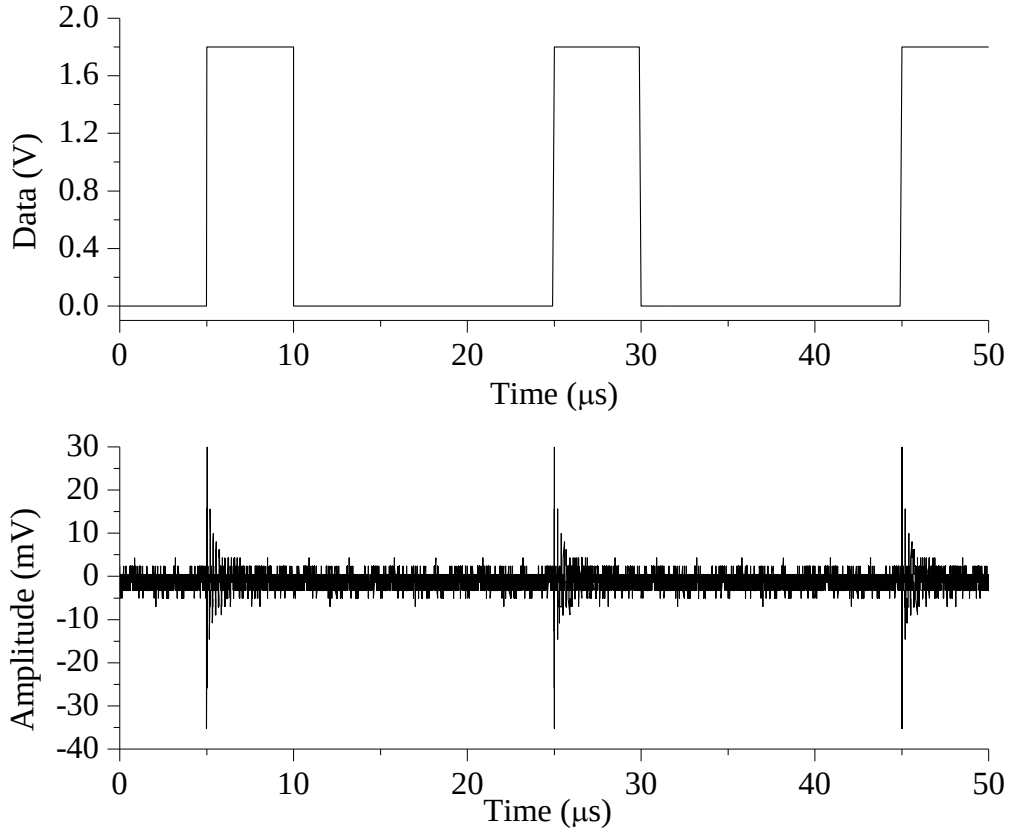

Figure 6.16: Input data (top) and the corresponding transmitter output (bottom).

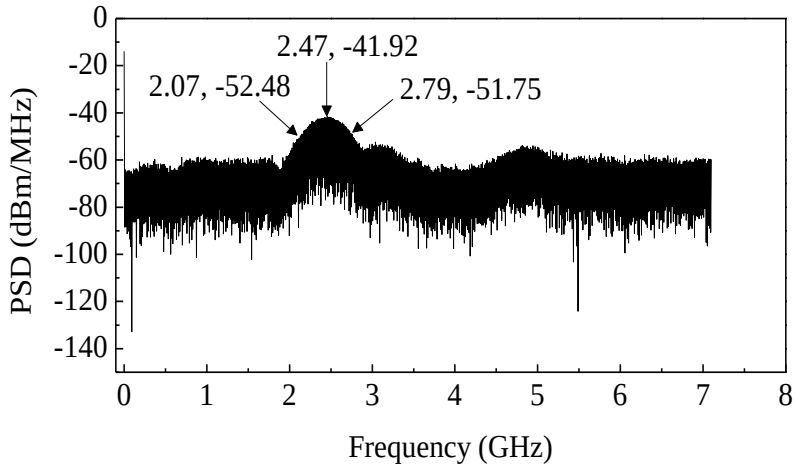

Figure 6.17: PSD of the impulse signal from the transmitter.

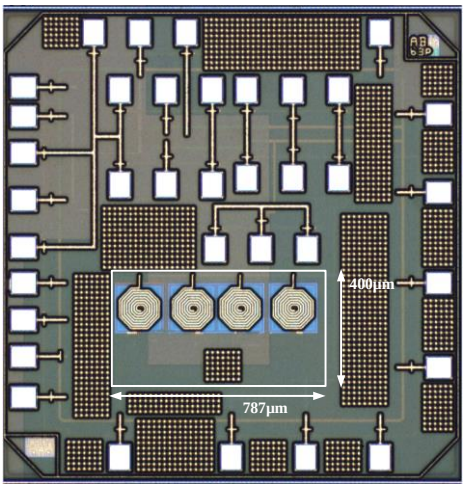

Figure 6.18: Chip microphotograph of IR-UWB transmitter designed in 180 nm CMOS process.

Table 6.2 compares the simulation and the measurement results of the transmitter with the other state of the art IR-UWB designs published in the literature. The leakage power (off-state) of the proposed design is only 437.4 nW which is much lower than the work presented in [21] and [61]. The transmitter in [61] utilizes a ring oscillator, therefore, the power consumption of the system is much lower compared to the proposed work. The energy per pulse for the proposed design at 100 kbps data rate is better than [21] but not better than [61]. With the aim to improve the energy efficiency, the transmitter is designed in the 130 nm CMOS process with 1.2 V supply voltage.

Table 6.2: Performance Comparison with the Other IR-UWB Transmitters

Performance	[21]	[61]	This work (simulation)	This work (measurement)
Technology	180nm CMOS	90nm CMOS	180nm CMOS	180nm CMOS
Supply Voltage	1.5 V	1 V	1.8 V	1.8 V
Frequency Spectrum	3.1-5 GHz	3.1-5 GHz	3.1-5 GHz	3.1-5 GHz
Oscillator Architecture	LC	Ring	LC	LC
Output Voltage Swing	0.16 V	0.5 V	0.21 V	70 mV_{pp}
Pulse Width	3.5 ns	1-2 ns	3 ns	1.4 ns
Tx Leakage Power	3.9 mW	2.9 µW	437.4 nW	437.4 nW
Tx Total Power	3.9 mW	5.7 µW	36.29 µW	36.29 µW
Active Die Area (mm^2)	0.308 mm^2	0.1 mm^2	0.315 mm^2	0.315 mm^2
Modulation	OOK	OOK	OOK	OOK
-10 dB Bandwidth	520	500	572 MHz	720 MHz
Peak Emission Power	-41.3 dBm/MHz	41.3 dBm/MHz	-42.28 dBm/MHz	-41.92 dBm/MHz
Energy Per Pulse	25 nJ @100 kbps 16.8pJ @1Mbps*	57 pJ @100 kbps 29.2 pJ @1Mbps	0.36 nJ @100 kbps 34 pJ @1Mbps	0.36 nJ @100 kbps 34 pJ @1Mbps

*Excluding the power consumption of the buffer.

6.2 Design of the IR-UWB Transmitter in 130nm CMOS Process (Version 1)

The IR-UWB transmitter presented in this section has been published in [30] in 2017. The excerpt of the manuscript is presented here according to the publication guideline of IEEE for dissertation.

6.2.1 System Overview

In UWB communication system the transmitter needs to fully comply with the FCC spectral mask which limits the PSD to be lower than - 41.3 dBm/MHz. Assuming rectangular pulse envelope with 1 bit per symbol modulation the peak power of the PSD, S_{pk} can be expressed as,

$$S_{pk} = \frac{2R_b}{B} Ep \tag{6.2}$$

Where R_b is the data rate, B is the bandwidth and E_p is the pulse energy. The proposed transmitter, whose block diagram is depicted in Fig. 6.19 has an impulse generator that has 9 bits for achieving tunable pulse width. Since the pulse width, $T_{PW} = \frac{2}{B}$, by changing the pulse width the peak emission power is controlled. The next block is a tunable cross-coupled LC oscillator followed by a buffer. The transmitter follows on-off keying (OOK) modulation scheme. The core building block of the impulse generator is a tunable capacitor bank, an inverter, a NAND gate and finally another inverter to generate the desired impulse signal (Fig. 6.20). The pulse width of the generated impulse signal is controlled by turning on/off the capacitors in the capacitor bank (Fig. 6.21). The corresponding values of the capacitors in the bank are also shown in Fig. 6.21. The generated impulse signal (V_{p1}) is then delayed by 100 ps using an inverter delay chain. V_{p1} and V_{p2} are required for the fast startup of the LC oscillator circuit.

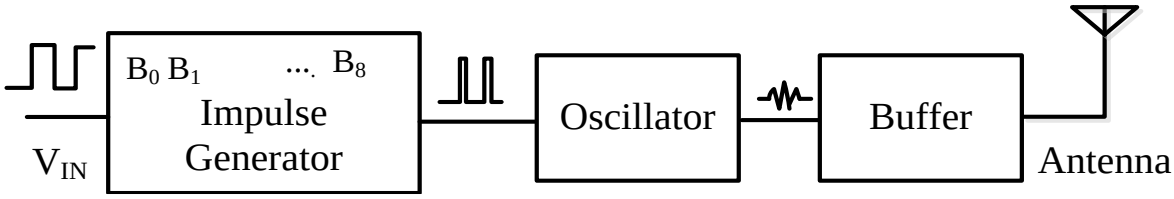

Figure 6.19: System level block diagram of the UWB transmitter.

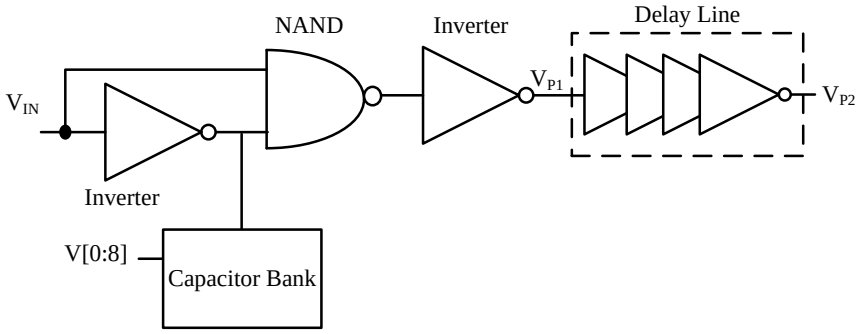

Figure 6.20: Schematic of the impulse generator structure.

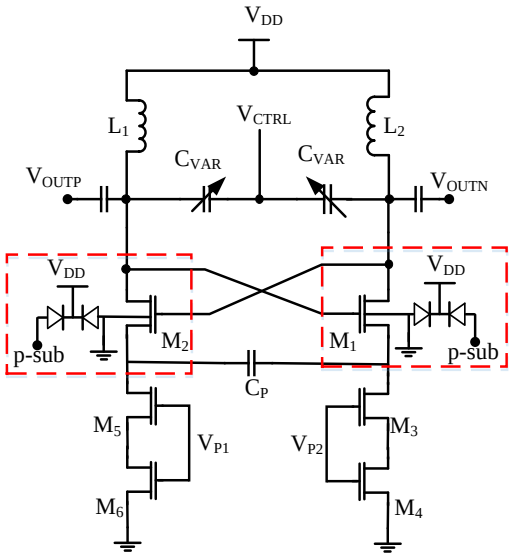

Figure 6.21: Tunable cross-coupled differential LC oscillator circuit.

The LC voltage controlled oscillator (VCO) core consists of the cross-coupled triple-well NMOS FETs (M_{1-2}) and LC tank with inductors (L_{1-2}) and variable capacitors (C_{var}) as shown in Fig. 6.22. The cross-sectional view of the triple-well NMOS transistor is illustrated in Fig. 6.23 which shows that the *p*-well is embedded within a deep *n*-well creating an isolated body for the NMOS from the *p*-substrate. The center frequency of oscillation can be tuned by changing the control voltage V_{CTRL}. The impulse signals, V_{p1} and V_{p2} that are generated by the impulse generator block controls the ON/OFF opeartion of the VCO through the tail transistor, M_{3-6}. The main aim of this design is to minimize the 'ON' time by enabling fast startup and turning off of the VCO. The tail current source of the LC oscillator has been modified to provide asymmetric drive to set up a large initial condition for oscillation, which results in a start-up time of smaller than 1 ns [62]. The asymmetry in current produces a large voltage difference across the C_p (=1.56 pF), which enables fast startup. A differential buffer is cascaded after the LC VCO to isolate the oscillator from the load impedance variation. A cascoded Class A topology is chosen for the buffer stage with proper sizing of the M_4 transistor as shown in Fig. 6.24 [63]. The input bias voltage (V_G) is chosen to be 1 V, which provides 0.8V to the gate of the triple NMOS transistors, M_{1-2} after the resistive divider. The high-pass filter at the input of the buffer provides good AC coupling to the LC oscillator at the oscillation frequency.

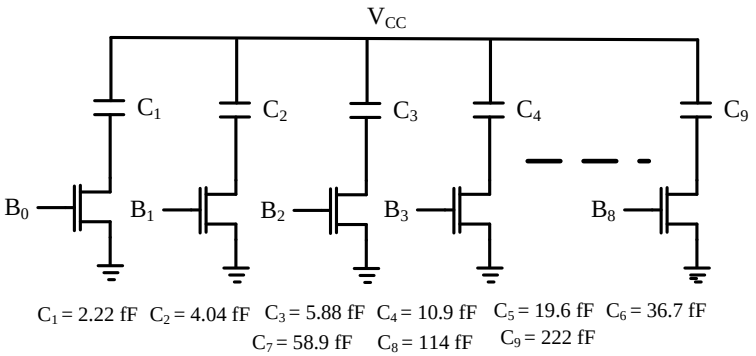

Figure 6.22: Circuit schematic of the 9-bit capacitor bank.

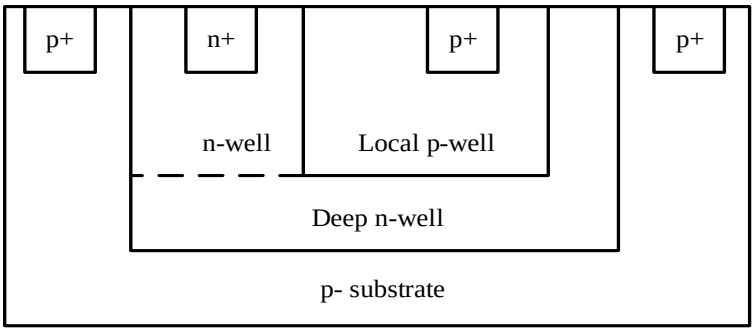

Figure 6.23: Cross section of the NMOS transistor in the triple-well 130 nm CMOS process.

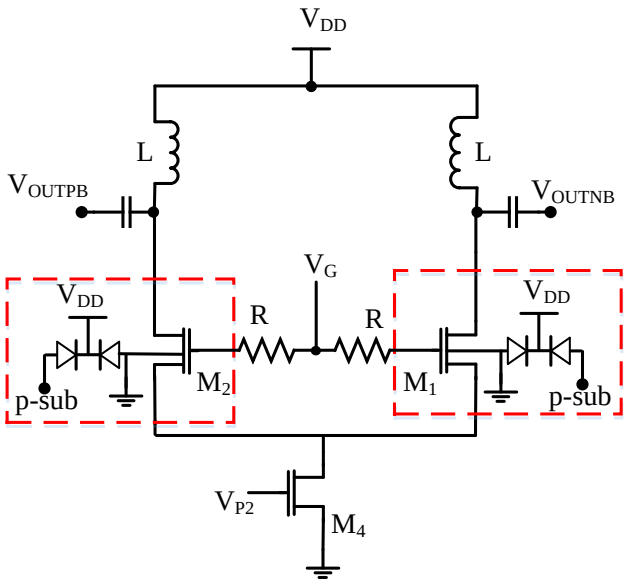

Figure 6.24: Schematic of the buffer.

6.2.2 Simulation Results

Fig. 6.25 shows the variation in pulse width for different active bits for the impulse generator. The total pulse width can be tuned from 280 ps to 770 ps which corresponds to a bandwidth tuning of ~1GHz. The up-converted impulse signal generated by LC oscillator is shown in Fig. 6.26. The amplitude of the signal is about 500 mV_{pp} and the pulse duration is about 3 ns. Fig. 6.27 shows the power spectral density of the signal at 4.5 GHz oscillation frequency. The approximate peak power is -42.3 dBm/MHz which follows the FCC regulation. The -10 dB signal bandwidth is about 800 MHz. The average power consumption of the total system is 0.836 µW with 1.2 V supply voltage, which results in overall power consumption of 8.23 pJ/pulse with 100 kbps data rate. At 1 Mbps data rate, the transmitter consumes 8.23 µW of power which results in 8.23 pJ/pulse energy efficiency. Fig. 6.28 shows the layout and the chip microphotograph of the proposed UWB transmitter highlighting the different design blocks in the transmitter. The total area of the transmitter is 600 µm by 600 µm in the 130 nm CMOS process.

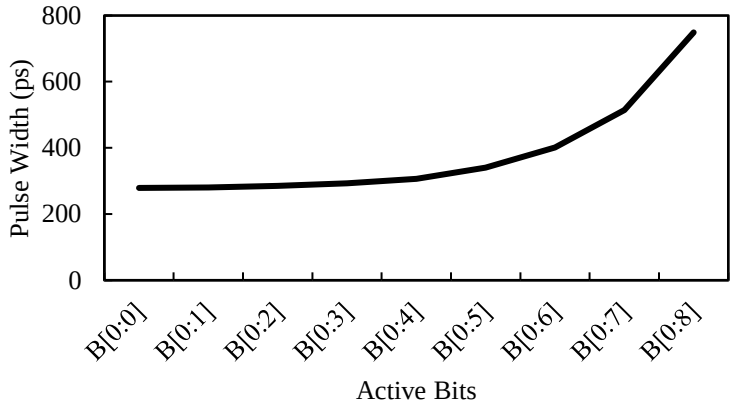

Figure 6.25: Pulse width of the impulse signal generated by the impulse generator for different bit combination.

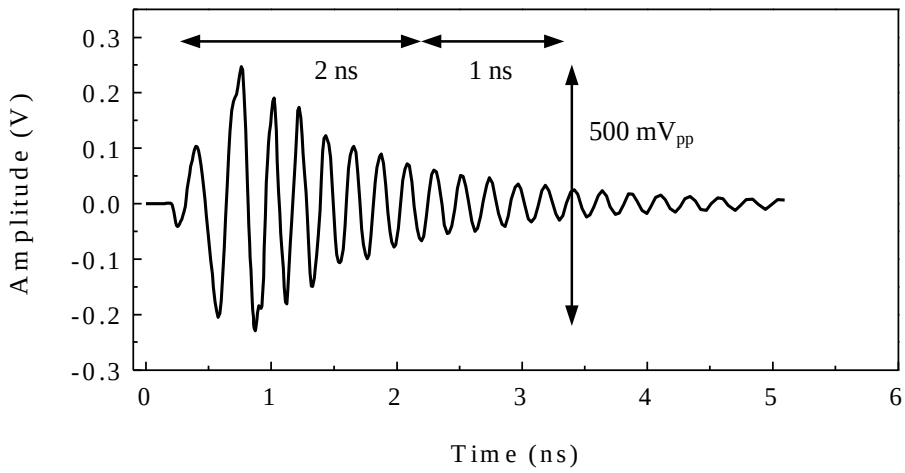

Figure 6.26: Post-layout simulation result of the impulse waveform from the LC oscillator (after buffer).

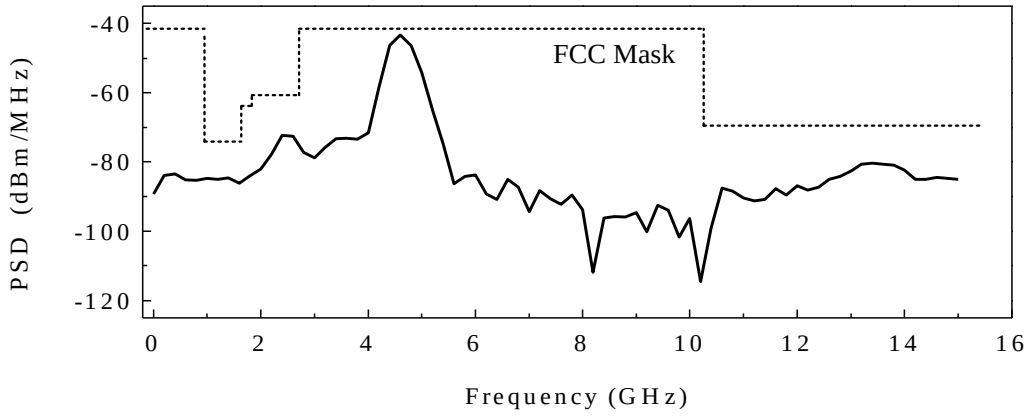

Figure 6.27: Power spectral density (PSD) of the impulse signal.

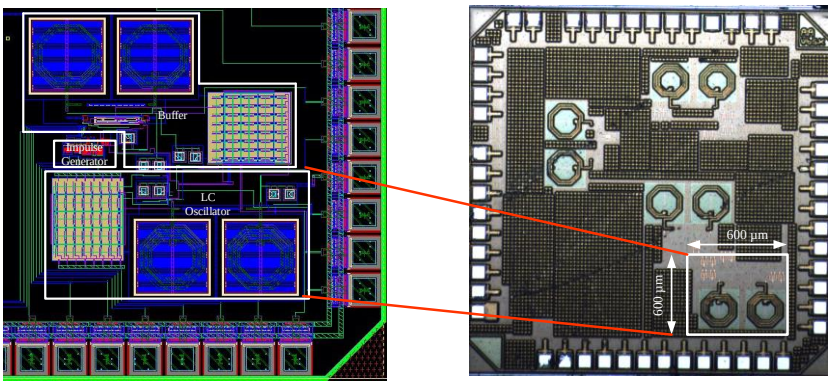

Chip Layout Chip Microphotograph

Figure 6.28: Chip Layout of the IR- UWB system in 130 nm CMOS process.

Table 6.3 compares the simulation results of the transmitter with the other state of the art IR-UWB designs published in the literature. The leakage power (off-state) of the proposed design is only 11.87 nW which is the lowest compared to the LC and ring oscillators based IR-UWB transmitters presented in [21] and [61]. The power consumption of the proposed design is 836 nW only, which is also the lowest compared to the other works. The energy per pulse for the proposed design at 100 kbps data rate is 8.37 pJ/pulse which is the lowest among the state-of-the-art designs.

A comparison of the power consumption of each block in the transmitter has been illustrated in Fig. 6.29. Compared to the 180 nm CMOS design, the power consumption for the 130 nm CMOS process design has been reduced almost 43 times. The impulse generator consumes 11% of the total power in the 130nm process, which is higher than the one designed in 180 nm process because of the added capacitor bank for bandwidth tuning. The overall power consumption of the buffer and the VCO has been reduced by reducing the supply voltage and the turn-on time of the transistor.

Table 6.3: Performance Comparison with Other State–of-the-Art works

Performance	[21]	[61]	This work (simulation)
Technology	180nm CMOS	90nm CMOS	130nm CMOS
Supply Voltage	1.5 V	1 V	1.2 V
Frequency Spectrum	3.1-5 GHz	3.1-5 GHz	3.1-5 GHz
Oscillator Architecture	LC	Ring	LC
Output Voltage Swing	0.16 V	0.5 V	0.5 V
Pulse Width	3.5 ns	1-2 ns	3 ns
Tx Leakage Power	3.9 mW	2.9 µW	11.87 nW
Tx Total Power	3.9 mW	5.7 µW	836 nW
Active Die Area (mm^2)	0.308 mm^2	0.1 mm^2	0.36 mm^2
Modulation	OOK	OOK	OOK
-10 dB Bandwidth	520	500	800
Peak Emission Power	-41.3 dBm/MHz	41.3 dBm/MHz	-42.3 dBm/MHz
Energy Per Pulse	25 nJ @100 kbps 16.8pJ @1Mbps*	57 pJ @100 kbps 29.2 pJ @1Mbps	8.37 pJ @100 kbps 8.23 pJ @100 kbps

*Excluding the power consumption of the buffer.

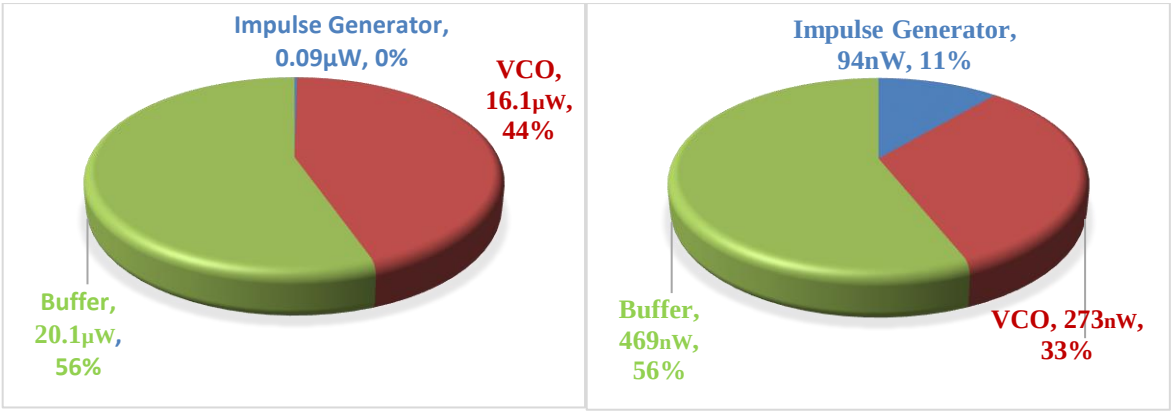

(a) (b)

Figure 6.29: Power dissipation pie chart of each block in the (a) 180 nm CMOS process and (b) 130 nm CMOS process.

6.3 Design of the IR-UWB Transmitter in 130nm CMOS Process (Version 2)

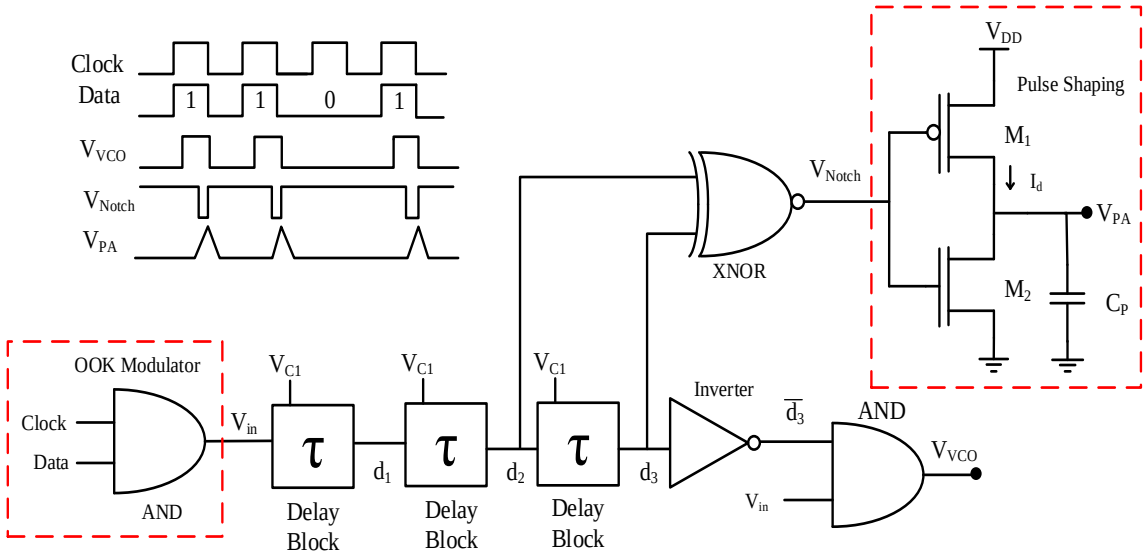

Figure 6.30: Impulse signal and triangular voltage generator.

6.3.1 System Overview

In this section, a second version of the IR-UWB transmitter designed using 130 nm process is presented. Fig. 6.30 shows the impulse signal generator and the triangular pulse shaping circuitry which is a modified design of the IR-UWB transmitter proposed by Carlos *et al*. [64]. The transmitter is implemented using on-off keying (OOK) modulation.

The transmitter block comprises of the complimentary cross-coupled LC VCO (Fig. 5.6) and the driver amplifier (Fig. 5.15) which have been presented in Chapter 5. The OOK modulation is achieved by using an AND gate. Since the LC VCO has a start-up time of 2.5 ns, the voltage, V_{VCO}, which drives the LC VCO, is turned on for a time period that is equal to the delay period of three delay blocks, 3τ. On the other hand, the output of the driver circuit is shaped by the triangular voltage V_{PA}, which has a pulse width equal to the delay period of one delay block, τ. The delay block consists of two cascaded current-starved inverters as shown in Fig. 6.4. The delay of each delay cell is modeled as [65]

$$t_{delay} = \frac{C_L}{I_d} V_o \tag{6.3}$$

where C_L is the load capacitance of each delay cell, I_d is the inverter current and V_0 is output voltage swing, which is 1.2 V for 130nm CMOS process. The current, I_d is controlled by the gate voltage V_{C1} of the transistors, M_1 and M_2 and that on the other hand changes the delay of each delay cells, as shown in equation 6.3. The pulse shaping circuit is basically a charge pump based circuitry. When the V_{Notch} voltage is low, M_1 transistor is turned on and M_2 transistor is turned off and thus the current I_d charges the capacitor C_p. The voltage across C_p is discharged through the transistor M_2 to the ground when V_{Notch} is high. The time domain output waveform of the V_{VCO} and V_{PA} voltage for V_{C1} = 300 mV are shown in Fig. 6.31. The pulse width of the V_{VCO} signal is about 12 ns while the pulse width of the V_{PA} is 3.5 ns. To ensure that the output of the VCO reaches the full swing, the pulse width is made longer for the V_{VCO} signal. Since the driver consumes much more power than the VCO, the pulse width of V_{PA} signal is kept smaller. The average power consumption of the impulse signal and triangle voltage generator is 61.87 nW with 1.2 V supply voltage. Since all of the blocks consists of digital logic gates, the power consumption is reduced.

6.3.2 Simulation Results

The individual simulation results of the VCO and the driver amplifier circuit are presented in Chapter 5. The time domain signal output of the transmitter (I_{tail} = 20 µA, V_{tune} = 400 mV, V_{bias} = 400 mV and V_{VCO} = 1.2 V) is shown in Fig. 6.32. The amplitude of the output signal is 600 mV_{pp} and the pulse width is ~ 3ns, where the ringing at the end is due to the inductance of the bond wire and the parasitic capacitance. The corresponding PSD is shown in Fig. 6.33. The center frequency is 5.34 GHz and the peak output power at the frequency is -42.56 dBm/MHz, which is lower than the -41.3 dBm/MHz FCC limit. The -10 dB bandwidth is ~1.03 GHz and the entire PSD follows the FCC mask regulation.

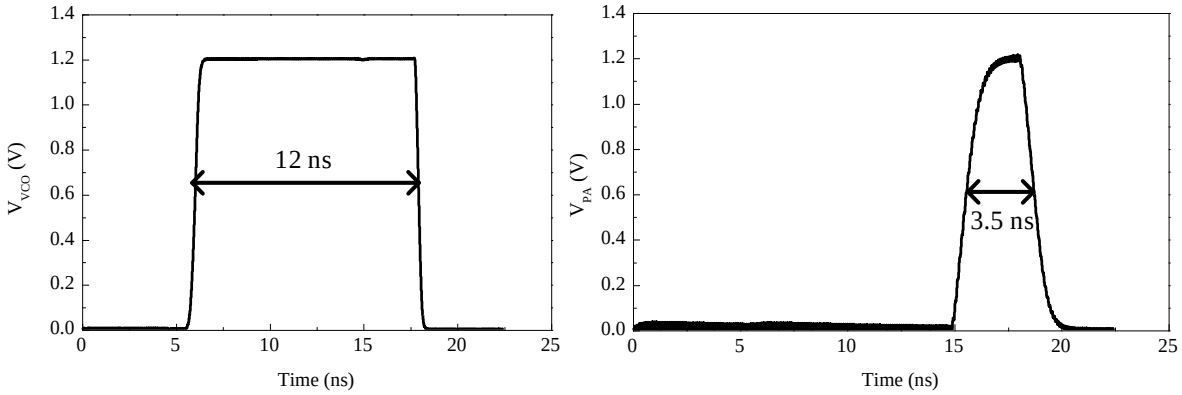

(a) (b)

Figure 6.31: (a) Time domain signal output of (a) V_{VCO} and (b) V_{PA} when V_{C1} = 300mV.

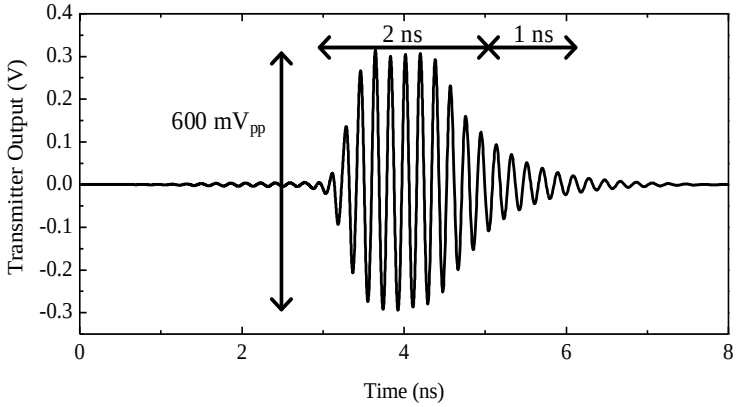

Figure 6.32: The simulated output waveform of the transmitter at V_{C1} = 300mV.

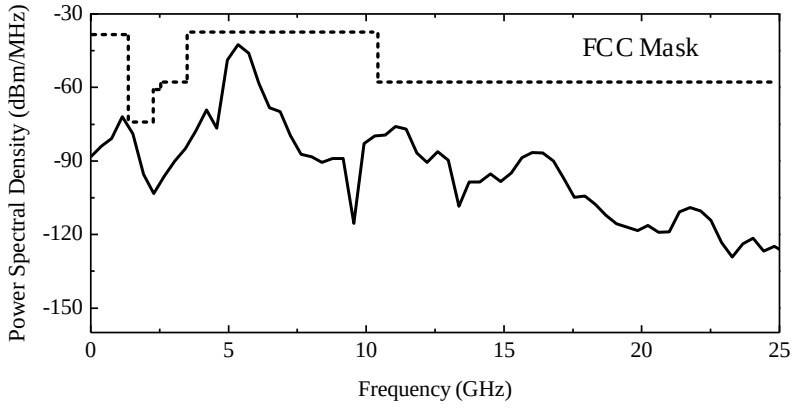

Figure 6.33: Power spectral density (PSD) of the transmitter output shown in Fig. 6.32.

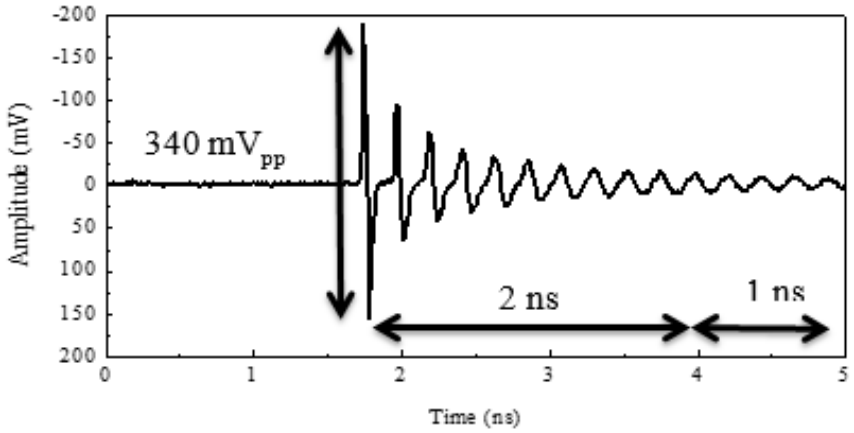

Figure 6.34: The measured output waveform of the IR-UWB transmitter.

6.3.3 Measurement Results

The measured time domain output waveform of the IR-UWB transmitter is shown in Fig. 6.34. From this waveform it can be seen that the amplitude of the signal is 340 mV_{pp} and the impulse duration is 2 ns with additional 1 ns of ringing. Due to the inductance of the bond-wire and the parasitic capacitance at the output node of the transmitter, a damping oscillation is observed at the output of the transmitter, In Fig. 6.35, the PSD of the transmitter output waveform is plotted for the V_{tune} = 400 mV. From the measured data, it can be seen that the impulse signal spectrum is centered at 3.56 GHz and the -10 dB bandwidth is ~550 MHz. The maximum emitted power is -46.3 dBm/MHz, which follows the FCC mask regulation. The tuning range was found to be limited between 3.5-3.7 GHz. By adequately designing varactor capacitor banks a wide tuning range can be achieved. Fig. 6.36 depicts the measured reflection coefficient at the output port of the transmitter. The measured *S11* of -15 dB indicates a good matching at the output port of the transmitter.

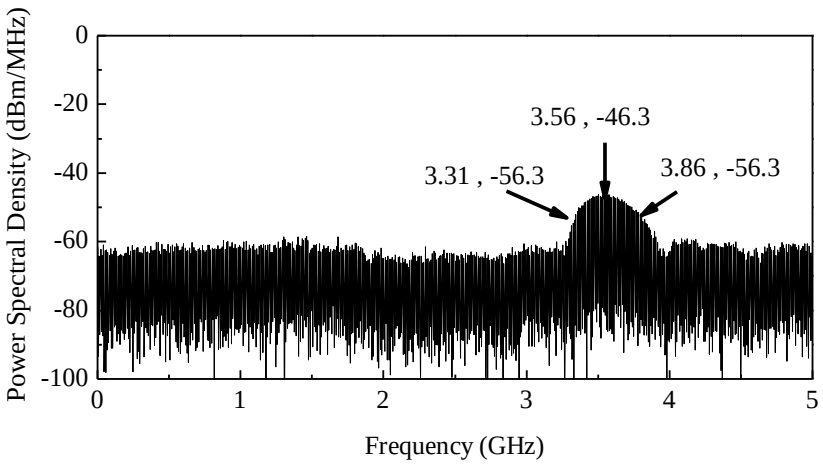

Figure 6.35: Power spectral density of the IR-UWB transmitter.

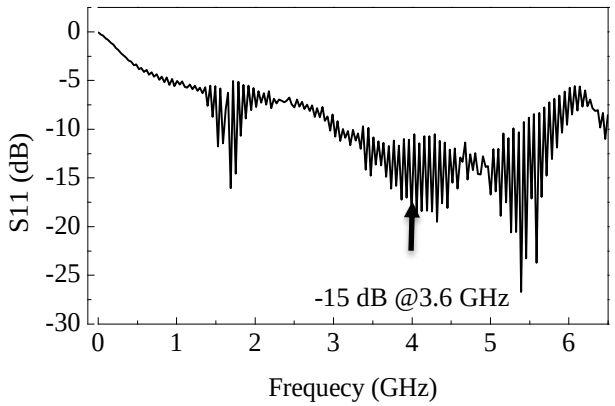

Figure 6.36: The reflection coefficient at the output port of the IR-UWB transmitter.

Fig. 6.37 shows the layout and the chip microphotograph of the IR-UWB transmitter in the 130 nm CMOS process, which occupies 0.115 mm^2 of the die area. Table 6.4 shows a comparison of the proposed work with the previously published literature. The leakage power of the transmitter is the lowest compared to all the other published works. While the ring oscillator based transmitter proposed by Dokania *et al.* [61] still has the lowest energy per pulse at 100 kbps data rate compared to all other works, this work manages to achieve a comparable power consumption at 100 kbps data rate and the lowest energy per pulse for higher data rates (>100 kbps). This is also evident from Fig. 6.38, where energy per pulse versus the data rate of the transmitters proposed by Dokania *et al.* [61], Phan *et al.* [21], Crepaldi *et al.* [66] and the transmitter proposed in this work. The power consumption of this work could be further reduced by reducing the time period of the V_{VCO} voltage so that the LC oscillator is on for even shorter period time thus dissipating less power. The tuning range is planned to be increased by including the varactor capacitor banks in the LC tank in future.

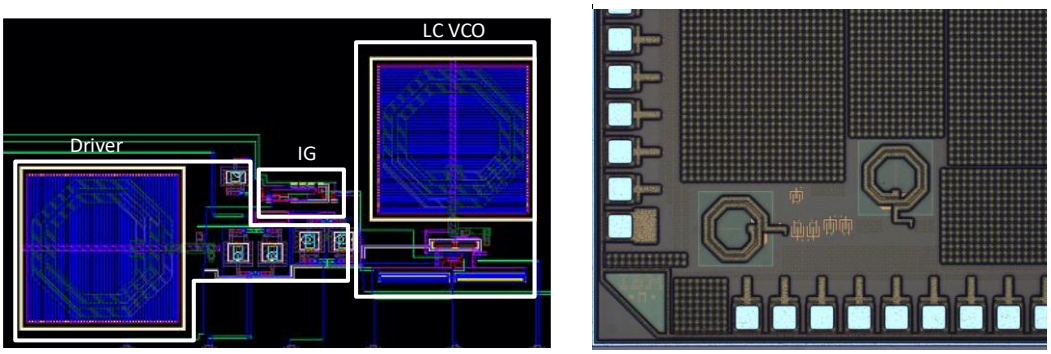

(a) (b)

Figure 6.37: (a) Layout and the (b) chip microphotograph of the IR-UWB transmitter in 130 nm CMOS process.

Table 6.4: Performance Comparison with the Other IR-UWB Transmitters

Performance	[21]	[61]	[66]	This work
Technology	180nm CMOS	90nm CMOS	90 nm CMOS	130nm CMOS
Supply Voltage	1.5 V	1 V	0.9 – 1.1 V	1.2 V
Frequency Spectrum	3.1-5 GHz	3.1-5 GHz	2.9 – 3.8 GHz	3.5-3.7 GHz
Oscillator Architecture	LC	Ring	LC	LC
Output Voltage Swing	0.16 V	0.5 V	610 mV_{pp}	340 mV_{pp}
Pulse Width	3.5 ns	1-2 ns	2 ns	3 ns
Tx Leakage Power	3.9 mW	2.9 µW	184 µW	2.88 µW
Tx Total Power (@100 kbps)	3.9 mW	5.7 µW	258 µW (@1Mbps)	9.12 µW
Active Die Area (mm^2)	0.308 mm^2	0.1 mm^2	0.6 mm^2	0.115 mm^2
Modulation	OOK	OOK	OOK, S-OOK	OOK
-10 dB Bandwidth	520	500	500 MHz	550 MHz
Peak Emission Power	-41.3 dBm/MHz	-41.3 dBm/MHz	-51.95 dBm/MHz (@1Mbps)	-46.53 dBm/MHz
Energy Per Pulse	25 nJ @100 kbps* 16.8pJ @1Mbps*	57 pJ @100 kbps 29.2 pJ @1Mbps	1.91 nJ @100 kbps# 249 pJ @1Mbps	91.2 pJ @100 kbps 12.96 pJ @1Mbps

*Excluding the power consumption of the buffer
calculated from equation provided in the manuscript

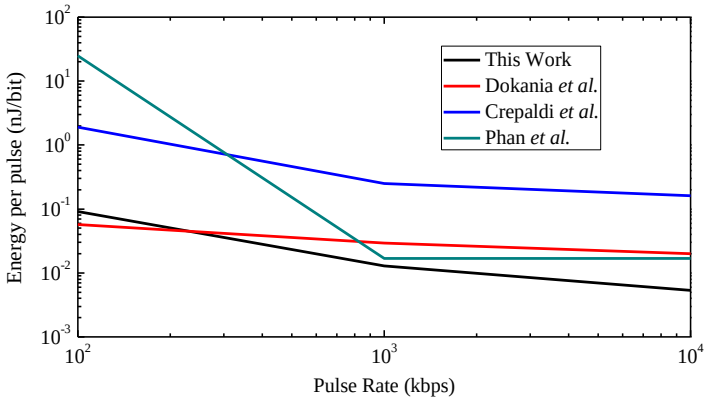

Figure 6.38: Energy per pulse versus data rate of different published works ([61], [66], [21]) and this work.

The average transmitted power is calculated to be -19.13 dBm and the duty cycling ratio for 100 kbps data rate is 0.03%. The calculated path loss is ~43.5 dBm which leads to the minimum sensitivity that the receiver needs to have to attain a BER of 10^{-4}.

6.4 Summary and Conclusion

In this chapter, three low-power IR-UWB transmitter designs have been presented. By implementing aggressive duty-cycling and reducing the supply voltage, a competitive energy efficiency is achieved.

Chapter 7 Conclusion and Future Work

7.1 Original Contributions

In this work a PVDF-based respiration monitoring sensor has been proposed which is light-weight and can be easily integrated with a nasal cannula or mask. A low-power, low-noise charge amplifier is proposed for efficient charge-to-voltage conversion of the charges generated by the PVDF transducer. A low-power low-complexity OOK based IR-UWB transmitter is proposed for low data-rate biomedical applications such as the respiration sensor. The original contributions of this work are listed below:

- In this work, a novel approach of respiration monitoring based on a PVDF-based pyroelectric transducer is presented. It not only eliminates the complexity and inconvenience related to the previously discussed methods but also has the superiority over other sensor-based system studied recently. The transducer is placed underneath the nostril or inside a mask or cannula to detect the temperature change during breathing.
- A low-power low-noise fully integrated charge amplifier is designed in 0.5µm CMOS process as the front-end amplifier of the respiration monitoring sensor. The proposed charge amplifier features low power consumption of 5.4 µW and very low input referred noise of 5.017 μV_{rms} along with the lower cut-off frequency of 125 mHz. These features make the charge amplifier a potential candidate for use as front-end circuitry of a respiration monitoring system using pyroelectric transducer.
- To reduce the power consumption even further, another charge amplifier is also designed using 130 nm CMOS process. With a power consumption of only 1.8 µW, the amplifier has a -3 dB bandwidth of 10 mHz to 13 kHz and a NEF of 2.79.

- A low-power IR-UWB transmitter is designed using standard 180 nm CMOS process. Even though the measurement results of the transmitter in the 180 nm CMOS process show a shift in the oscillation frequency, the active and the leakage power consumption of the transmitter are 36.29 µW and 437.4 nW, respectively making this design competitive compared to other state-of-the-art IR-UWB transmitters. To achieve even better energy efficiency, two versions of IR-UWB transmitters are designed using 130 nm CMOS process which have been able to achieve an energy efficiency of 8.23 pJ/pulse and 91.2 pJ/pulse, respectively, which are very much comparable to other state-of-the-art works.

7.2 Future Works

Some improvements of the proposed respiration monitoring sensor, the front-end amplifier, and the IR-UWB transmitter remain to be done and are listed below as future work:

- A variable gain front-end amplifier could be designed so that the gain can be adjusted for different nasal cannula and patch based pyroelectric transducer. The bandwidth can also be adjusted as needed so that the integrated noise over the bandwidth can be lowered by reducing the bandwidth, Tseng *et al.* proposed a variable gain and bandwidth amplifier by implementing a capacitor bank for the input capacitance and by implementing different NMOS transistors as load capacitors [67]. Chopper amplifier such as proposed by Yazicioglu *et al.* could also be studied to incorporate the chopping technique in the existing folded-cascode OTA to reduce the noise contribution due to flicker noise even further [68].
- Some packets of data are found to be corrupted and dropped during the transmission/reception of data using DecaWave DWM1000 module. The received signal can be resampled at 50 Hz (20 ms period) rate to retrieve the lost data.

- To achieve a wider tuning range of the VCO, a varactor based capacitor bank could be implemented along with switches [69].
- An energy detection based receiver circuit board is needed to be designed using commercially available off-the-shelf components to test the performance and bit error rate (BER) of the transmitter. An antenna can be designed either on-chip [70] or a chip antenna such as the UWB chip antenna by Johanson Technology (P/N 3100AT51A7200) can be used for the transmitter and receiver boards.

References

[1] C. A. Kushida, M. R. Littner, T. Morgenthaler, C. A. Alessi, D. Bailey, J. Coleman Jr, *et al.*, "Practice parameters for the indications for polysomnography and related procedures: an update for 2005," *Sleep*, vol. 28, pp. 499-521, 2005.

[2] J. Werthammer, J. Krasner, J. DiBenedetto, and A. R. Stark, "Apnea monitoring by acoustic detection of airflow," *Pediatrics*, vol. 71, pp. 53-55, 1983.

[3] P. Corbishley and E. Rodríguez-Villegas, "Breathing detection: towards a miniaturized, wearable, battery-operated monitoring system," *IEEE Transactions on Biomedical Engineering*, vol. 55, pp. 196-204, 2008.

[4] D. Falie and M. Ichim, "Sleep monitoring and sleep apnea event detection using a 3D camera," in *Communications (COMM), 2010 8th International Conference on*, 2010, pp. 177-180.

[5] K. J. Kim, Y. M. Chang, S. Yoon, and H. J. Kim, "A novel piezoelectric PVDF film-based physiological sensing belt for a complementary respiration and heartbeat monitoring system," *Integrated Ferroelectrics*, vol. 107, pp. 53-68, 2009.

[6] F. Erden and A. Enis, "Respiratory rate monitoring using infrared sensors," in *2015 9th International Conference on Electrical and Electronics Engineering (ELECO)*, 2015, pp. 1136-1140.

[7] G. P. Heldt and R. J. Ward III, "Evaluation of Ultrasound-Based Sensor to Monitor Respiratory and Nonrespiratory Movement and Timing in Infants," *IEEE Transactions on Biomedical Engineering*, vol. 63, pp. 619-629, 2016.

[8] S. Y. Chekmenev, H. Rara, and A. A. Farag, "Non-contact, wavelet-based measurement of vital signs using thermal imaging," in *The first international conference on graphics, vision, and image processing (GVIP), Cairo, Egypt*, 2005, pp. 107-112.

[9] D. Zito, D. Pepe, M. Mincica, F. Zito, A. Tognetti, A. Lanatà, *et al.*, "SoC CMOS UWB pulse radar sensor for contactless respiratory rate monitoring," *IEEE Transactions on Biomedical Circuits and Systems*, vol. 5, pp. 503-510, 2011.

[10] S.-H. Liao, W.-J. Chen, and M. S.-C. Lu, "A CMOS MEMS capacitive flow sensor for respiratory monitoring," *IEEE Sensors Journal*, vol. 13, pp. 1401-1402, 2013.

[11] H.-C. Liu, W.-C. Huang, Y.-J. Chen, C.-C. Lu, and J.-T. Huang, "An electromechanical system based on carbon nanotube sensors to detect apnea," *IEEE Sensors Journal*, vol. 13, pp. 2737-2741, 2013.

[12] M. Folke, F. Granstedt, B. Hök, and H. Scheer, "Comparative provocation test of respiratory monitoring methods," *Journal of clinical monitoring and computing*, vol. 17, pp. 97-103, 2002.

[13] I. Mahbub, S. A. Pullano, H. Wang, S. K. Islam, A. S. Fiorillo, G. To, *et al.*, "A Low-Power Wireless Piezoelectric Sensor-Based Respiration Monitoring System Realized in CMOS Process," *IEEE Sensors Journal*, vol. 17, pp. 1858-1864, 2017.

[14] I. Mahbub, H. Wang, S. K. Islam, S. A. Pullano, and A. S. Fiorillo, "A low power wireless breathing monitoring system using piezoelectric transducer," in *Medical Measurements and Applications (MeMeA), 2016 IEEE International Symposium on*, 2016, pp. 1-5.

[15] S. H. Hwang, H. J. Lee, H. N. Yoon, Y.-J. G. Lee, Y. J. Lee, D.-U. Jeong, *et al.*, "Unconstrained sleep apnea monitoring using polyvinylidene fluoride film-based sensor," *IEEE Transactions on Biomedical Engineering*, vol. 61, pp. 2125-2134, 2014.

[16] T. Denison, K. Consoer, W. Santa, A. T. Avestruz, J. Cooley, and A. Kelly, "A 2 µW 100 nV/rtHz Chopper-Stabilized Instrumentation Amplifier for Chronic Measurement of

Neural Field Potentials," *IEEE Journal of Solid-State Circuits,* vol. 42, pp. 2934-2945, 2007.
[17] R. R. Harrison and C. Charles, "A low-power low-noise CMOS amplifier for neural recording applications," *IEEE Journal of solid-state circuits,* vol. 38, pp. 958-965, 2003.
[18] P. Kmon and P. Gryboś, "Energy efficient low-noise multichannel neural amplifier in submicron CMOS process," *IEEE Transactions on Circuits and Systems I: Regular Papers,* vol. 60, pp. 1764-1775, 2013.
[19] B. W. Cook, A. Berny, A. Molnar, S. Lanzisera, and K. S. J. Pister, "Low-Power 2.4-GHz Transceiver With Passive RX Front-End and 400-mV Supply," *IEEE Journal of Solid-State Circuits,* vol. 41, pp. 2757-2766, 2006.
[20] P. P. Mercier, D. C. Daly, and A. P. Chandrakasan, "An energy-efficient all-digital UWB transmitter employing dual capacitively-coupled pulse-shaping drivers," *IEEE Journal of Solid-State Circuits,* vol. 44, pp. 1679-1688, 2009.
[21] A. T. Phan, J. Lee, V. Krizhanovskii, Q. Le, S. K. Han, and S. G. Lee, "Energy-Efficient Low-Complexity CMOS Pulse Generator for Multiband UWB Impulse Radio," *IEEE Transactions on Circuits and Systems I: Regular Papers,* vol. 55, pp. 3552-3563, 2008.
[22] S. A. Pullano, A. S. Fiorillo, I. Mahbub, S. K. Islam, M. S. Gaylord, and V. Lorch, "Non-invasive integrated wireless breathing monitoring system based on a pyroelectric transducer," in *2016 IEEE SENSORS*, 2016, pp. 1-3.
[23] P. Höppe, "Temperatures of expired air under varying climatic conditions," *International journal of biometeorology,* vol. 25, pp. 127-132, 1981.
[24] R. Newsome and E. Andrei, "Measurement of the pyroelectric coefficient of poly (vinylidene fluoride) down to 3 K," *Physical Review B,* vol. 55, p. 7264, 1997.
[25] S. A. Pullano, I. Mahbub, S. K. Islam, and A. S. Fiorillo, "PVDF Sensor Stimulated by Infrared Radiation for Temperature Monitoring in Microfluidic Devices," *Sensors,* vol. 17, p. 850, 2017.
[26] R. Assaad and J. Silva-Martinez, "Enhancing general performance of folded cascode amplifier by recycling current," *Electronics Letters,* vol. 43, pp. 1243-1244, 2007.
[27] S. Pullano, I. Mahbub, S. Islam, and A. Fiorillo, "PVDF Sensor Stimulated by Infrared Radiation for Temperature Monitoring in Microfluidic Devices," *Sensors,* vol. 17, p. 850, 2017.
[28] Y. Tsividis and C. McAndrew, *Operation and Modeling of the MOS Transistor*: Oxford Univ. Press, 2011.
[29] D. M. Binkley, "Tradeoffs and optimization in analog CMOS design," in *2007 14th International Conference on Mixed Design of Integrated Circuits and Systems*, 2007, pp. 47-60.
[30] I. Mahbub and S. K. Islam, "A low-power impulse radio ultra-wideband (IRUWB) transmitter for biomedical sensor applications," in *2017 United States National Committee of URSI National Radio Science Meeting (USNC-URSI NRSM)*, 2017, pp. 1-2.
[31] I. Mahbub, M. S. Hasan, S. A. Pullano, F. Quaiyum, C. P. Stephens, S. K. Islam, *et al.*, "A low power wireless apnea detection system based on pyroelectric sensor," in *Biomedical Wireless Technologies, Networks, and Sensing Systems (BioWireleSS), 2015 IEEE Topical Conference on*, 2015, pp. 1-3.
[32] J. Jin and E. Sánchez-Sinencio, "A home sleep apnea screening device with time-domain signal processing and autonomous scoring capability," *IEEE transactions on biomedical circuits and systems,* vol. 9, pp. 96-104, 2015.

[33] A. Srivastava, R. Bai, D. Blaauw, and D. Sylvester, "Modeling and analysis of leakage power considering within-die process variations," in *Proceedings of the 2002 international symposium on Low power electronics and design*, 2002, pp. 64-67.

[34] J. Ou and P. M. Ferreira, "A g_m/I_D-Based Noise Optimization for CMOS Folded-Cascode Operational Amplifier," *IEEE Transactions on Circuits and Systems II: Express Briefs*, vol. 61, pp. 783-787, 2014.

[35] J. Holleman and B. Otis, "A sub-microwatt low-noise amplifier for neural recording," in *Engineering in Medicine and Biology Society, 2007. EMBS 2007. 29th Annual International Conference of the IEEE*, 2007, pp. 3930-3933.

[36] T. A. Phan, J. Lee, V. Krizhanovskii, S. K. Han, and S. G. Lee, "A 18-pJ/Pulse OOK CMOS Transmitter for Multiband UWB Impulse Radio," *IEEE Microwave and Wireless Components Letters*, vol. 17, pp. 688-690, 2007.

[37] D. D. Wentzloff and A. P. Chandrakasan, "Gaussian pulse Generators for subbanded ultra-wideband transmitters," *IEEE Transactions on Microwave Theory and Techniques*, vol. 54, pp. 1647-1655, 2006.

[38] "Revision of Part 15 the Commission's rules regarding ultra-wideband transmission systems," *FCC*, vol. ET Docket, pp. 98–153 2002.

[39] M. A. Stelios, A. D. Nick, M. T. Effie, K. M. Dimitris, and S. C. Thomopoulos, "An indoor localization platform for ambient assisted living using UWB," in *Proceedings of the 6th international conference on advances in mobile computing and multimedia*, 2008, pp. 178-182.

[40] K. Higashikaturagi, Y. Nakahata, I. Matsunami, and A. Kajiwara, "Non-invasive respiration monitoring sensor using UWB-IR," in *2008 IEEE International Conference on Ultra-Wideband*, 2008, pp. 101-104.

[41] M. S. Chae, Z. Yang, M. R. Yuce, L. Hoang, and W. Liu, "A 128-Channel 6 mW Wireless Neural Recording IC With Spike Feature Extraction and UWB Transmitter," *IEEE Transactions on Neural Systems and Rehabilitation Engineering*, vol. 17, pp. 312-321, 2009.

[42] J. Youngkyun, J. Sungyong, and L. Jin, "A CMOS impulse generator for UWB wireless communication systems," in *Circuits and Systems, 2004. ISCAS '04. Proceedings of the 2004 International Symposium on*, 2004, pp. IV-129-32 Vol.4.

[43] H. Kim, D. Park, and Y. Joo, "All-digital low-power CMOS pulse generator for UWB system," *Electronics Letters*, vol. 40, p. 1, 2004.

[44] A. Apsel, X. Wang, and R. Dokania, "Low Power Impulse Radio Transceivers," in *Design of Ultra-Low Power Impulse Radios*, ed: Springer, 2014, pp. 37-69.

[45] S. Hongsan, P. Orlik, A. M. Haimovich, L. J. Cimini, and Z. Jinyun, "On the spectral and power requirements for ultra-wideband transmission," in *Communications, 2003. ICC '03. IEEE International Conference on*, 2003, pp. 738-742 vol.1.

[46] M. Demirkan and R. R. Spencer, "A Pulse-Based Ultra-Wideband Transmitter in 90-nm CMOS for WPANs," *IEEE Journal of Solid-State Circuits*, vol. 43, pp. 2820-2828, 2008.

[47] F. Padovan, A. Bevilacqua, and A. Neviani, "A 20Mb/s, 2.76 pJ/b UWB impulse radio TX with 11.7% efficiency in 130 nm CMOS," in *European Solid State Circuits Conference (ESSCIRC), ESSCIRC 2014 - 40th*, 2014, pp. 287-290.

[48] "DecaWave, DW 1000 User manual [Online]. Available: thetoolchain.com/mirror/dw1000/dw1000_user_manual_v2.05.pdf," 2015.

[49] "DecaWave, DWM 1000 datasheet. [Online]. Available: www.decawave.com/sites/default/files/resources/dwm1000-datasheet-v1.3.pdf," 2015.
[50] "Atmel, ATSAM3S2BA-MU datasheet [Online]. Available: https://www.google.com/url?sa=t&rct=j&q=&esrc=s&source=web&cd=3&cad=rja&uact=8&ved=0ahUKEwjDoOO1rJ3UAhXGRiYKHYrfAQQQFggsMAI&url=http%3A%2F%2Fwww.atmel.com%2FImages%2FATMEL_6500S-32-bit%2520Cortex-M3%2520Microcontroller_SAM3S_Summary-Datasheet.pdf&usg=AFQjCNFRZXRQ0thEBibDmsLXwKAH5wLpcQ&sig2=B6G27xL69QvaysmZ3hN96A."
[51] M. Malajner, P. Planinšič, and D. Gleich, "UWB ranging accuracy," in *2015 International Conference on Systems, Signals and Image Processing (IWSSIP)*, 2015, pp. 61-64.
[52] A. Figueroa, B. Al-Qudsi, N. Joram, and F. Ellinger, "Comparison of two-way ranging with FMCW and UWB radar systems," in *2016 13th Workshop on Positioning, Navigation and Communications (WPNC)*, 2016, pp. 1-6.
[53] D. Ham and A. Hajimiri, "Concepts and methods in optimization of integrated LC VCOs," *IEEE journal of solid-state circuits*, vol. 36, pp. 896-909, 2001.
[54] I. Mahbub, S. K. Islam, and A. Fathy, "Impulse radio ultra-wideband (IR-UWB) transmitter for low power low data rate biomedical sensor applications," in *2016 IEEE Topical Conference on Biomedical Wireless Technologies, Networks, and Sensing Systems (BioWireleSS)*, 2016, pp. 88-90.
[55] A. Hajimiri and T. H. Lee, "A general theory of phase noise in electrical oscillators," *IEEE journal of solid-state circuits*, vol. 33, pp. 179-194, 1998.
[56] D. Lesson, "A simple model of feedback oscillator noise spectrum," *proc. IEEE*, vol. 54, pp. 329-330, 1966.
[57] B. Razavi and R. Behzad, *RF microelectronics* vol. 2: Prentice Hall New Jersey, 1998.
[58] P. Andreani, "A 2GHz, 17% tuning range quadrature CMOS VCO with high figure-of-merit and 0.6^0 phase error," in *Proceedings of the 28th European Solid-State Circuits Conference*, 2002, pp. 815-818.
[59] Y. Zheng, M. A. Arasu, K. W. Wong, Y. J. The, A. P. H. Suan, D. D. Tran, *et al.*, "A 0.18µm CMOS 802.15.4a UWB Transceiver for Communication and Localization," in *2008 IEEE International Solid-State Circuits Conference - Digest of Technical Papers*, 2008, pp. 118-600.
[60] M. Crepaldi, D. Dapra, A. Bonanno, I. Aulika, D. Demarchi, and P. Civera, "A Very Low-Complexity 0.3-4.4 GHz 0.004 mm^2 All-Digital Ultra-Wide-Band Pulsed Transmitter for Energy Detection Receivers," *IEEE Transactions on Circuits and Systems I: Regular Papers*, vol. 59, pp. 2443-2455, 2012.
[61] R. K. Dokania, X. Y. Wang, C. I. Dorta-Quinones, W. Godycki, S. G. Tallur, and A. B. Apsel, "A 6µw, 100kbps, 3-5GHz, UWB impulse radio transmitter," in *Proceedings of the 16th ACM/IEEE international symposium on Low power electronics and design*, 2010, pp. 91-94.
[62] D. Barras, F. Ellinger, H. Jackel, and W. Hirt, "Low-power ultra-wideband wavelets generator with fast start-up circuit," *IEEE Transactions on Microwave Theory and Techniques*, vol. 54, pp. 2138-2145, 2006.
[63] J. Charthad, M. J. Weber, T. C. Chang, and A. Arbabian, "A mm-sized implantable medical device (IMD) with ultrasonic power transfer and a hybrid bi-directional data link," *IEEE Journal of Solid-State Circuits*, vol. 50, pp. 1741-1753, 2015.

[64] C. I. Dorta-Quiñones, X. Y. Wang, R. K. Dokania, A. Gailey, M. Lindau, and A. B. Apsel, "A Wireless FSCV Monitoring IC With Analog Background Subtraction and UWB Telemetry," *IEEE Transactions on Biomedical Circuits and Systems,* vol. 10, pp. 289-299, 2016.

[65] G. S. Jovanović and M. Stojčev, "Linear current starved delay element," *Proc. of ICEST,* 2005.

[66] M. Crepaldi, C. Li, J. R. Fernandes, and P. R. Kinget, "An Ultra-Wideband Impulse-Radio Transceiver Chipset Using Synchronized-OOK Modulation," *IEEE Journal of Solid-State Circuits,* vol. 46, pp. 2284-2299, 2011.

[67] Y. Tseng, Y. Ho, S. Kao, and C. Su, "A 0.09 μ W Low Power Front-End Biopotential Amplifier for Biosignal Recording," *IEEE Transactions on Biomedical Circuits and Systems,* vol. 6, pp. 508-516, 2012.

[68] R. F. Yazicioglu, P. Merken, R. Puers, and C. V. Hoof, "A 60 μ W 60 nV/√Hz Readout Front-End for Portable Biopotential Acquisition Systems," *IEEE Journal of Solid-State Circuits,* vol. 42, pp. 1100-1110, 2007.

[69] S. Geng, D. Liu, Y. Li, H. Zhuo, W. Rhee, and Z. Wang, "A 13.3 mW 500 Mb/s IR-UWB Transceiver With Link Margin Enhancement Technique for Meter-Range Communications," *IEEE Journal of Solid-State Circuits,* vol. 50, pp. 669-678, 2015.

[70] V. V. Kulkarni, M. Muqsith, K. Niitsu, H. Ishikuro, and T. Kuroda, "A 750 Mb/s, 12 pJ/b, 6-to-10 GHz CMOS IR-UWB Transmitter With Embedded On-Chip Antenna," *IEEE Journal of Solid-State Circuits,* vol. 44, pp. 394-403, 2009.

Vita

Ifana Mahbub has received her B.Sc. degree in Electrical and Electronic Engineering from Bangladesh University of Engineering and Technology (BUET), Dhaka, in 2012. She is a Chancellor's Fellow and Graduate Research Assistant in the Department of Electrical Engineering and Computer Science at the University of Tennessee, Knoxville. She is working towards her Ph.D. degree under the supervision of Dr. Syed Kamrul Islam. Her dissertation topic includes the design and implementation of low-power front-end amplifier and impulse-radio ultra-wideband (IR-UWB) transmitter for a wearable wireless respiration monitoring system. In recognition of her outstanding research achievements, she has received the Chancellor's Citation award for the "Extraordinary Professional Promise" in 2014, 2015 and 2016 academic years. She also worked as an RF design engineering intern at the Boston Design Center of Qorvo, Inc. during the summer semesters in 2015 and 2016 respectively. As an intern, she worked towards the development of techniques to characterize memory effects in average power tracking (APT) and envelope tracking (ET) power amplifier using single carrier and carrier aggregated LTE waveforms. Her research interests include low-power CMOS analog and RF integrated circuit design for implantable and wearable biomedical sensing applications.